Towards high efficiency thin film solar cells

Guifang Han,[a,b] Sam Zhang,[a,*] Pablo P. Boix,[b] Lydia Helena Wong,[b,c] Lidong Sun,[d] Shui-Yang Lien [e]

[a] School of Mechanical and Aerospace Engineering, Nanyang Technological University, 50 Nanyang Avenue, 639798 Singapore

[b] Energy Research Institute @NTU (ERI@N), Research Techno Plaza, X-Frontier Block, Level 5, 50 Nanyang Drive, 637553 Singapore

[c] School of Materials Science and Engineering, Nanyang Technological University, Block N4.1, Nanyang Avenue, 639798 Singapore, Singapore

[d] School of Materials Science and Engineering, Chong Qing University, Chongqing, 400044 China

[e] Department of Materials Science and Engineering, Dayeh University, Changhua, 515 Taiwan

[*] Corresponding author, email: MSYZhang@ntu.edu.sg

Abstract

As an alternative to single crystal silicon photovoltaics, thin film solar cells have been extensively explored for miniaturized cost-effective photovoltaic systems. Though the fight to gain efficiency has been severely engaged over the years, the battle is not yet over. In this review, we comb the fields to elucidate the strategies towards high efficiency thin films solar cells and provide pointers for further development. Starting from the photoelectron generation, we look into the fundamental issues in photoelectric conversion processes, including light harvesting and charge handling (separations, transportations and collections). The emerging organic-inorganic halide perovskite systems, as well as the rapidly developed polycrystalline inorganic systems, organic photovoltaics and amorphous silicon cells are discussed in detail. The biggest bottleneck for the cost-effective polycrystalline inorganic cells is the composition sensitivity and deep defects; for amorphous silicon cells, it is the quantum of the dangling bonds; for organic cells, it is the low charge carrier mobility and high exciton binding energy; and for perovskite cells, it is the environmental degradation and the controversial mechanisms of generation of I-V hysteresis. Strategies of light harvesting and charge handling as well as directions to break the bottlenecks are pointed out.

Keywords: Thin film solar cell, light harvesting, charge dissociation, charge transport and collection, perovskite, stability

Note: Dr. Pablo P. Boix's current affiliation: Instituto de Ciencia Molecular, Universidad de Valencia, c. Catedratico J. Beltran2, 46980 Paterna, Valencia, Spain

Table of Contents

Thin film solar cells have encountered bottlenecks for efficiency hike. We review the design rules and strategies for high efficient thin film solar cells to provide better design guidance for veterans and also an easy to follow introduction to newcomers in this field.

To provide the basis for discussion on efficiency enhancement, currently widely studied four categories of thin film solar cells are discussed with regard to how they work: polycrystalline inorganic [$Cu(In,Ga)(S,Se)_2$ (or CIGSSe for short), $Cu_2ZnSn(S,Se)_4$ (or CZTSSe)], amorphous silicon (a-Si), organic photovoltaics (OPV) and organic-inorganic halide perovskite (perovskite) and etc.

Based on the working principles, strategies in achieving high efficiency is discussed in a few aspects in serial, i.e., Light harvesting, Charge dissociation, Charge transportation and collection.

This section starts briefly with what happens when a ray of light hit a semiconductor, how photoelectron is generated and transported outside to produce electricity. Making use of the available light to the fullest extent is light harvesting. Other related topics discussed in this section are Bandgap adjustment and Light utilization. Also mentioned in this section is how to make the solar cell Efficient yet transparent (as this is a matter of selective transmission of light in the visible range).

Creation of an effective “photoelectron” involves separation the electrons and holes or electron/hole pairs. p-n junction, p-i-n junction and heterojunction are illustrated respectively for charge dissociation in inorganic, amorphous silicon, and organic solar cells. The charge dissociation mechanism in organic-inorganic halide

perovskite is still not clear. Ferroelectric domain and built-in electric fields are two proposed mechanisms. Their limitations are analysis in detail.

3.3. Charge transportation and collection

As the electrons and holes are separated they need to be "safely" transported to the collection electrode in order to avoid recombination. Charge carrier mobility, effective mass, scattering time, etc. are the affecting factors. Influences of composition, surface integrity, grain size and grain boundaries, device configuration design are also discussed. Strategies of process control and device configuration design to gain efficient charge transport and collection are proposed.

4. Reliability and stability

Success of the solar cell in real application lies largely on its reliability and stability. This section focus more on perovskite cells as they have great application potential but yet encounter the biggest problem in this regard. These includes appearance of the hysteresis in I-V curve, the degradation mechanism of perovskite solar cell against environmental parameters, such as heat, moisture, oxygen, light and interface, are thoroughly explained and improvement strategies discussed.

5. Summary

The key obstacles in the four major cell categories are summarized and direction for breakthrough pointed out. Also summarized are the strategies in achieving high efficiency solar cells in each and every critical stage.

1. Introduction

Currently single crystal silicon (Si) solar cell exhibits a conversion efficiency of about 25% and has dominated the solar cell market. However, due to low light absorption and indirect bandgap features, single crystal Si layers of around 200~250 μm in thickness are usually needed to efficiently harvest the sunlight. It has been widely used in solar farms and building roofs. This, however, is not suitable for integrated photovoltaic, such as windows and facades, nor for electronic devices that require flexibility and transparency. Therefore, thin film solar cells

emerged and have attracted increasing attention. In this review, we start from the design rules and strategies for high efficient thin film solar cells, in an attempt to provide better design guidance for veterans and an effective introduction to newcomers. Thin film solar cell examples covered in this review are mainly of the following four categories: polycrystalline inorganic [$Cu(In,Ga)(S,Se)_2$ (or CIGSSe for short), $Cu_2ZnSn(S,Se)_4$ (or CZTSSe)], amorphous silicon (a-Si), organic photovoltaics (OPV) and organic-inorganic halide perovskite (perovskite) and etc.

This review is organized into five sections. Section 1 is this introduction. Section 2 illustrates solar cell basics and the origins of thin film solar cells. Section 3 dives into how to obtain high efficiency. Section 4 focuses on the reliability and stability in perovskite cells and finally section 5 summarizes the whole review and highlights the key bottleneck in each of the four categories.

2. Thin film solar cells

The efficiency of conversion of light into electrical power, or simply termed conversion efficiency, is defined as the ratio of the output electricity to the input energy of sunlight. In practice, the power conversion efficiency (η) of a solar cell is defined as the ratio of the maximum power output, P_{max}, generated by the solar cell to the power input, P_{in}, based on the measurement of current density and voltage (*I-V*) curve :[1]

$$\eta = \frac{P_{max}}{P_{in}} = \frac{J_{mp} \cdot V_{mp}}{P_{in}} = \frac{J_{sc} \cdot V_{oc} \cdot FF}{P_{in}} \quad (1)$$

Where J_{mp} and V_{mp} are the current density and voltage at the maximum power point (c.f., Fig. 1), J_{sc} is the short circuit current density, V_{oc} is the open circuit voltage, and *FF* is the fill factor. Fig. 1 is a typical *I-V* curve used in solar cell efficiency illustration.

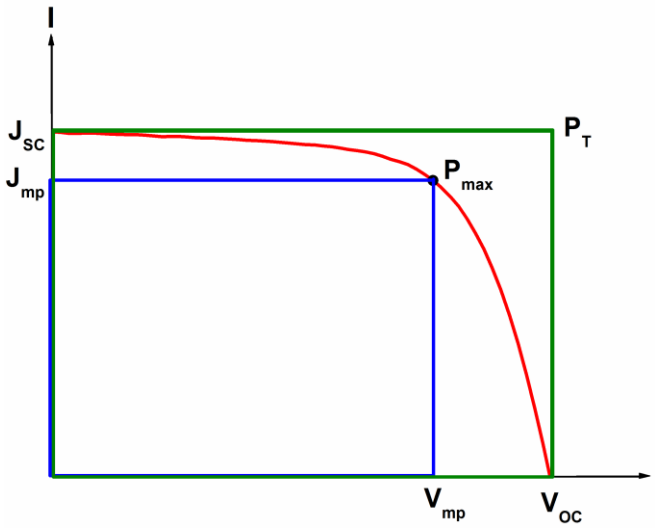

Fig. 1. A typical *I-V* curve in solar cell efficiency illustration

The fill factor *FF* is introduced to simplify the calculation of the efficiency, and is defined as the ratio of the areas of the two rectangles determined by J_{mp} and V_{mp} (blue in Fig. 1) and by V_{oc} and J_{sc} (green in Fig. 1), respectively. Accordingly, the three parameters of V_{oc}, J_{sc} and *FF* combine to compute the efficiency of a device. The open circuit voltage V_{oc} is, in theory, determined by the energy difference of quasi-Fermi levels between *p*- and *n*-type semiconductors under illumination. The short circuit current density J_{sc} is a product of 3 aspects of efficiency: light harvesting, charge separation and charge collection. The light harvesting efficiency is dependent on the absorbance of a semiconductor.

Based on the photoelectric phenomenon, two factors should be of concern in producing more photoelectrons: bandgap energy and incident photon energy. As seen in Fig. 2, semiconductors that have bandgap higher than 3.1 eV can only absorb ultraviolet (UV, wavelength of 280-400 nm) light. For a semiconductor that has a bandgap of 1.77 eV, all of UV and visible light (VL, wavelength of 400-700 nm) are able to excite electrons from valance band to conduction band, but not the infrared portion (IR, wavelength of 700-4000 nm). The visible and infrared light (VL and IR) accounts for 43.0% and 52.5% [AM 1.5G according to ASTM G173] of the total energy of solar spectrum, respectively.

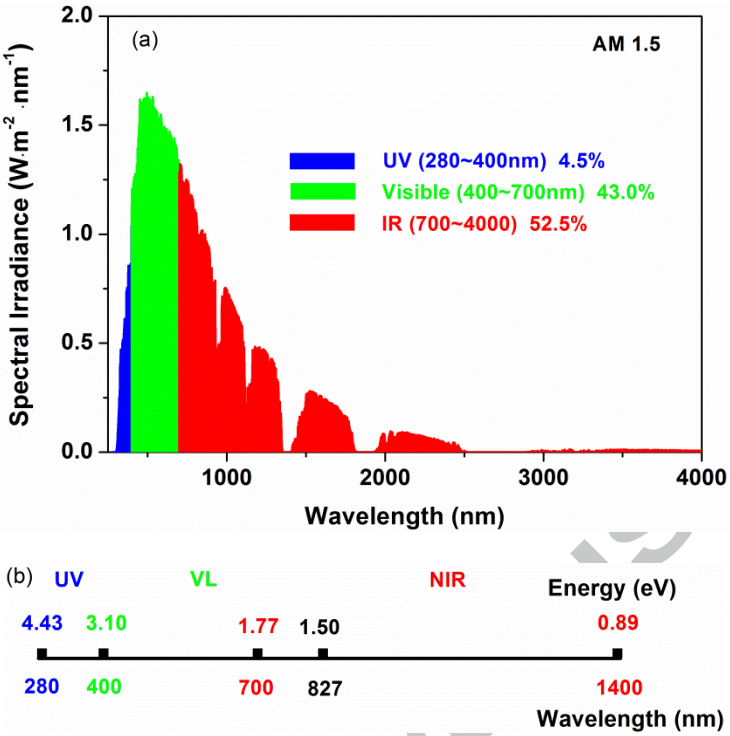

Fig. 2 (a) energy distribution of solar spectrum (as determined by AM 1.5G according to ASTM G173) and (b) the corresponding energy level and wavelength

We focus our attention to polycrystalline inorganic, organic photovoltaics, amorphous silicon and organic-inorganic halide perovskite cells. As epitaxial III-IV group thin film solar cells are based on single crystal films thus not covered in this review.

2.1 Polycrystalline inorganic cells

In this category of solar cells, the most famous ones are $Cu(In,Ga)(S,Se)_2$ or CIGSSe and $Cu_2ZnSn(S,Se)_4$ or CZTSSe. For a long time it is believed that grain boundary is detrimental to solar cell performance since it causes serious recombination. However in materials like $CuInSe_2$, because of the special chemical structure, the grain boundary shows low recombination velocity which allows high efficiency solar cell even when polycrystalline materials with grain size of a few microns. This is a revolution from single crystal to polycrystalline thin film solar cells. Bell Telephone Laboratories first reported $CuInSe_2$ (CISe) single crystal solar cell with an efficiency of ~5% in 1974 [2, 3]. Later gallium (Ga) and Sulphur (S) were introduced to CISe system to obtain CIGSSe with a recording efficiency of 21.7% [4, 5]. CIGSSe is a

direct bandgap semiconductor with light absorption coefficient much higher than conventional silicon. Also, its bandgap can be adjusted by composition design to match the optimized bandgap according to solar spectrum (around 1.5 eV). As a result, CIGSSe of only several microns is thick enough to absorb sufficient photon energy.

In light of the cost saving, efforts were made to eliminate the use of In and Ga. Complete replacement of In with Zn and Ga with Sn gave rise to $Cu_2ZnSn(S,Se)_4$ or CZTSSe [6, 7], but with an efficiency of less than 13% even up to date. Analysis of this problem is given in Section 3.

2.2 Amorphous Si (a-Si:H)

The first amorphous silicon (a-Si) layer was reported as 'silicon from silane' in 1965 by Sterling and Swann through chemical vapour deposition [8]. However, less attention was paid at that time as compared to single crystal Si. For the latter, each silicon atom is covalently bonded to four neighboring atoms. In contrast, the a-Si has extremely high density of dangling bonds (as shown in Fig. 3) and hence high density of intra-gap states (10^{21} cm^{-3}) [9], which induce immediate recombination of carriers and pins the energy level. Until ten years later, Spear and LeComber [10] reported that the conductivity of a-Si can be controlled over many orders of magnitude through incorporating phosphine or diborane gas during deposition. It was later recognized that hydrogen plays an important role in a-Si, which passivates most of the dangling bonds and reduces the trap density to around $10^{15\text{-}16}$ cm^{-3} (cf. Fig. 3 where those with small circles are passivated bonds) [9]. The hydrogen alloying happens during the deposition of a-Si film since SiH_4 is widely used as precursor. Therefore a-Si is often called hydrogenated amorphous silicon denoted as a-Si:H.

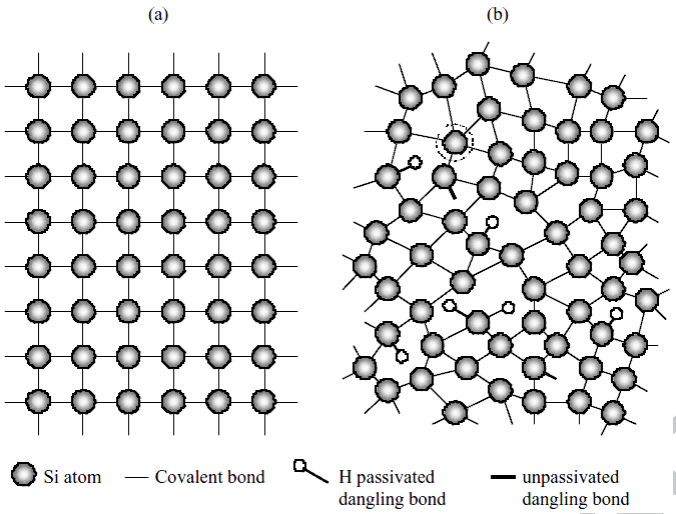

Fig. 3 Schematic representation of the atomic structure of (a) single crystal silicon, (b) hydrogenated amorphous silicon. Reprinted with permission from ref. [9]

Compared to single crystal Si, the a-Si:H exhibits a high absorption coefficient in visible light range. A thickness of 1 μm is sufficient to absorb 90% of the usable solar energy. Besides, large area of a-Si:H can be processed by chemical vapor deposition at relatively low temperature (100~400°C). Due to these advantages and earth abundant Si, a-Si:H attracts more interests. However, the long range disorder nature of a-Si:H hinders the carrier mobility and diffusion length. A highest stable conversion efficiency obtained to date is 13.6% [4].

2.3 Organic photovoltaics

Thin film organic photovoltaic (OPV) is developed in parallel, where organic materials are prepared by solution-based process [11]. Similar to planar *p-n* or *p-i-n* junction of inorganic solar cells, organic planar devices were first produced with an efficiency of only around 1%. As the diffusion length is too short, the excitons are difficult to reach the heterojunction to dissociate into free electrons and holes before they get annihilated. Breakthrough originates from the concept that a bulk distributed interface to efficiently capture and dissociate excitons, named as bulk heterojunction [12]. The low-cost and flexible feature makes the OPVs a good candidate for cost-effective photovoltaics [13], although the state-of-the-art efficiency is still below 12% [14].

2.4 Organic-inorganic halide perovskite

As an extension of the idea of bulk distributed interface in OPVs, Graetzel developed dye-sensitized solar cells (DSSC, also called Graetezl cell), in which a porous titanium dioxide (TiO_2) nanoparticles is formed on the top of compact TiO_2 layer. A monolayer of organic sensitizer is absorbed on the nanoparticles and liquid electrolyte of redox couples fills up the pores. Under illumination, the excited electrons produced by the sensitized molecules inject into the conduction band of TiO_2. The sensitizers are recovered by the electrons supplied from the liquid electrolyte within the pores [15]. The Graeztel cell separates the absorption, the charge transport and collection processes in a photovoltaic device. Miyasaka and coworkers first use inorganic-organic halide perovskite as the sensitizer in DSSC and achieved an efficiency of 3.8% with a high photovoltage of 0.96V [16]. A breakthrough was made in 2012 by Park, Graetzel and coworkers using a solid-state hole transporting materials instead of liquid electrolyte to achieve an efficiency of 9.7% [17]. Since then, organic-inorganic halide perovskite solar cells (hereafter referred to as perovskite) quickly dominate the research field in view of the high conductivity, fast charge mobility, long diffusion length, and thus a high powder conversion efficiency [18]. An absorber thickness of several hundreds of nanometers from solution process is sufficient to generate an efficiency of over 20% [19].

3. Strategies towards high efficiency

3.1 Light harvesting

As discussed afore, increasing of light harvesting efficiency relies on two aspects: decreasing the bandgap and managing the photons. The bandgap of a semiconductor is closely related to the interaction between atomic nucleus and shell electrons (i.e. Coulomb interaction), and between electrons and electrons (i.e. chemical bonding). The stronger the interaction, the wider the bandgap thus the larger the energy requires to excite electrons from valance band to conduction band. Besides, the symmetry of electron cloud distribution will also affect these interactions. For instance, s-orbit electron has symmetric distribution and thus can move easier than other p or d-orbit electrons. Silver has the best conductivity is due to its loosely-held single symmetric s-shell valence electrons. Therefore, the composition and structure of a semiconductor determine its bandgap. As such, altering the composition and structure hold the keys in adjusting the bandgap. On the other hand, the photons of lower energy such as the IR photons can be moved to

a higher energy level thus are able to be absorbed in a semiconductor with a higher bandgap, the efficiency of light harvesting is improved. A high energy photon can also be divided into two or more photons with lower energy. If, however, absorption is controlled so that the visible light passes through or partly passes through, transparent or semitransparent solar cells are realized. These will be discussed in details below, together with multi-junction and quantum dot solar cells.

3.1.1 Bandgap adjustment

A semiconductor can only absorb photons whose energy is higher than its bandgap E_g. However, photons bearing much higher energy than *Eg* can excite electrons to energy levels above conducting band minimum (CBM), and subsequently the electrons rapidly relax to the CBM by releasing the extra energy as heat. Consequently, there exists optimal bandgap energy for photovoltaic application. Shockley and Queisser calculated the theoretical conversion efficiency to be around 31% for single junction solar cells [20]. Green proposed a simple empirical relation that can be used to reasonably estimate the minimal value of the reverse saturation current density. As such, the optimum *Eg* should be around 1.5 eV, which agrees well with the experimental data [21, 22].

In order to manipulate the bandgap, let's first examine the formation of the bandgap and what affect it. By definition, bandgap is the energy difference between conduction band minimum and valance band maximum. The conduction band and valance band are formed by the interaction of shell electrons within the semiconductor. Stronger interaction between atomic nucleus and shell electrons, and/or stronger interaction between electrons and electrons forming tightly bonded chemical bonds, leads to larger *Eg*. As such, the bandgap can be tuned by substituting elements with different electronegativity. Atoms of larger size have relatively weaker attraction to its shell electrons therefore smaller bandgap *Eg*, thus the valance electrons escape easier. Similarly, crystal lattice parameters, i.e., the size of unit cell also affect bandgap *Eg* by changing the strength of chemical bonds. The larger the unit cell, the weaker the attraction between atoms, giving rise to smaller bandgap *Eg*. Below we examine the effect of composition and effect of structure separately.

Effect of Composition

In copper indium sulfide (CIS), the valance band (VB) is formed by the interaction of copper (Cu, $3d^{10}4s^1$) *d*- and sulfur (S， $3s^23p^4$) *p*-orbit electrons, and the conduction band (CB) is formed by the overlap of Indium (In， $4d^{10}5s^25p^1$) *s*- and sulfur (S) *sp*-orbits [23]. Therefore, replacing any In atoms with other elements affects the position of the conduction band of the compound, while replacing S causes moving of both CB and VB. Research shows for $CuInS_2$ the bandgap *Eg* is around 1.53 eV. Substituting In with smaller atomic size Ga in the same group (c.f., Table 1), the position of the conduction band minimum is raised as the outer electrons in Ga are bond with stronger interaction. Consequently, for $CuGaS_2$ the *Eg* is 2.43 eV [23], that is a large increase from that of 1.53 eV for $CuInS_2$. Complete substitution of S with larger atomic size selenium (Se) decreases *Eg* to 1.04 eV for $CuInSe_2$ (CISe). As such, proportional substitution of Sulfur results in tunable bandgap from 1.04 eV to 2.43 eV, as in the case of CI(G)S(Se). The second column in Table 2 lists bandgap change as composition varies. The device performance reveals that the highest efficiency of the CI(G)S(Se) system is obtained with a bandgap *Eg* of around 1.1~1.2 eV, rather than the optimal 1.5 eV [24-26]. This will be discussed in light of charge carrier mobility in section 4. Substitution of In and Ga in CIGSSe with Zn and Sn formulates CZTSSe or $Cu(ZnSn)(S,Se)_2$, similar trend in bandgap change is observed, i.e., replacing of S with bigger atomic size Se gives rise to smaller bandgap *Eg* (0.82 ~1.48 eV, c.f., Table 2). Replacing of In and Ga with Zn and Sn is for economic reason. An optimum efficiency of 12.6% was obtained at an S:Se ratio of around 1:4 [5]. In organic-inorganic perovskite ABX_3 system, a mix of 85% $CH(NH_2)_2PbI_3$ and 15% $CH_3NH_3PbBr_3$ gives rise to an efficiency of 20.3% with a bandgap of 1.49 eV [19]. By the way, from Table 2, a rule of mixture with regard to the bandgap gives rise to 1.48 eV for 85% $CH(NH_2)_2PbI_3$ and 15% $CH_3NH_3PbBr_3$. Table 2 also lists other important parameters often used in solar cell characterizations: effective mass (m^*) of charge carriers, dielectric constant (ε_r), exciton bonding energy(E_b), and etc. These will be defined in details in section 3 and section 4 where charge dissociation and collection are discussed.

Table 1 Section of the periodic table

		IIIA	IVA	VA	VIA	VIIA
		5 **B** $1s^22s^22p^1$	6 **C** $1s^22s^22p^2$	7 **N** $1s^22s^22p^3$	8 **O** $1s^22s^22p^4$	9 **F** $1s^22s^22p^5$
IB	IIB	13 **Al** $3s^23p^1$	14 **Si** $3s^23p^2$	15 **P** $3s^23p^3$	16 **S** $3s^23p^4$	17 **Cl** $3s^23p^5$
29 **Cu** $3d^{10}4s^1$	30 **Zn** $3d^{10}4s^2$	31 **Ga** $3d^{10}4s^24p^1$	32 **Ge** $3d^{10}4s^24p^2$	33 **As** $3d^{10}4s^24p^3$	34 **Se** $3d^{10}4s^25p^4$	35 **Br** $3d^{10}4s^24p^5$

47 **Ag** $4d^{10}5s^1$	48 **Cd** $4d^{10}5s^2$	49 **In** $4d^{10}5s^25p^1$	50 **Sn** $4d^{10}5s^25p^2$	51 **Sb** $4d^{10}5s^25p^3$	52 **Te** $4d^{10}5s^25p^4$	53 **I** $4d^{10}5s^25p^5$
79 **Au** $5d^{10}6s^1$	80 **Hg** $5d^{10}6s^2$	81 **Tl** $5d^{10}6s^26p^1$	82 **Pb** $5d^{10}6s^26p^2$	83 **Bi** $5d^{10}6s^26p^3$	84 **Po** $5d^{10}6s^26p^4$	85 At $5d^{10}6s^26p^5$

Table 2 Electrical and physical parameters of commonly used compounds for solar cells

Materials		*Eg* (eV)	$m^*_e(m_o)$	$m^*_h(m_o)$	m^*	ε_r	$E_b(meV)$ (calculated)	Reference
Chalcopyrite and kesterite	$CuInS_2$	1.53	0.16	0.39				[23, 27, 28]
	$CuInSe_2$	1.04	0.08	0.14				[23, 27-29]
	$CuGaS_2$	2.43	0.24	0.91				[23, 27]
	$CuGaSe_2$	1.68	0.13	0.47				[23, 27]
	$Cu(In,Ga)S_xSe_{1-x}$	1.04-2.43	0.09	0.66-0.72	0.08-0.09	12-13.5	5.97-8.50	[23, 30-35]
	$Cu_2ZnSn(S,Se)_4$	0.82-1.48	0.1-0.2	0.29-0.48	0.07-0.14	6.79-8.59	12.90-41.30	[36, 37]
hydrogenated amorphous silicon (a-Si:H)			0.34	0.34	0.17	13.5	12.68	[38, 39]
Halide perovskite	$CH_3NH_3GeI_3$	1.6						[40]
	$CH_3NH_3SnI_3$	1.3	0.13	0.25				[41-43]
	$CH_3NH_3PbI_3$ or $MAPbI_3$	1.55	0.19	0.28	0.11	25.7	2.33	[43-48]
	$CH_3NH_3PbBr_3$	2.32						[49]
	$CH_3NH_3PbCl_3$	3.1						[50]
	$CsPbI_3$	1.73						[44, 46]
	$CH(NH_2)_2PbI_3$ or $FAPbI_3$	1.47						[44]
Organic photovoltaics (OPV)			1.3	0.94	0.55	2-4	467.5-1854	[51-53]

Effect of Structure

The effect of structures is discussed in terms of lattice structures and dimensional structures.

Figure 4 illustrates the perovskite structure originating from the mineral structure of $CaTiO_3$, where Ca or A forms simple cubic and Ti or B sits in the center while O or X occupies the face-center positions, giving rise to 1A, 1B and 3X atoms in a basic lattice cell, i.e., ABX_3. When X is O, i.e., in ABO_3, A and B must be divalent and tetravalent cations respectively, for instance, Ca^{2+}, Ti^{4+}. For solar cell applications, replacing O with monovalent halogen (e.g., I^-) results in lower bandgap thus are

widely used. In this case, A site should be monovalent cations and B site should be divalent for charge neutrality, such as those from the IVA group in Table 1, or Pb, Sn and so on. Monovalent cations at A site can be anything metallic (such as Cs, Rb, etc.) or organic groups (such as methylammonium ($(CH_3NH_3)^+$, or MA^+), formamidinium ($[CH(NH_2)_2]^+$, or FA^+), etc.) as long as the structure factor permits, as illustrated in Fig. 4.

In addition to compositional change of B-site metal and X site halogen elements gives rise to modulation of bandgap as discussed before, lattice dilation in perovskite due to A-site being occupied by organic group results in another dimension of bandgap modulation. With the ionic size of A site cation increases from 1.80 Å for Cs^+ to 2.17 Å for $(CH_3NH_3)^+$ and to 2.53 Å for $[CH(NH_2)_2]^+$ (c.f., Fig. 5) [54, 55], the unit cell size of $APbI_3$ increases from 222 Å to 248 Å and to 256Å [54]. Consequently, the bandgap reduces from 1.73 eV for $CsPbI_3$ to 1.55 eV for $CH_3NH_3PbI_3$ and to 1.47 eV for $CH(NH_2)_2PbI_3$ [44]. The distortion of the unit cell causing by the orientation or twist of organic cation in A side might also affect the chemical bonding and thus bandgap of perovskite.

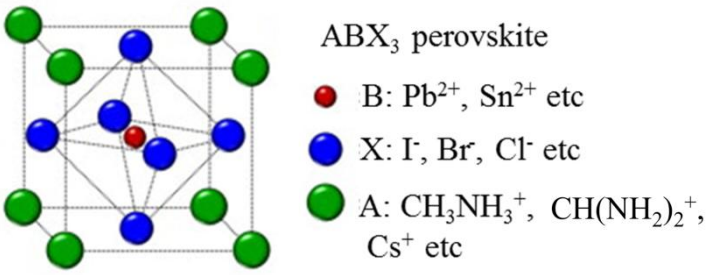

Fig. 4 Perovskite crystal structure. Reprinted with permission from ref. [56]

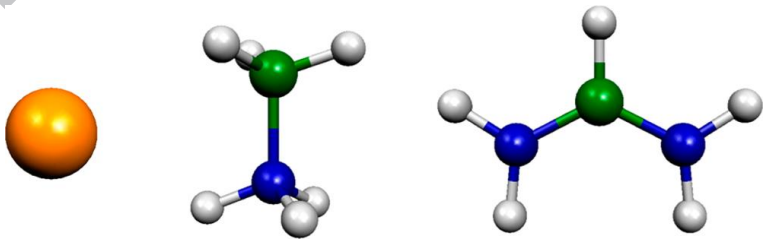

Fig. 5 Structure and illustration of size of Cs^+, Methylammonium $(CH_3NH_3)^+$, and Formamidinium, $[CH(NH_2)_2]^+$ cations. Reprinted with permission from ref. [54]

Further increasing the A site cation size, however, brings in destruction to the ABX_3 structure, because maintaining a stable 3D ABX_3 perovskite structure needs the

radii R_A, R_B and R_X of the A, B and X ions respectively satisfy certain relationship such that $t = (R_A + R_X)/\{\sqrt{2}(R_B + R_X)\} \approx 1$, or 0.813 to 1.107 [57], where t is termed tolerance factor first introduced by Goldschmidt [58]. In addition, B site and X site ions must meet the requirement of $0.442 < R_B/R_X < 0.895$ to maintain stable six-fold coordination octahedral structure BX_6 [57]. Smaller t gives rise to lower symmetry while too large a t destroys the perovskite's B-X network, causing formation of 2D layered structure. In Fig. 6, n=∞represents the 3-D structure of perovskite. As A site size increase, it breaks up the structure into layers depending on the amount [59]. Reading from the right to the left hand side, Fig. 6 shows a 3D (n=∞), 3-layer (n=3), 2-layer (n=2) and 1-layer (n=1) structures.

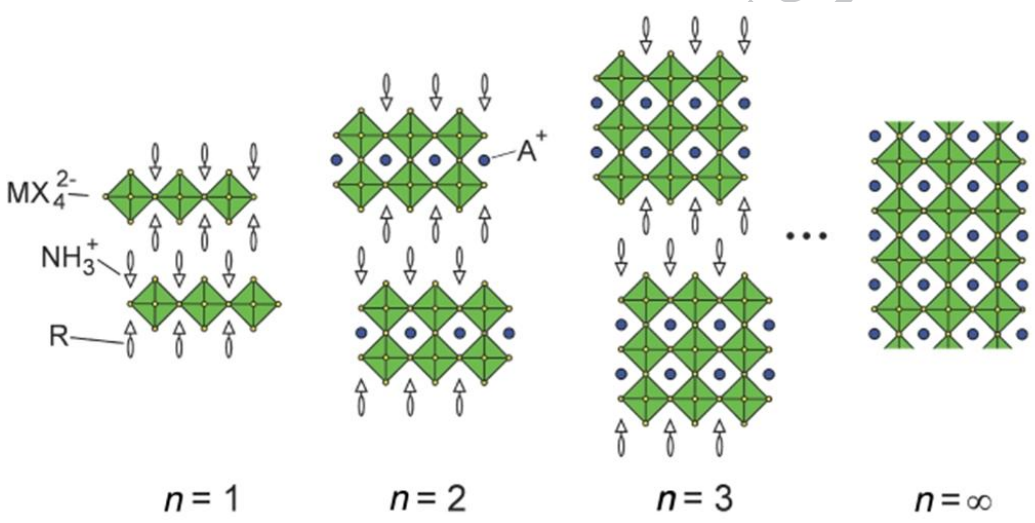

Fig. 6 The stacking of inorganic octahedral layer (n) with organic cation RNH_3^+ in the ⟨100⟩-oriented 2D perovskite. When n is ∞, it is 3D structure. Reprinted with permission from ref. [59]

In layered structure, the dielectric confinement and quantum effect should be taken into consideration. The dielectric confinement phenomenon describes a situation whereby a layer of material with a higher dielectric constant is sandwiched between two layer of materials with lower dielectric constant (ε_1 and ε_2), the effective thickness of electron-electron interaction within the higher dielectric constant layer is shortened, indicating much stronger interaction [60]. These layered structures are a natural quantum well structure, in which the inorganic sheets and organic molecules act as "well" and "barrier", respectively. The size and composition of the intercalated organic molecule, the numbers of stacking inorganic layer, all will affect the value of bandgap. In Fig. 6, the green layer or MX_4^{2-} layer is the higher dielectric constant layer (for instance, a 2D PbI_6

has a high dielectric constant of ε = 6.1) and the open arrows layer or the RNH_3^+ layers are the lower dielectric constant layers (ε_1 = 2.1 for $C_9H_9NH_3$) [61]. In the dielectric confined layer, electron-electron interactions are effectively stronger that, in turn, widens the bandgap. When the structure changes from 3D to 2D and further to 1D and 0D, 3D ABX_3 perovskite structure changes into A_2BX_4, A_3BX_5 and A_4BX_3 while the bandgap increases from 1.65 eV to 2.43 eV and to 2.70 eV and further to 3.33 eV sequentially as shown in Fig. 7 [62].

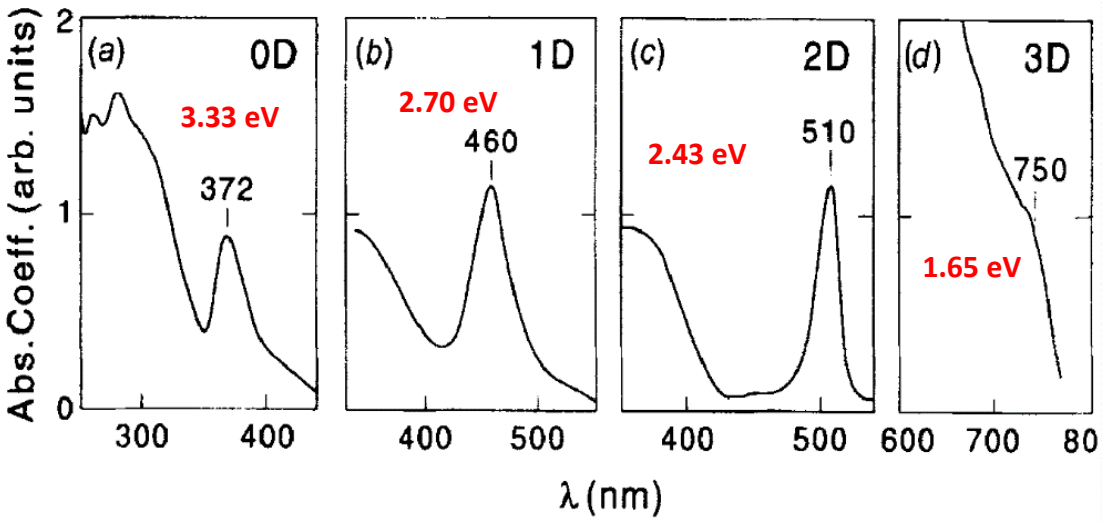

Fig. 7 Room temperature absorption coefficient as a function of wavelength (λ) for (a) $(CH_3NH_3)_4PbI_3$, (b) $[(NH_2C(I)=NH)_2]_3PbI_5$, (c) $(C_9H_9NH_3)_2PbI_4$, (d) $CH_3NH_3PbI_3$. These systems consist of OD. ID, 2D, and 3D extended inorganic networks of corner-sharing PbI_6 octahedra [62]

3.1.2 Light utilization

When the working layer (the "absorber") is thin, transmission of light is unavoidable. To make use of this transmitted light, one can stack cells in a serial manner thus the transmitted light from the top cell can be made into work in the cells beneath; this is the so-called "tandem" design. A reflector can also be used to turn the transmitted light back into the absorber for a second absorption. Generation of more than one electron-hole pair from one photon absorption (multiple exciton generation) is a new way of maximizing utilization of light. Photons of longer wavelength not having enough energy can be "up-converted" to gain higher energy thus are used in

photoelectron excitation, photons having too high an energy can also be "down-converted" to use in the excitation. These ways of maximizing the utilization of incident light are discussed here.

Minimizing Light Transmission

To efficiently minimize the transmission of light through the cell, tandem design or reflector is used. In tandem design, two or more cells are stacked one on top of another so that the transmitted light can be used in the cells below.

In Fig. 8, two solar cells are stacked in "tandem" manner: light travelled through the top perovskite cell continues on to enter the bottom CIGS cell. From the perovskite cell around 72% transmits in the near infrared range (c.f. Fig. 8(b)), which is then utilized by the bottom cell. The external quantum efficiency (EQE) shown in Fig. 8(c) confirms superimposition of the individual subcells, giving rise to a total conversion efficiency of 20.5% from the individual 14.2% for the top and 6.3% for bottom cell.

Tandem arrangement theoretically suits all cells. Yang's group stacked two polymer thin film cells of 4% efficiency in tandem architecture to improve to more than 7% and purposely let through a transparency of 30% in visible light [63] in an attempt for transparent solar cell. Graetzel, Segawa and coworkers [64] hybridized perovskite cell to absorb the visible light up to ~800 nm and wideband dye-sensitized solar cells to absorb NIR wavelength up to ~1100 nm to achieve an efficiency of 21.5% with current density up to 30 mA/cm^2.

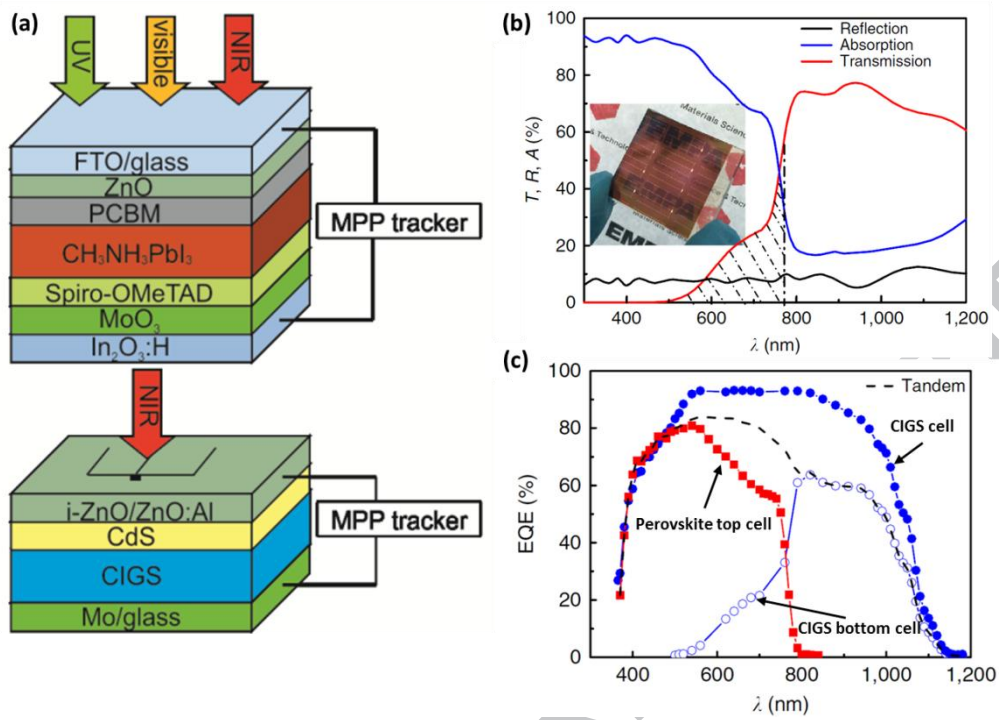

Fig. 8 (a) schematic 4-terminal tandem solar cell, (b) the transmission (T), reflection (R) and absorption (A) of top perovskite cell, and (c) external quantum efficiency (EQE) spectra of the four-terminal tandem device. Reprinted with permission from ref. [65]

Another way of minimizing the light transmission is to use a reflector to switch the transmitted light back into the cell for second absorption, as demonstrated in Bragg reflector [66], layered light-trapping architecture [67], photonic crystals reflector [68] and others [69, 70].

Maximizing photon excitation

Usually one photon excites one electron-hole pair. Can one photon excite multiple excitons? Quantum dot (QD) is nano-sized particle with dimension smaller than its Bohr radius, at which quantum effect occurs. In bulk semiconductors where exist large amount of atoms, above the bandgap there are many energy states with very small energy gap. The excited electrons of much higher energy rapidly relax onto the conduction band minimum, and the photon energy in excess of band gap is wasted as heat, as shown in Fig. 9(a) [71]. In a quantum dot, however, as the number of atoms in the dot is limited (100-10000 atoms per dot), there does not exist such small energy states, but discrete ones with energy separation between energy states much higher than the phonon energy. The relaxation of excited electrons slows down due to the existence of discrete quantized energy levels. The phonon energy of heat cannot transfer out quickly due to the limited amount of atoms; the excitons in QD are normally hot. The slow relaxation of these hot exciton allows possibly excite

another electron thus creating more than one electron-hole pairs per photon, called multiple-exciton-generation as illustrated in Fig. 9(b). This, however, only happens when the initial photon energy is at least two times that of the bandgap *Eg*. Beard et al [72] first reported this multiple-exciton-generation effect in PbSe QD solar cells when measured external quantum efficiency becomes more than 100% (under one sun solar intensity with no external applied bias). Recently Greenham et al. [73] reported external quantum efficiency above 120% by sandwiching PbTe QD between ZnO and MoO_x layers as shown in Fig. 9(c) and (d). The main drawback of Quantum Dot solar cell is the high recombination rate and poor charge collection efficiency.

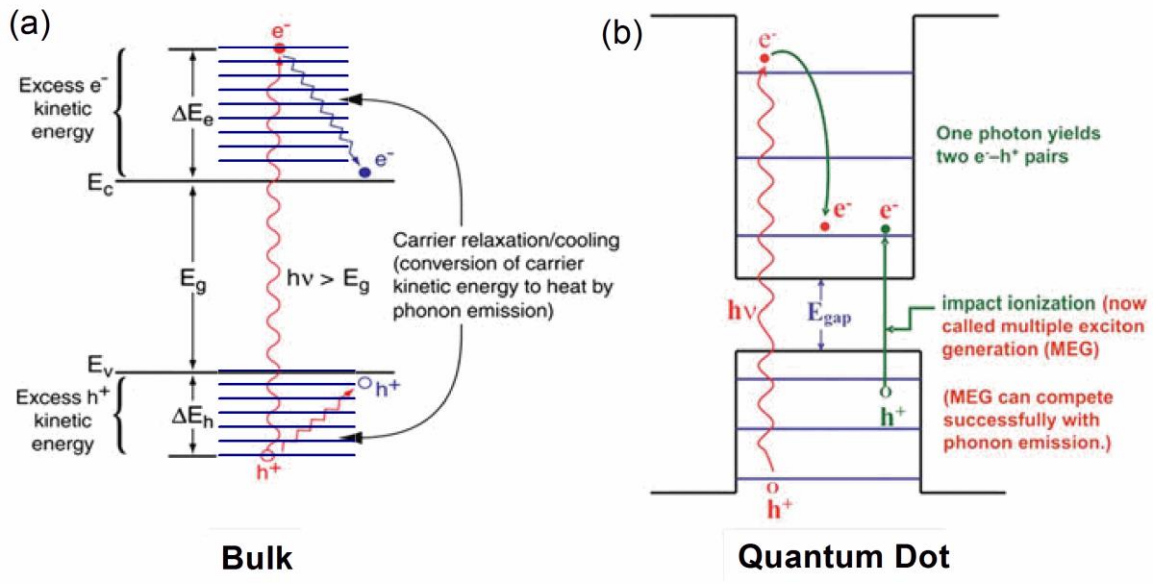

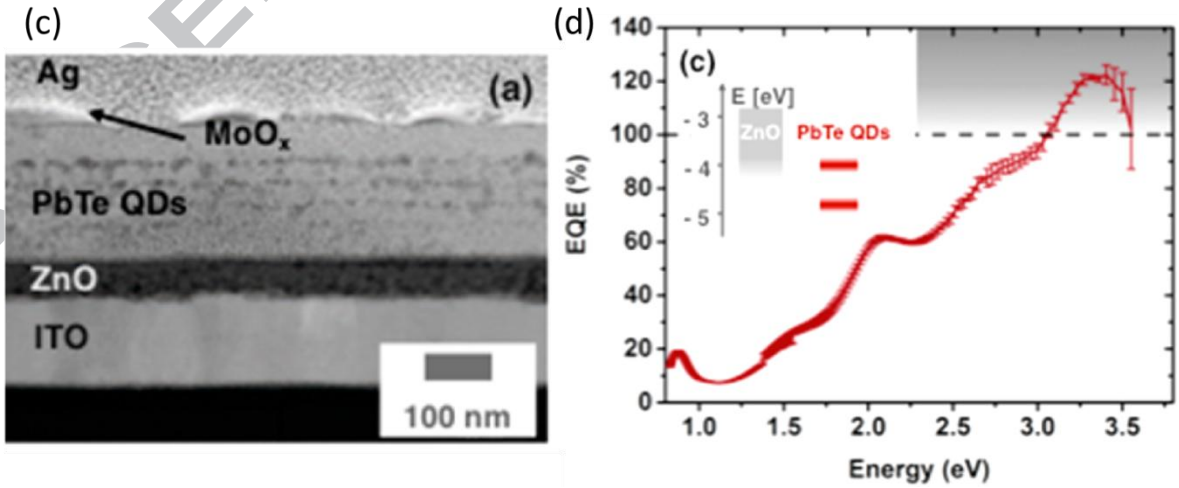

Fig. 9 (a) Hot carrier relaxation/cooling in bulk semiconductors (b) Multiple electron–hole pair generation in quantum dots, (c) the cross section microscopy and (d) EQE of PbTe QD solar cell. (a) and (b) reprinted with permission from ref. [71] , (c) and (d) from [73]

When the incident photon has much higher energy than that needed to excite an electron, one way of making use of this "extra" energy is quantum dot architecture, as mentioned above, another way is to down-convert the photon into two or more with lower energy that excite two or more electron and hole pairs. Down conversion is very useful for low bandgap semiconductors. Fig. 10 illustrates the down-conversion process where one photon with higher energy splits into two lower energy photons.

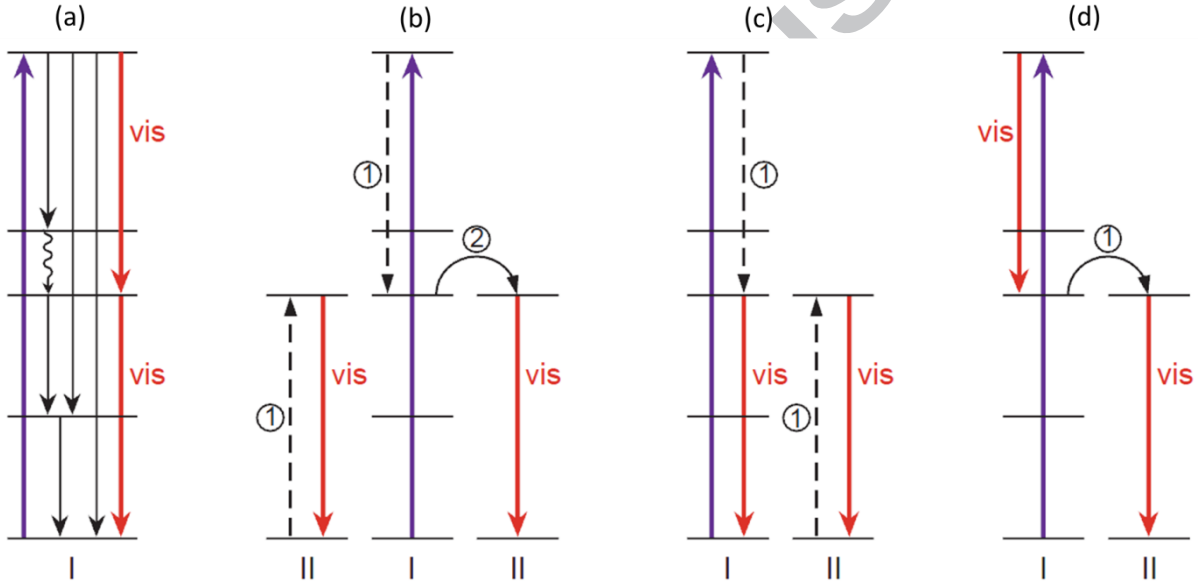

Fig. 10 Schematic illustration of down conversion [74]

In Fig. 10, europium doped lithium gadolinium fluoride (Eu^{3+}-doped $LiGdF_4$) has two types of lanthanide ions: Gd^{3+} or Ion I is the ion in the matrix as host material and Eu^{3+} or Ion II is doped in as energy acceptor [74]. In Fig. 10(a), a photon is excited in Ion I and split into two visible photons upon relaxation (marked as "vis" line). It may also possibly come down in steps as illustrated in the black line in Fig. 10(a) if the energy levels of matrix and acceptor ions are not matched. Actually, this high level photon (UV photo) could drop half way down and excites a photon in Ion II (marked ① at the "left type II ion" in Fig. 10(b), which gives out a visible light when returns to ground state) and at the same time, transfer the leftover energy to another Type II ion (to release in visible light upon its relaxation as marked "vis" at

the "right type II ion" in Fig. 10(b)). This UV photon could also relax through exciting a lower energy photon in Ion II (marked ① and "vis" in Fig. 10(c) as it gives out a visible light when returns to ground state) and at the same time emitting the leftover energy as a visible light photon in Ion I itself. Fig. 10(d) shows yet another possibility: the UV photon emits a visible light in Ion I itself and transfers the leftover to a Type II ion to relax as a visible light. Realization of the down conversion needs careful "architectural design" of ions with matching energy levels. The fundamental requirements for this high energy photon splitting to happen are: the energy gap between adjacent levels in host material must be large enough to prevent "multi-phonon relaxation" (where energy is relaxed through multiple phonons of very small energy levels that have no use in exciting photoelectrons); a good overlap between emission spectrum of the host ion and the excitation spectrum of the dopant ion or acceptor, i.e. the electron energy state of acceptor is same as the energy level in the middle of host ion's energy states [75]. For efficient energy transfer from host ion to dopant ion, these two ions should be physically close enough in space and defects should be carefully controlled to eliminate non-radiation energy losses.

Through this process, effectively one photon of high energy is split into two photons of lower energy. In Si solar cell, 32% extra spectral irradiance was obtained by down conversion strategy [76]. Theoretically, for a single crystal Si-based solar cell with an ideal down conversion layer, conversion efficiency up to 38.6% could be achieved as compared to the theoretic limiting efficiency of 30.9% [77].

In the solar spectrum, however, only a small portion of the energy is in UV range, a large amount of the energy lies in the IR or near IR range. The low energy IR light cannot be utilized to excite the electrons for large bandgap semiconductors. Fig. 11 illustrates the reverse to the down-conversion: the up-conversion, i.e., two photons of individual energy not enough to excite a photoelectron but they "team up" to excite one.

The concept of up conversion can be traced back to 1983 when Saxena studied thulium-doped calcium tungstate as a potential material [78]. Recent studies show that nanocrystals combined with molecular emitters are effective in realizing up-conversion of photons in the IR range. The nanocrystals absorb low energy photons and transfer the energy to the molecular triple state. When two of this kind of triple state superimposed, it creates high energy singlet states that emit up-converted light [79]. In Fig. 11, a possible potential strategy illustrates PbSe nanocrystal combines with rubrene, photons with wavelength of 980 nm and up-converts into that of 568 nm [79]. Other systems, such as CdSe, lanthanide doped chloride, bromide and iodide [80], oxyfluoride glass ceramics, [81] can also be found in the

literatures. Till date, however, the resultant quantum yield of the up conversion processes is still low because of unstable middle state. In Fig. 11, a photon excites an electron (let's say, electron A in PbSe) from $1S_h$ to $1S_e$ level with 1.32 eV, which then transfers to rubrene (RUB) and excite another electron (electron B in RUB) to lift to 1.14 eV (triplet or T* state) (with the difference being irradiated as heat). Now another photon subsequently hits electron B with another 1.14 eV, thus electron B is further lifted to 2T* or 2.28 eV that relaxes to 2.21 eV as electron C. As electron C drops from S_1 to its ground state S_0, a photon of 2.21 eV is created. As such, two photons of lower energy (1.32 eV 1.14 eV) are up-converted to a photon of much higher energy (2.21 eV) (with the difference being heat radiation). Later, upon absorption, this photon will eject a photoelectron with bandgap of 2.21 eV.

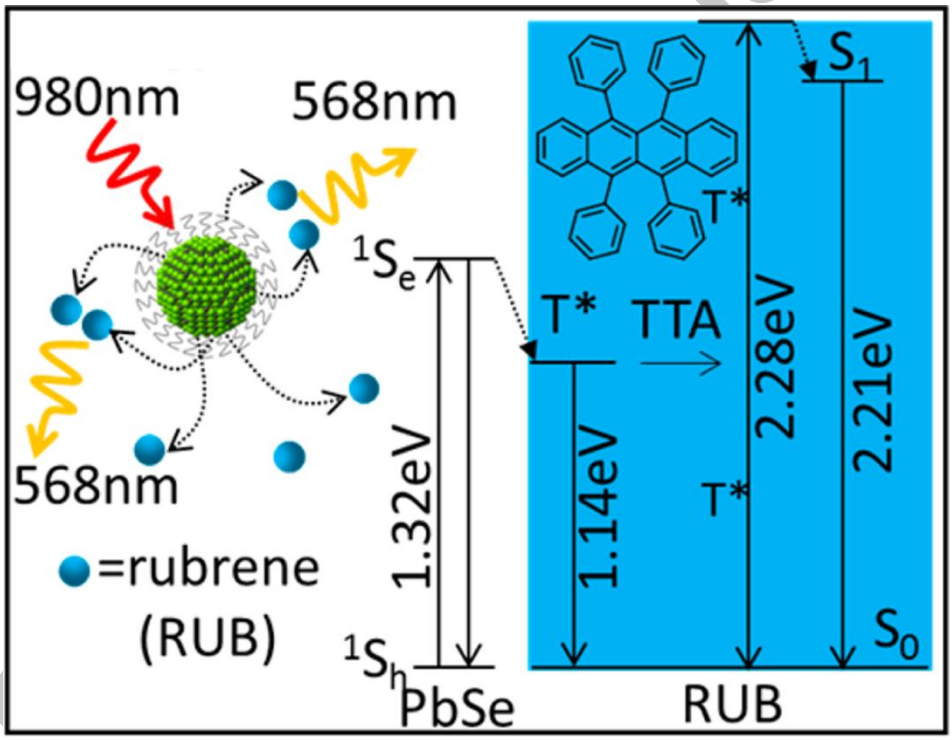

Fig. 11 Schematic illustration of a possible nanocrystal-organic up conversion strategies. Reprinted with permission from ref. [79]

The most critical thing in up conversion process is the short life time of triplet state. It should be longer enough until another photon come over and hit it further up. Therefore the light intensity should be very high, much higher than solar spectrum. This is why the up conversion efficiency is normally very low under solar illumination.

Wang et al [82] reported the significant improvement of photocurrent of solar cells by applying yttrium fluoride host doped with ytterbium and erbium in organic photovoltaic.. Shan et al [83] designed Er^{+3} and Yb^{+3} co-doped LaF_3-TiO_2 nanocomposite to absorb IR photons and realized up-conversion in dye sensitive solar cell. The enhancement in current density was around 3%.

3.1.3 Efficient yet transparent

If the light absorption layer is designed such that the visible light is allowed to transmit through the layer without absorption, other light bands (UV and/or NIR) are absorbed to generate photoelectrons, transparent solar cell is realized. If the visible light is partially absorbed, a partial transparent or semitransparent solar cell is created. When this solar cell is used onto window glass or building glasses, building/window glass will all generate solar power without hindering its "see-through" function.

However, visible light accounts for 43% of total solar energy. Allowing all visible light to pass through without doing anything greatly decreases the light harvesting efficiency and thus efficiency of the solar cell. Therefore, a big question lies in front of scientists is how to increase efficiency. Partial transparency (letting the visible light partially go through) solves part of the question. Fundamentally one has to fully utilize the UV and the NIR range radiations. As UV light has very high energy, thus the down conversion strategy discussed afore is useful. NIR light usually have too low an energy with respect to typical light absorbing materials used in solar cells, the up conversion strategy should come handy. Light reflector mentioned above is another strategy to improve the efficiency of transparent solar cell.

Partial transparency can be easily realized by simply making the solar cell thinner, trading off efficiency for transparency. Perovskite solar cell with power conversion efficiency above 6% with 30% device transparency was reported [84]. Ultra-thin CIGS [85, 86], InP [87] and Si [88, 89] semitransparent solar cells were tested this way resulting in different colors as the absorption peaks are in visible light range (the bandgap of all these solar cells are less than 1.5 eV).

Snaith's [90] group designed perovskite "islands" array (Fig. 12(a)) to solve the color tilting problem. The perovskite "islands" act as absorbers and produce electricity, while the voids between islands let the light go through completely. A 5.2% efficiency is thus realized at 28% transparency. The semitransparent device, tilted film surface SEM and cross-sectional SEM are also shown in Fig. 12.

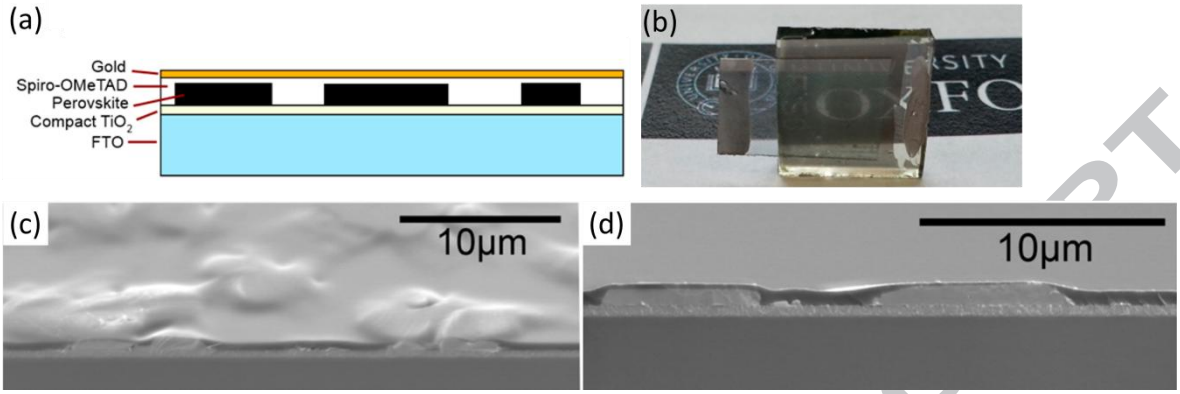

Fig. 12 (a) diagram of the device architecture, (b) digital image of a full semitransparent device, (c) tilted and (d) cross-sectional SEMs. Reprinted with permission from ref. [90]

Composition design can enlarge the bandgap of the absorber to target on only absorbing UV band of light plus small amount of visible light at higher energy edge. In halide perovskites, the bandgap *Eg* is continuously tuned up to 2.25 eV by substituting Iodine with Bromine. Bailie et al reported more than 12% efficiency with semitransparency with peak transmission of 77% at around 800 nm [91].

It is impossible for a single material to absorb both UV and IR photons at the same time while letting the visible light wavelengths to go through, thus two materials are mixed in which one targeting at UV and the other at IR. In this way, 4% efficiency [92] is reported at a maximum transparency of 66% at 550 nm wavelength. Similar results can be found in dye sensitized solar cells and others [93-96].

To increase the light intensity, a "concentrator" is used to concentrate light from a large area into a small one to enhance efficiency of transparent solar cell. In Fig. 13(a), the incident NIR light comes in from up-side is concentrated into Si solar cell located at both sides of it. A true (or total) transparent concentrator only makes use of NIR radiation and let all visible light to pass (c.f. Fig. 13(b) and (c)). Using the following luminophore blends of cyanine and cyanine salts, i.e. 2-[7-(1,3-dihydro-1,3,3-trimethyl-2H-indol-2-ylidene)-1,3,5-heptatrienyl]-1,3,3-trimethyl-3H-indolium (HITC) iodide (HITCI) and 1-(6-(2,5-dioxopyrrolidin-1-yloxy)-6-oxohexyl)-3,3-dimethyl-2-((E)-2-((E)-3-((E)-2-(1,3,3-trimethylindolin-2-ylidene)ethylidene) cyclohex-1-enyl)vinyl)-3H-indolium chloride (CY), a total transparent luminescent solar concentrator has been reported [97]. However the efficiency is <1% and need further improvement.

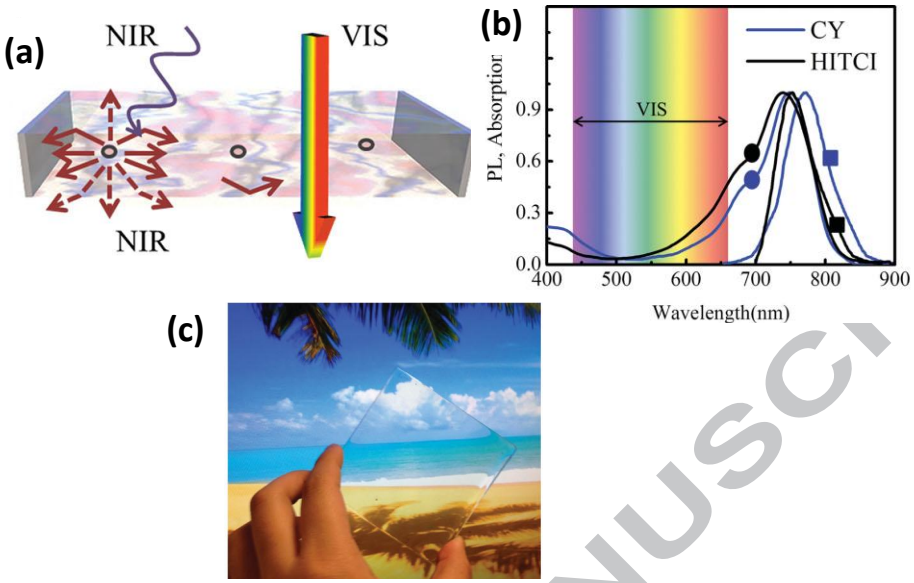

Fig. 13(a) Schematic of the transparent luminescent solar concentrator (b) Normalized absorption (circle symbols) and emission (square symbols) spectra of the NIR-absorbing luminophores CY (blue line) and HITCI (black line) films. (c) Photograph of the transparent luminescent solar concentrator system. Reprinted with permission from ref. [97]

3.2. Charge dissociation

After illumination, the generated electron and the hole must be separated to avoid recombination. Separation of the electrons and holes is called charge dissociation. In inorganic materials, electrons and holes are free to move separately (only a p-n junction is needed) but in organic materials the excited electron and the hole are in pairs (the so-called exciton) that can't move freely in separation. Therefore, for organic solar cells, special measures must be taken to separate the electrons and the holes, i.e., to break up the exciton and keeping them separated (using the so-called heterojunction). In organic-inorganic halide perovskite, the charge dissociation mechanism is not clear yet and several models were proposed. The efficiency of charge dissociation directly determines how many free charges one obtains.

The attraction force between an electron and a hole is called Coulomb attraction. In an exciton, an electron and a hole are "bonded" by this Coulomb attraction internally. Externally, however, exciton is electrically neutral, analogue to hydrogen atom but with different size and binding energy. The exciton binding energy is defined as the energy required separating an exciton into a free electron and a free hole. The radius of an exciton is called Bohr radius, which can be calculated by [98]:

$$a_B = \frac{\varepsilon}{m^*} \cdot a_H \tag{2}$$

where m^* is the reduced mass derived by $m^* = \frac{m^*_e \, m^*_h}{m^*_e + m^*_h}$, m^*_e and m^*_h are the effective mass of electron and hole, respectively, ε is the dielectric constant of material and a_H is the Bohr radius for the hydrogen atom. By introducing excitonic Rydberg energy, $R_y(H)$ = 13.6 eV, the binding energy (E_b) is determined as: [98, 99]

$$E_b = \frac{e^2}{\epsilon a_B} = \frac{m^*}{\varepsilon^2} Ry(H) = 13.6 \times \frac{m^*}{\varepsilon^2} \text{ eV} \tag{3}$$

Accordingly, the binding energy is directly related to the scale of reduced effective mass and dielectric constant, which determines the state of charge carries either in the form of free electrons and holes or bonded excitons. Table 2 lists the effective mass and dielectric constant of a few materials used for solar cells.

According to Eq. (3), the exciton binding energy is inversely proportional to the square of dielectric constant. Dielectric constant, also known as permittivity, is the resistance which encounters when applying an electric field in a medium. A higher value means charges can be separated easily inside its body. Compared to inorganic materials, organic molecules are formed by light elements such as carbon, nitrogen, hydrogen and so on. These light elements have smaller atomic radius and thus stronger attraction to the shell electrons. Consequently, organic materials usually exhibit lower dielectric constants, which in turn induce higher exciton binding energy (467.5-1854 meV), seen in Table 2 [29]. In contrast, inorganic (or mainly inorganic perovskite) counterparts generally have much lower exciton binding energy (5.97-8.50 meV for CIGS, 12.68 meV for a-Si:H and 2.33 meV for $CH_3NH_3PbI_3$ perovskite, shown in Table 2), where thermal vibration at room temperature (k_{BT} ~25 meV) is enough to break electron-hole pairs and release free electrons and holes. The low exciton binding energy of 3D organic-inorganic perovskite solar cell is one of its benefits compared to all-organic counterparts. The high exciton binding energy of organic requires special design to dissociate exciton into free electrons and holes.

3.2.1 Polycrystalline inorganic cells

P-n junction is used for charge dissociation for inorganic cells. In conventional *p-n* junctions, as illustrated in Fig. 14, the concentration gradient of electrons between n-doped and p-doped side drives the electrons diffuse from the "*n*-side" to the "*p*-

side" i.e., from right to left, across the interface leaving holes at the n-side border. Similarly, holes diffuse in the opposite direction and leave electrons at the p-side. As such, equilibrium finally reaches, and a "space charge region" forms to establish an electrical field across the interface [100], with the field direction pointing from the n-side to the p-side, shown as "Electric field" in Fig. 14.

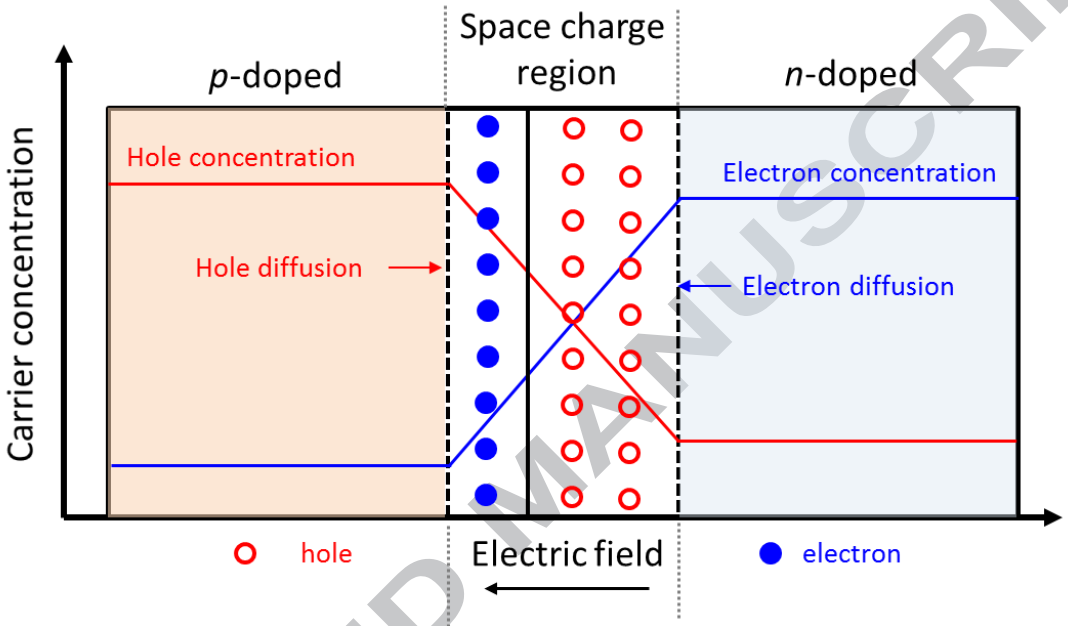

Fig. 14 A p–n junction in thermal equilibrium with zero-bias voltage applied

Upon illumination, let's say with p-type semiconductor as absorber, photoelectrons and holes are generated within the p-side. The photoelectrons generated in the p-side move within the p-side, when encounter the p-n junction, they move ("drift") across the interface into the n-side by this electric-field, while the holes at the p-side. As such, charge dissociation is realized. The transport of photoelectrons in the p-side is the limiting factor in generating the final photoelectron current as they are the minority charge carriers as compared to the holes in a p-type semiconductor. As such, in later discussion, charge transportation and recombination are all referring to that of the minority charge carriers. As the key is the effect of the electric field, this is only effective for free electrons and holes, as in the case of inorganic solar cells where the electron-hole pairs are not bond to each other. That's why the p-n junction method of charge dissociation has no use for excitons generated in organic solar cells because the excitons are electrically neutral. Copper indium gallium sulfide or CIGS solar cell is a good example of using *p-n* junction for charge

dissociation. In CIGS, Cu vacancies formed during manufacturing process serves as holes thus a natural "p-type" semiconductor. To realize a p-n junction, a thin layer (around 80 nm) of cadmium sulphide (CdS) is deposited on top of the CIGS layer to serve as the "n-side". The separation of the photoelectrons and pulling them into the CdS (while the holes are kept in CIGS and move to collecting electrode) is thus materialized. Charge dissociation with a p-n junction is highly effective. To date, the highest efficiency of CIGS solar cell achieved is 21.7% [4].

3.2.2 Amorphous silicon cells

In inorganic solar cells, such as CIGS, the mobility of electrons is much larger than that of the holes as the effective mass of the holes are much larger. Therefore, p-type semiconductor is normally used as absorber and the movement of electrons (minority charge carrier) produces the photocurrent. In hydrogenated amorphous silicon (a-Si:H) and perovskite, however, the effective masses of electron and hole are similar or comparable (as displayed in Table 2), thus they have similar mobility (termed "ambipolar semiconductor"). As such, charge dissociation in a-Si:H and perovskite needs to move both electrons and holes: electrons be collected to the "n-side" and holes to "p-side". However in amorphous silicon, the locally ordered structure is completely lost on a scale exceeding a few atomic distance and is thus a continuous random network. This randomized network dramatically retards the diffusion of charge carriers [9]. Besides, large amount of dangling bond defects in a-Si:H of (10^{15} - 10^{16}) cm^{-3} further reduced the diffusion length of charge carriers to 0.1~0.3 μm, rendering it too thin for efficient light harvesting [9]. To counter this problem, an "n" layer (heavily doped n-type a-Si:H) and a "p" layer (heavily doped p-type a-SiC:H) are built to sandwich the a-Si:H to establish an internal electric field to speed up the charge carrier transport, as shown in the schematic (Fig. 15). The sandwich structure effectively forms a p-i-n junction: the "p" is the hole-collecting layer, "i" is the intrinsic amorphous layer and the "n" is the electron-collecting layer. The resultant internal electric field profile can be adjusted through controlling of the thickness of intrinsic layer and the doping level in the "p" and/or the "n" layer. With this internal electric field, the electron is speeded up and drifts to n-side, while the hole to p-side, realizing the charge dissociation (Fig. 15(b)). The TCO layer in Fig. 15 is the transparent conducting oxide on glass substrate designed to facilitate the light harvesting by decreasing the reflection and increasing the scattering at the interface. The ZnO and the Ag or Al layer is the back contact electrode. This design structure yielded an efficiency of 13.6% [4].

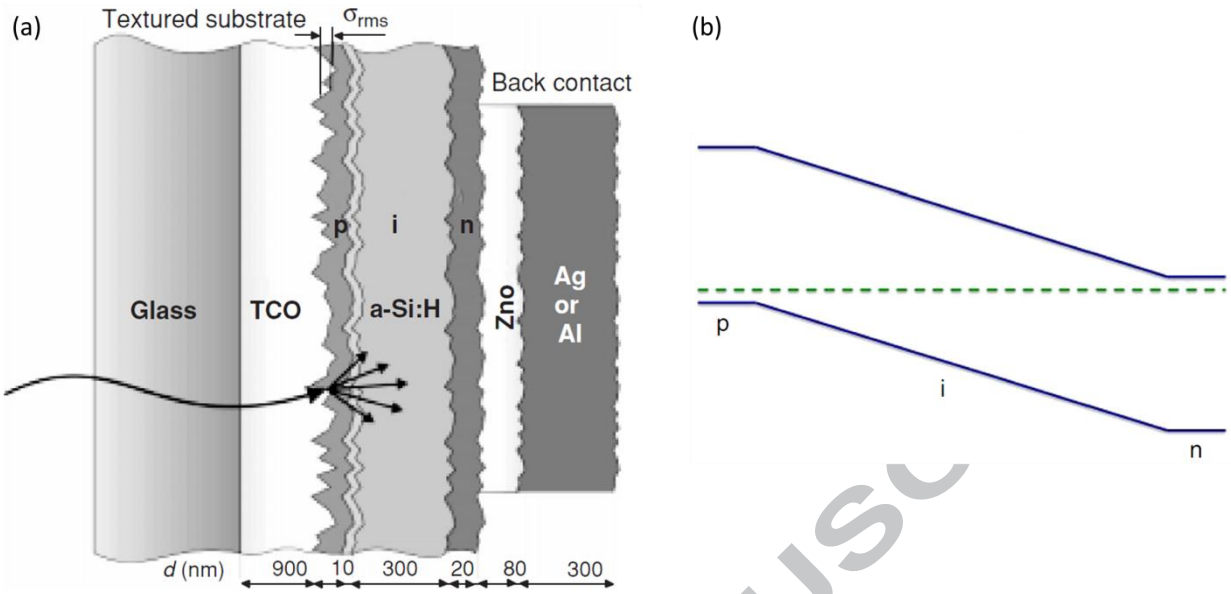

Fig. 15 (a) schematic structure and (b) band alignment of a p-i-n type a-Si:H solar cell. Reprinted with permission from ref. [9, 101]

3.2.3 Organic cells

Charge dissociation in organic solar cells is a different matter as in this case illumination creates excitons but the excitons are electrically neutral.

To split the electron and the hole bond in an exciton, two layers with one of them having higher electron affinity (so called electron acceptor) and the other one having lower ionization energies (called electron donor) are put together. Electrostatic forces generated at the interface between the two layers are designed strong enough, through materials selection, to split the excitons. Derivative of fullerene, for instance Phenyl-C61-butyric acid methyl ester (PCBM), is commonly used as electron acceptor, and polythiophene, such as poly(3-hexylthiophene) (P3HT), can be used as electron donor. Analogue to the conduction band minimum and valence band maximum in inorganic materials, in organic, the conduction of electrons takes place in the so-called "lowest unoccupied molecular orbitals" (LUMO) and movement of holes takes place in the "highest occupied molecular orbitals" (HOMO). The value of LUMO level in an acceptor is approximately equal to its negative electron affinity, while the value of HOMO level in a donor is approximately equal to its ionization potential (c.f. Fig. 16) [102, 103]. Fig. 16 illustrates two types of organic materials with different energy levels of LUMO and HOMO put together to form a so-called "heterojunction" [104]. When an exciton (illustrated in the diagram as the elliptic) diffuses to the junction, the exciton is split into electron and hole,

where the electron (the red dot) is "injected" to the polymer with a lower LUMO and the hole (the open circle) stays in the original polymer. This completes the splitting and dissociation of the exciton.

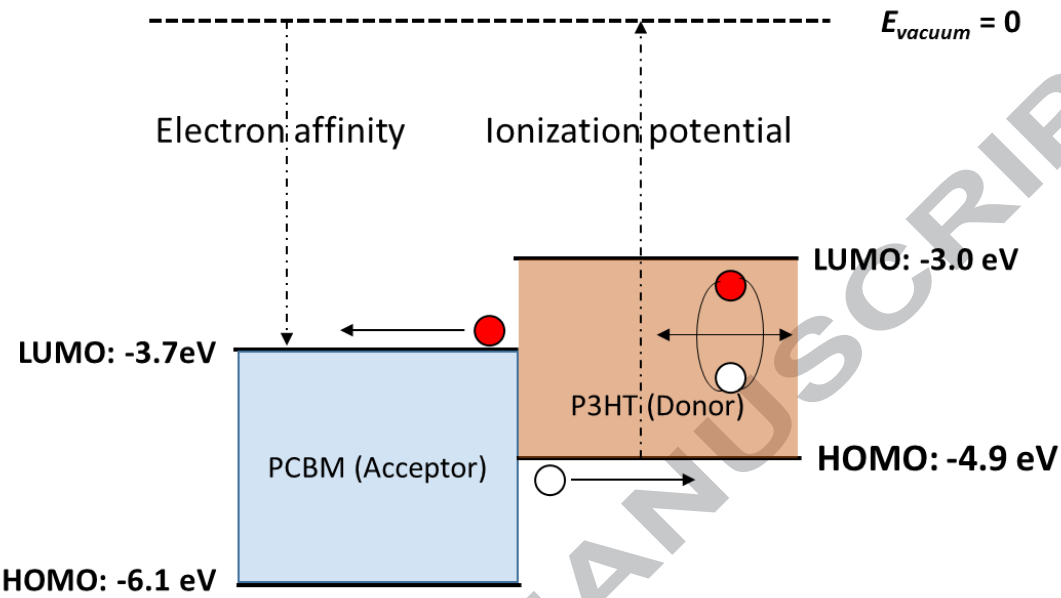

Fig. 16 Illustration of heterojunction splits excitons. Reprinted with permission from ref. [104]. P3HT is poly(3-hexylthiophene) (P3HT), while PCBM is 1-(3-methoxycarbonyl)propyl-1-phenyl[6,6]C61, energy level date are taken from reference [105]

However limited by the short diffusion length (in the scale of 10 nm) of exciton within organic material, only small amount of exciton could reach the interface therefore limits the dissociation efficiency. Bulk heterojunction is introduced and will discuss in section 4. Based on this design, Hu et al reported a high efficiency of 10.7% with terthiophene-based donor and acceptor [106].

3.2.4 Organic-inorganic hybrid perovskite cells

Perovskite solar cell exhibits similar device structure, a typical configuration of device is shown in Fig. 17. Fig. 17 (a) illustrates a mesoporous design, i.e., on a transparent conducting glass (Fluorine doped Tin Oxide or FTO), one compact layer of *n*-type thin film (such as TiO_2, SnO_2 and so on) is deposited (the dark gray layer). On top of that, a layer of mesoporous TiO_2 (the round sphere labelled TiO_2) is spin-coated. After firing/sintering, perovskite (the dark red layer) is made to fill up the space and also form a capping layer. Finally a hole transporting layer (HTM, such as spiro-OMeTAD, p-type) is spin-coated on before a metallic electrode is evaporated (the Au layer in Fig. 17 (a)).

Fig. 17(b) explains possible collection mechanism of electrons and holes at FTO and Au electrode respectively. When $MAPbI_3$ perovskite is used, the conduction band minimum (CBM) is -3.93 eV, photoelectrons excited to the conduction band would then be able to transfer to the conduction band of TiO_2 particles, and further inject into the conducting glass FTO. As the hole collection layer has a higher CBM (in the case of Spiro, -2.11eV), the electron injection is not possible. Similarly, holes move upward to spiro as depicted in the diagram, and finally reach the Au electrode.

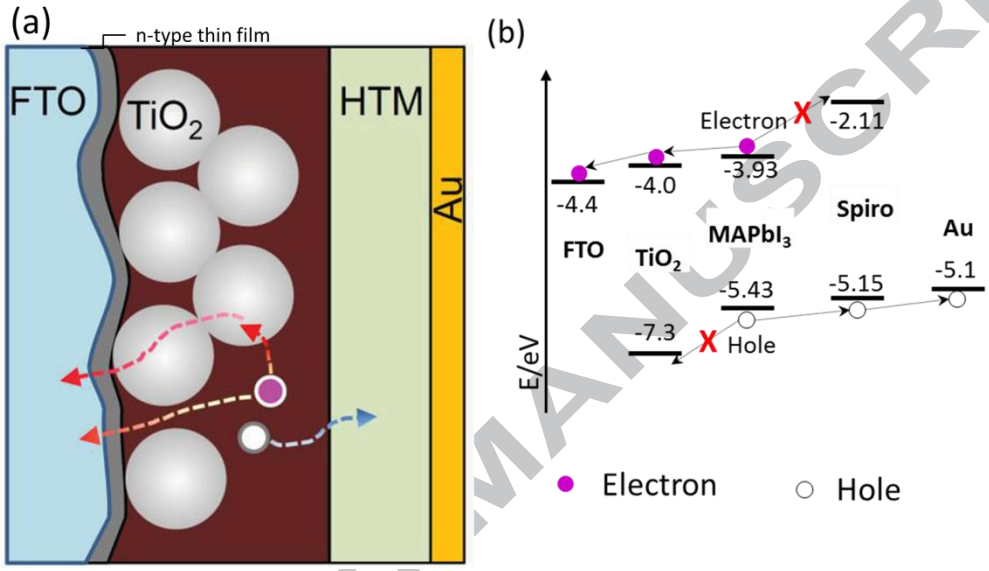

Fig. 17 Illustration of (a) mesoporous structure, and (b) band alignment of $CH_3NH_3PbI_3$ ($MAPbI_3$) perovskite solar cells, reprinted with permission from ref. [107]. The energy level data is taken from reference [108]

The compact n-type thin film layer on the FTO glass serves as the hole blocking and electron extraction layer and the p-type HTM layer serves as electron blocking and hole extraction layer. It was once believed that the existence of mesoporous TiO_2 and HTM, very thin perovskite layer on top of TiO_2 nanoparticles are essential to allow perovskite effectively inject electrons into TiO_2 and further collected by electrode, the same way as in DSSC (Fig. 18(a)). However, complete replacement of mesoporous TiO_2 with mesoporous Al_2O_3 (Fig. 18(b)), which is insulating thus electron injection is not possible, the cells still work with a comparable efficiency [109]. Increasing the thickness of the capping layer (the perovskite layer on top of mesoscopic TiO_2 layer) of nearly 500nm (Fig. 18(c)), a device with an efficiency of 20.8% was achieved [110], meaning the perovskite itself actually conduct both electron and hole efficiently to the collection electrode without recombination. As such, total elimination of the mesoporous layer results in simple planar devices (Fig. 18(d)) with an efficiency of >18% [111]. To further simplify the structure, researchers even completely excluded the usage of HTM, directly contacting the Au

electrode with perovskite (Fig. 18(e)), or with a triple-layer structure of TiO_2, ZrO_2 and carbon (carbon-device) filled with perovskite (Fig. 18(f)). However direct contact perovskite with metal without HTM increases the recombination rate at the metal side, detrimental to device performance. The highest efficiency with HTM free and Au contact is 11.2% [112]. In Fig. 18(f), the Au contact is replaced with carbon as contact electrode, and a layer of ZrO_2 was added to reduce recombination. The conduction band minimum of ZrO_2 is higher than that of TiO_2 and valance band maximum is lower than that of carbon. Therefore the photo-electron generated in perovskite can only move to TiO_2 and holes move to carbon side. This ensures elimination of the recombination [113]. The highest efficiency achieved of this carbon device is 15% [114].

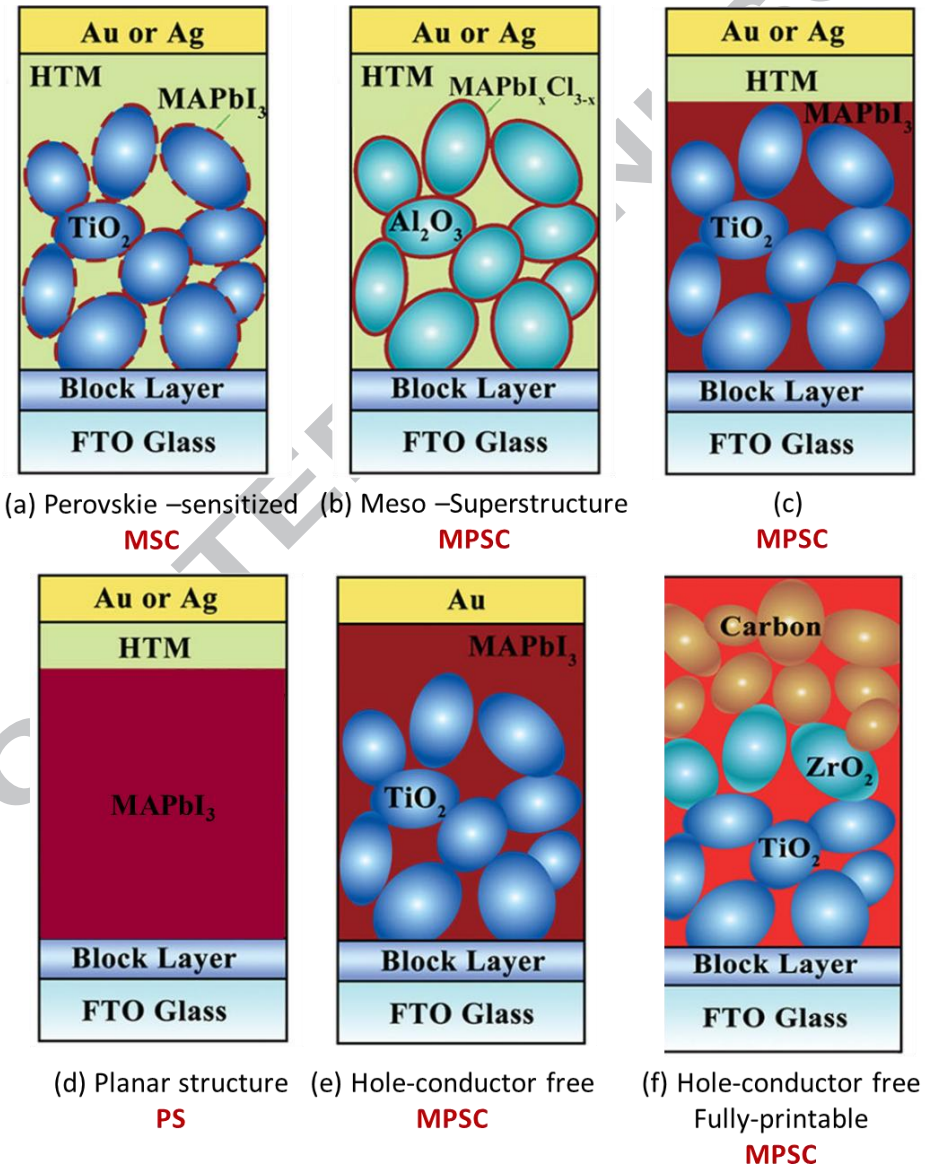

Fig. 18 Historic architecture evolution of mesoscopic perovskite solar cells, starting from perovskite-sensitized mesoscopic to planar to HTM-free fully printable MPSC. Reprinted with permission from ref. [114]

Fig. 19 illustrates how ferroelectric domains helps charge separation [115]. In polycrystalline perovskite thin film, there exist many nanoscale ferroelectric domains with opposite direction. These neighboring domains establish a local electric field where electrons move along the minima of potential while holes will move along the maxima of potential. In junction solar cells, the generated electrons and holes need to travel to the interface of junction and be separated, during these traveling, electrons and holes might encounter each other and get recombined. As the size of these ferroelectric domains is of a few nanometers (much smaller than crystal grains in bulk-heterojunction or thickness of an absorber layer in a *p*-*n* junction cell), the electron and hole can be easily separated right at the site where they are generated. This seemingly explains the experimentally observed long diffusion length and low recombination rate of charge carriers in perovskite solar cells. (As will be discussed in section 4, the ferroelectric property theory in perovskite is still controversial).

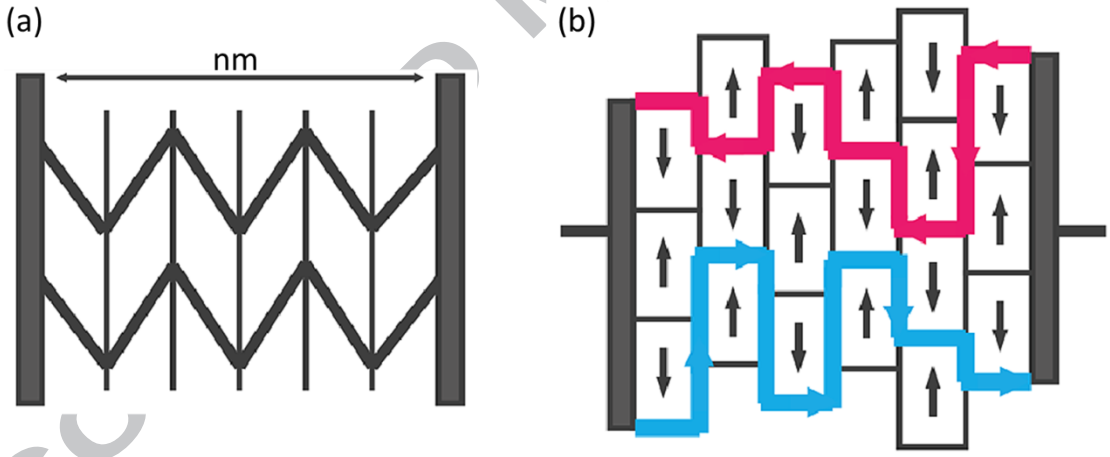

Fig. 19 A schematic illustration of (a) a multi-domain ferroelectric thin film and (b) the electrons and holes separation and transport pathway, where electrons will move along minima in the potential, while holes will move along maxima. Reprinted with permission from ref. [115]

As perovskite and a-Si solar cells share similar device configuration, researchers thought that it is the work function difference between *n*- and *p*-type contact layers that builds up an electric field across the perovskite [123]. This field enables electrons to drift to the *n*-type contact layer (i.e. electron extraction layers, such as TiO_2) and holes to the *p*-type contact layer (i.e. hole transporting materials, such as spiro). Another supporter of this built-up field is the observation of motion of ions

or charged defects [116]. Eames et al, however, proved otherwise: ion/defect motion actually weakens the built-in electric field [117].

Edri et al [101] used electron beam to bombard the $CH_3NH_3PbI_{3-x}Cl_x$-based cell cross-section (c.f., Fig. 20(a)) and measured the induced current and plotted into a 3D surface current profile (c.f., Fig. 20(b)). The profile displays a "twin-peak", similar to what a *p-i-n* junction would behave, thus is considered a *p-i-n* junction in nature. Guerrero et al [118], however, showed different results. Fig. 21 (a) set up a cross section Kelvin probe force microscopy measurement of a perovskite cell. The potential increased from the interface between TiO_2 and perovskite till more than half of the perovskite layer and then flattened into spiro layer (Fig. 21(b)). No twin-peak was observed: only one junction near TiO_2 side and no junction at spiro side. This explains electron extraction layer is essential for perovskite solar cell; while without HTM the device still can work, coincident with experimental findings.

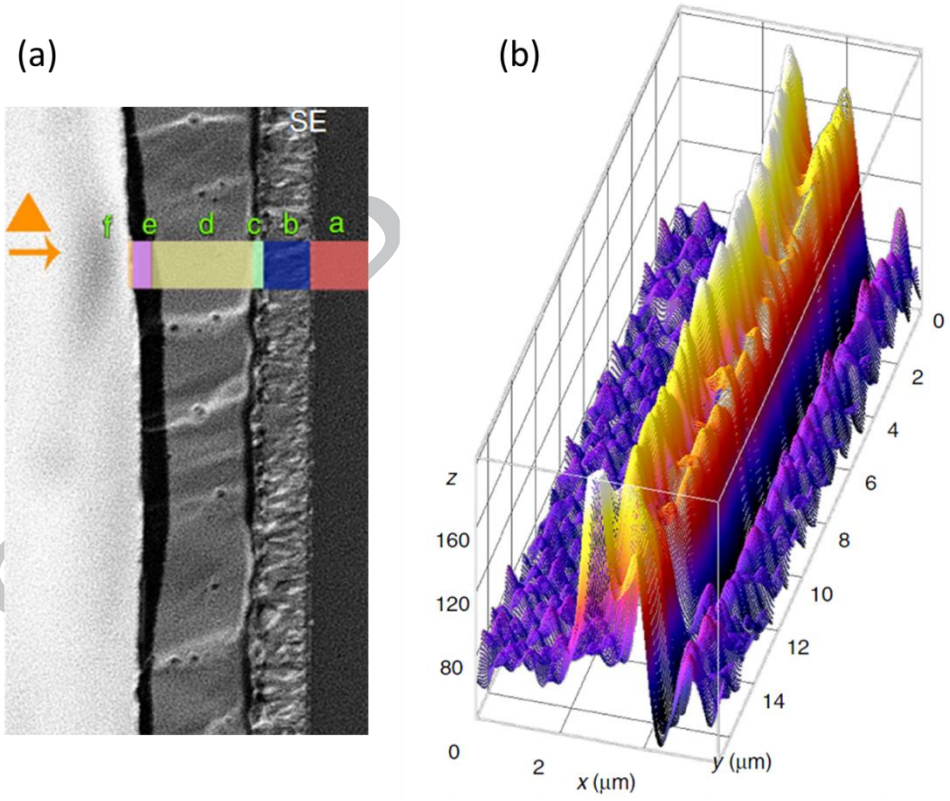

Fig. 20 (a) Cross section SEM image of perovskite solar cell, where a:glass, b:FTO; c:TiO_2, d:$CH_3NH_3PbI_{3-x}Cl_x$, e: HTM, f: Au, the arrow shows the scan direction. (b) 3D surface plot of the EBIC image. Reprinted with permission from ref. [101]

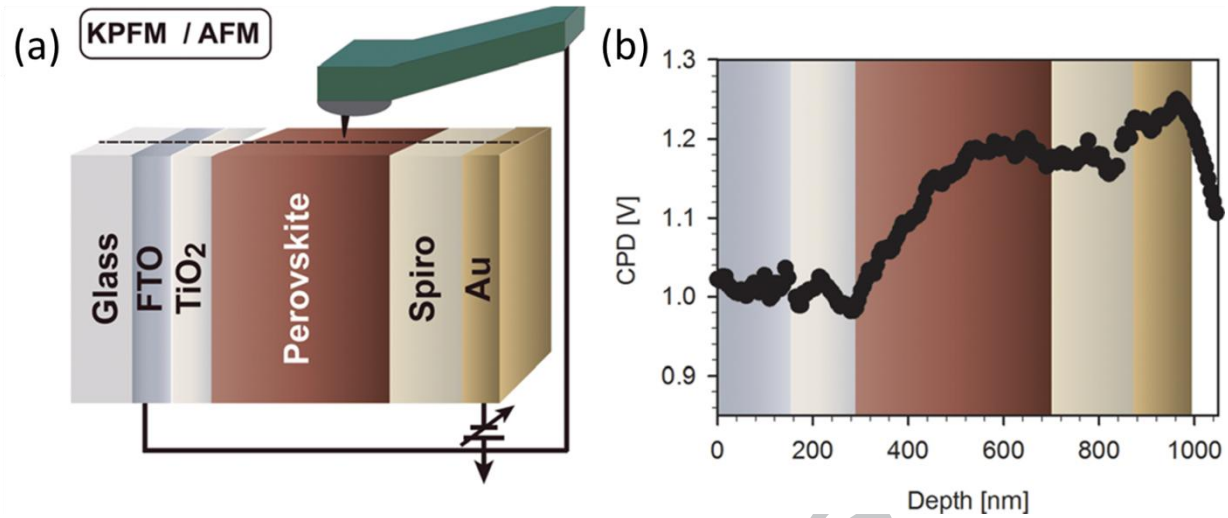

Fig. 21 (a) Set-up of the Kelvin probe force microscopy signaling the lateral path over which contact potential difference is monitored CPD, (b) average values over several tracks are displayed. Reprinted with permission from ref. [118]

However other researchers argue that there is no strong or direct proof of the existence of built-in electric field across the perovskite layer. If the field is induced by the contact layers, the maximum Voc achievable should be the value of this field, i.e. the energy level difference between the two contact materials. However, the reported Voc of perovskite solar cell is sometimes higher than the so called built-in field. For instance, SnO_2 has lower conduction band level than that of TiO_2. However the Voc obtained from SnO_2-based perovskite solar cell is higher than that from TiO_2-based cells (1.19 V vs ~1.14 V) [119]. Li-doping lowers the work function of SnO_2. However, when Li-doped SnO_2 is used as contact layer, the solar cell achieved a Voc value of 1.106 V, higher than 1.084 V without doping [120]. As such, other mechanisms should also be at work. One of these possibilities is the co-existence of electrons and holes inside perovskite, which somehow, forms two energy levels, that in turn, contributes to the charge dissociation and the attainable Voc. To establish a different contact condition, Gouda et al [121] coated MgO on top of TiO_2 nanoparticle inside the perovskite solar cell. The variation of Voc is investigated with different light intensity (Fig. 22). At low intensity, the increasing of Voc is determinant of the contact (TiO_2 or MgO). However, at high intensity, the contact material does not affect the Voc anymore. This is an indirect proof that the Voc is determined not only by contact materials but also perovskite itself.

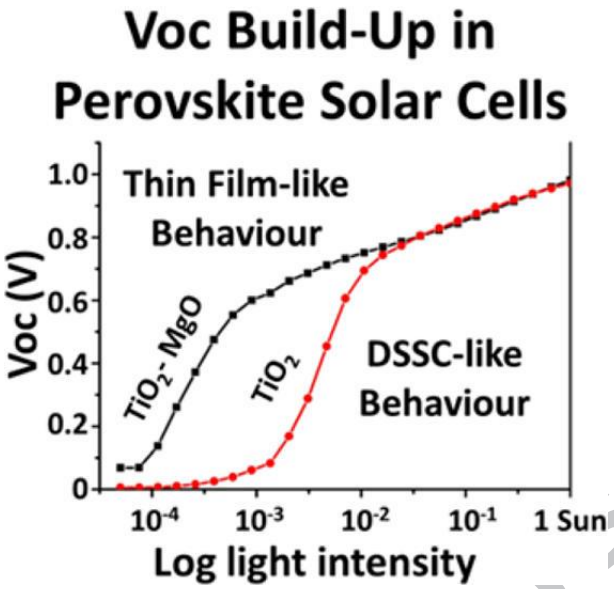

Fig. 22 Illustration of Voc build-up in perovskite solar cell [121]

In fact, grain boundary also serves charge separation in perovskite (as is also reported in CIGS [122]). As shown in the surface Kelvin probe force microscopy investigation, the potential at grain boundary (blue color area in Fig. 23(a)) dramatically increased compared to that in the inner grains (pink color area in Fig. 23(a)). This potential difference serves to separate the charges. And the grain boundary serves as the charge transportation channel into the collection electrode (Fig. 23(b) and (c)) [123]. As grain boundaries are plane defect affected by many factors during fabrication, it is not surprised this measurement result varies in reports.

Charge separation in perovskite solar cell is still not clear and all mechanisms are debatable. This, therefore, is still one of the most active research areas in perovskite thin film solar cells.

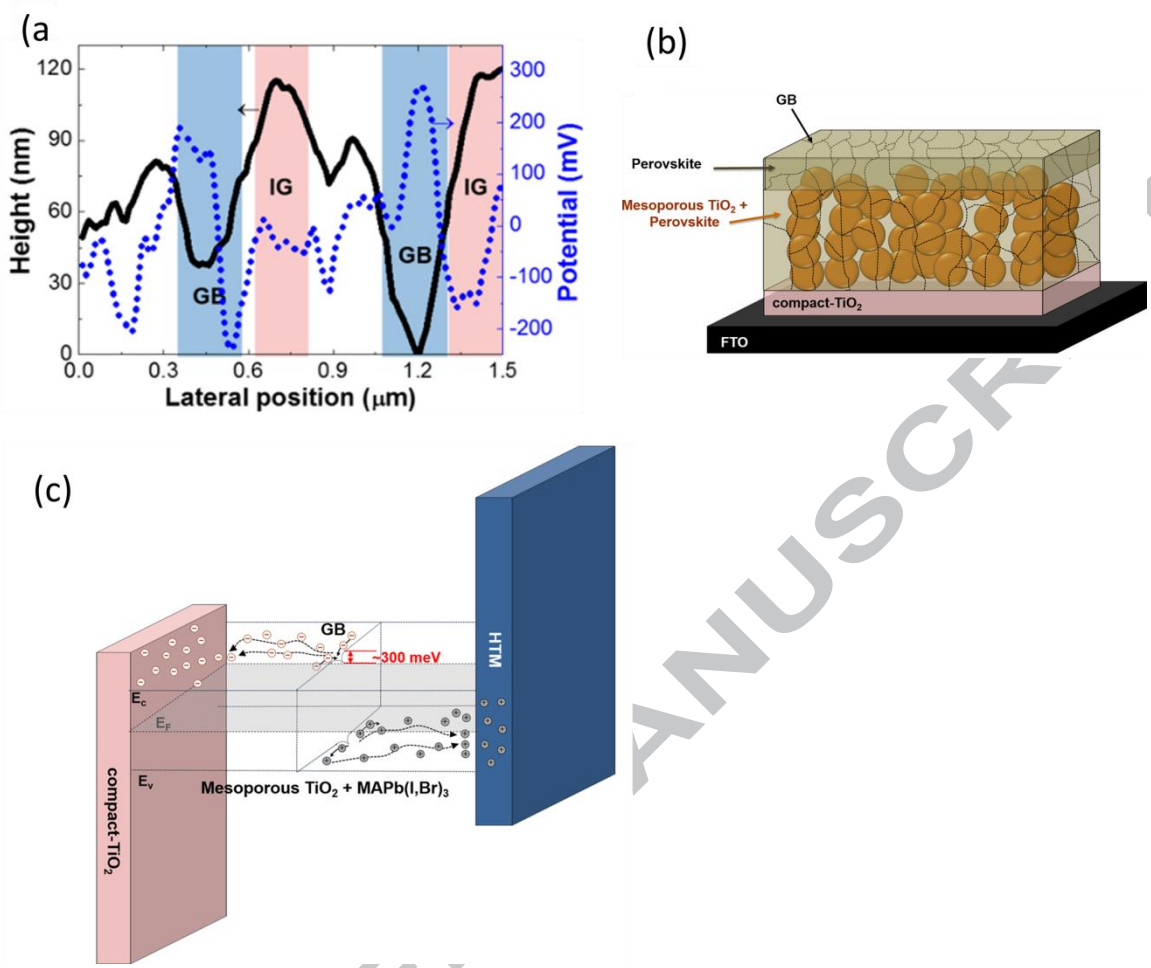

Fig. 23 (a) one-dimensional potential and the topography line profiles near the GBs in the perovskite thin films, (b) structure of the mesoporous TiO_2 with a mixed halide perovskite absorber (c) the schematic band diagram near the GBs in Br-contained $MAPb(I_{0.88},Br_{0.12})_3$ thin films. The electron–hole carrier separates the mesoporous TiO_2 layer from the perovskite layer. The charged GBs (potential value at GBs ~300 mV) have a high local built-in potential, which improves the carrier separation. The electrons attract the TiO_2 layer, and the holes move to the HTM layer. Reprinted with permission from ref. [123]

3.3. Efficiency of charge transportation and collection

Once the charges are dissociated, they diffuse or drift to the respective electrodes and thereby power the external loads. Two processes are involved, i.e. charge transport within the semiconductor and the collection by the electrodes. Efficiency of both the processes affects the total efficiency of the solar cell device.

The net-movement speed of a charge carrier is characterized by the term “mobility”. The distance which a charge carrier travels before recombination takes place is

referred to as "diffusion length". Mobility defines speed and the diffusion length measures the maximum travel distance. These are the two most important key items affecting solar cell efficiency that guide the design of the cells. For instance, the thickness of light absorption layer should be made thinner than the diffusion length.

The collection efficiency is mostly depending on the interface between semiconductor and the collection layer. The properties of collection layer, such as conductivity, band edge etc, will also influence the charge collection efficiency. The device structure can be specially designed to facilitate charge carrier transport and collection process. In this section, factors affecting charge transport and collection will be discussed.

3.3.1 Factors affecting charge transport

Normally diffusion is driven by concentration gradient and drift is induced by electric field. Einstein equation relates these two, as follows [124]:

$$D = \mu \frac{k_B T}{q} \tag{4}$$

Where D is the diffusion coefficient, μ is the mobility, k_B is the Boltzmann constant, T is the absolute temperature, and q is the electric charge that a particle carries. The charge carrier mobility is defined as: [124]

$$\mu = \frac{q \cdot \tau_s}{m^*} \tag{5}$$

$$m^* = \frac{\hbar^2}{k_{ex}} \cdot \frac{1}{\partial^2 E_n / \partial k^2} \tag{6}$$

where τ_s is the mean scattering time and m^* is the effective mass, $\hbar$ is the reduced Planck constant, k is the wave vector, E_n is the energy level, k_{ex} is wave vector at the band edges.

Therefore, the charge carrier mobility is determined by two factors: effective mass m^* and mean scattering time τ_s. The larger the effective mass, the lower the mobility, and the longer the scattering time, the higher the mobility. The effective mass, related to the second derivative of the energy band, is, in turn, affected by the composition and band structure of the materials. The charge carriers can be scattered by crystal defects and impurities (here ignore the phonon scattering), hence affecting the scattering time. Grain boundary is one of the important scattering centers which decrease the mobility. This is the reason why single crystal

normally shows high charge carrier mobility compared to polycrystalline films. Therefore, the main factors affecting mobility is composition and band structure defined effective mass, grain boundary and other defect induced scattering.

When charge carriers transport (diffuse or drift) in a material, there are two possible ways by which they get recombined. The charge is captured by a defect or gets trapped thus become immobile, and later when another charge of the opposite polarity comes by, they get recombined. This defect is referred to as "recombination center". Poor morphology with pin-hole or other imperfections, grain boundaries are all recombination centers. The recombination also takes place when charges of opposite polarity meet each other. Therefore, concentration of majority carriers increases the opportunity of recombination of the minority charge carriers, thus must be controlled at a proper level.

Let τ be the lifetime of the minority charge carrier, the effective diffusion length L is then related to τ through [125-127] :

$$L = \sqrt{D\tau} \tag{7}$$

Inserting equation (4) and (5) into (7) gives rise to

$$L = \sqrt{D\tau} = \sqrt{\mu\tau\frac{kT}{q}} = \sqrt{\frac{q\tau_s}{m^*}\tau\frac{kT}{q}} = \sqrt{\frac{\tau_s\tau}{m^*}kT} \tag{8}$$

Thus the L is determined by carrier life time τ, scattering time τ_s, and effective mass m^*. From Eq. (6), effective mass m* is related to energy levels, which, in turn, are determined by composition and structure of a material, therefore, effective mass can be tailored through composition and structure design.

Both carrier lifetime and mean scattering time are negatively affected by the imperfections in the material, such as poor morphologies, grain boundaries, vacancies, interstitials, etc., processing control of the material production is vital in achieving a good efficiency. For instance, a wrong morphology of the same material may prove detrimental to the whole cell. Details of these influencing factors and possible solutions are discussed below.

Influence of composition and band structure on effective mass

According to Eq. (6), the effective mass m* is inversely proportional to the second derivative of band energy with respect to wave factor, i.e. m* is directly proportional to the curvature of the energy distribution curve at the extrema. Fig. 24 illustrates

band structure of $CuIn_{0.75}Ga_{0.25}Se_2$ in different space directions calculated using density functional theory [33]. As the energy of valence band maximum is set to zero, negative energies refer to energies in valance band and positive ones to conduction band. In Fig. 24, the conduction band of $CuIn_{0.75}Ga_{0.25}Se_2$ is more dispersed with smaller effective mass of electron of 0.086 m_0 and the energy distribution reflecting valance band (i.e., below zero) is much more flatter than those in the conduction band, giving rise to an effective mass of hole of $0.67m_0$, drastically larger than 0.086 for electrons .

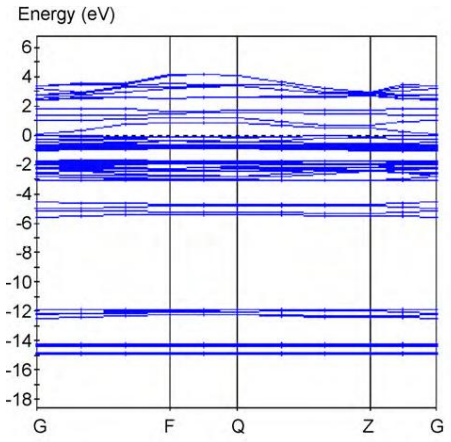

Fig. 24 Band structure of $CuIn_{0.75}Ga_{0.25}Se_2$ structure calculated by density functional theory. Reprinted with permission from ref. [33]

The influence of element on the effective mass comes in through the interaction between the electron clouds that exerts alternation to the energy distribution. When this interaction results in more possible electron states or the electrons are more delocalized, the effective mass reduces. In $CuInS_2$, the valance band is formed by the interaction between Cu *d*- and S *p*-orbit electrons, while the conduction band is developed by the overlap of In *s*- and S *sp*-orbits, the effective mass of electrons and holes are 0.16 m_0 and 0.39 m_0 (c.f., Table 2). Compared to Se atoms, the *s* and *p* states are much more localized in S atoms due to the smaller atomic radius and thus stronger attraction [36], therefore, replacing S with Se to form $CuInSe_2$ "delocalizes" the electrons (and holes), which, drastically reduces the effective mass of electrons to 0.08 m_0 (a 50% reduction!) and that of the holes to 0.14 m_0 (a 64% reduction!!).

Depending on formation of the conduction band and valance band structures, the effective mass change may go opposite ways. In methylammonium lead iodide ($CH_3NH_3PbI_3$) perovskite, hybridization between Pb-6*s* and I-5*p* states forms its valance band and the conduction band is derived from Pb 6p states [45, 128-130]. As Tin (Sn) has smaller atomic size, Sn 5s has higher energy than Pb 6s state,

substituting Pb with Sn results in Sn 5s mixing with I 5p orbit to form stronger anti-bonding than that of Pb atom in valance band [43]. Therefore the valance band of Sn-based perovskite is more dispersed thus effective mass of the hole reduces to 0.13 m_0 in $CH_3NH_3SnI_3$ from 0.25 m_o in $CH_3NH_3PbI_3$, (c.f., Table 2) about 50% reduction. Meanwhile, as the Pb 6p electron is more delocalized than Sn 5p, the effective mass of electron increases from 0.19 m_o in $CH_3NH_3PbI_3$ to 0.28 m_o in $CH_3NH_3SnI_3$ [43].

Effectively, substituting atoms with different sizes affects the band structure and therefore the effective mass of charge carriers. A lower effective mass contributes to higher charge carrier mobility, while the narrow bandgap favors more photons to be harvested. High efficiency can be achieved by optimizing these factors.

Influence of imperfections on diffusion length and mobility

Surface integrity, grain boundaries, defect concentration and device design all affect the charge transportation and thus efficiency of the solar cells.

The quality of the light absorbing layer (continuity of coverage and free of pin-holes) is crucial in eliminating the current leakage points and recombination centers in the effort to achieve high efficiency.

Fig. 25(a) shows a dendritic crystal with poor coverage of $CH_3NH_3PbI_3$ perovskite (from the so-called "one-step" manufacturing method) while Fig. 25(b) is a uniform cube-like crystals with good coverage of the same material (from the so-called "two-step" manufacturing method) [131]. The poor coverage results in direct contact between hole blocking TiO_2 layer and the hole conducting material, as illustrated in Fig. 25(c) fabricated with one-step compared to Fig. 25(d) with two-step method, causing recombination, thus dramatically decreased the electron life time of about one order of magnitude difference as seen in Fig. 25(e).

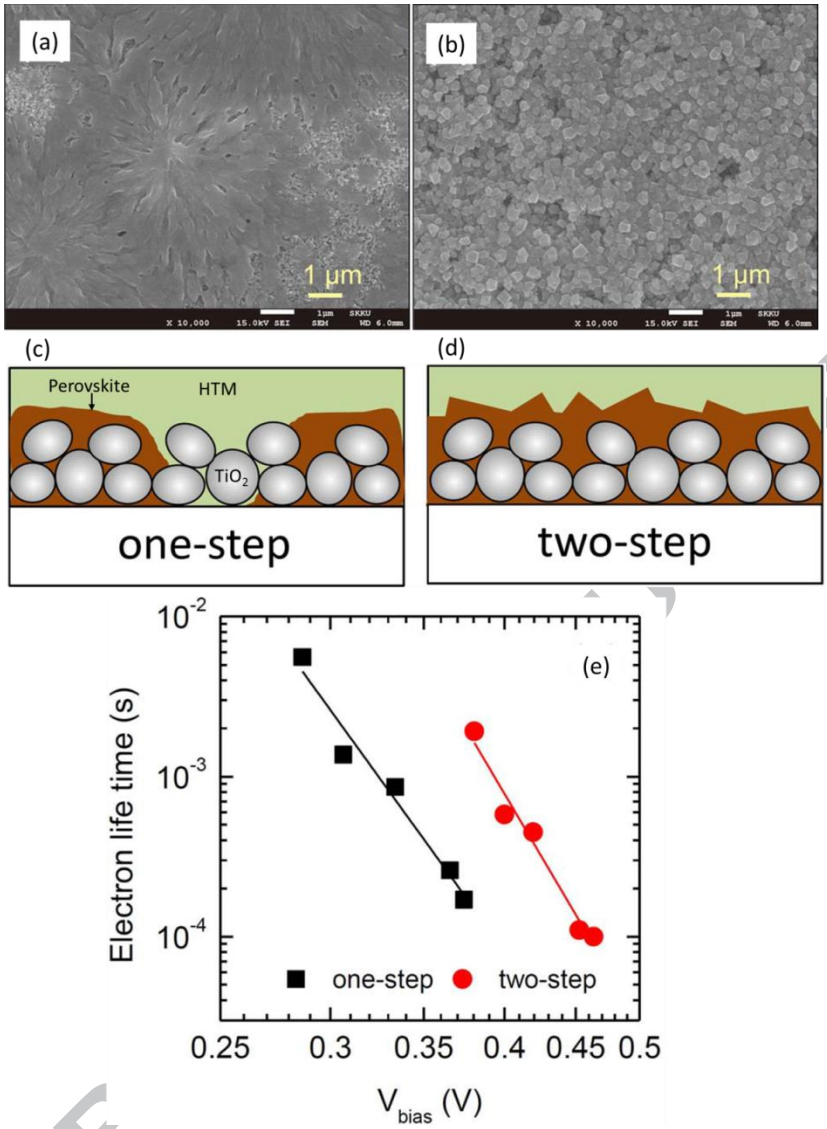

Fig. 25 surface morphology of $CH_3NH_3PbI_3$ ($MAPbI_3$) films fabricated by (a) one-step and (b) two-step method, schematic illustration of charge selective layer contact of perovskite from (c) one-step and (d) two-step method, (e) the measured electron life time at different bias [131]

One way of making $CH_3NH_3PbI_3$ ($MAPbI_3$) perovskite layer is to dissolve PbI_2 and MAI in N, N-Dimethylformamide (DMF) at the same time. After spin coating onto the substrate, it is heated at a hot plate at around 100 °C for evaporation of residual DMF and final crystallization thus achieves the absorption layer at one go (thus "one-step"). Because of the difference of PbI_2 and MAI in dissolvability, wettability and ionic strength [131], nucleation and growth of PbI_2 and MAI is largely different resulting in non-uniform and abnormal crystal growth during evaporation of DMF.

To combat this non-uniformity, fast evaporation and fast crystallization hold the key. Fig. 26 studies process in achieving fast evaporation. In Fig. 26(a), DMF is

evaporated slowly; In Fig. 26(b), diethyl ether is dropped onto the substrate during spin-coating. As diethyl ether is a high volatile solvent and also miscible with DMF promoting fast evaporation of DMF, giving rise to better surface in Fig. 26(b) as compared to dendrite morphology in Fig. 26(a) [133]. Huang et al [132] simply used compressed Argon gas to blow away excess solvent to promote fast evaporation and achieved uniform perovskite film with dense packed crystals.

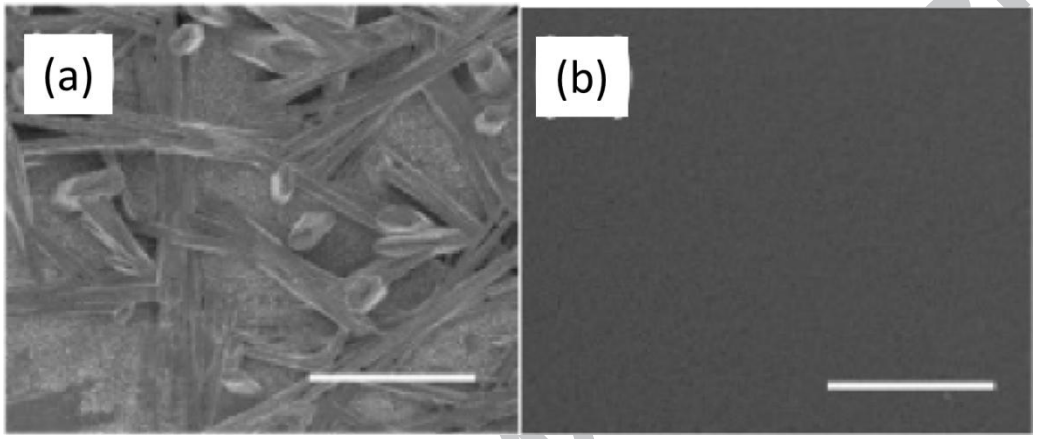

Fig. 26 Surface SEM images of (a) without and (b) with diethyl ether wash during spin coating. Reprinted with permission from ref. [133]

Faster crystallization can be realized with different source of lead-containing precursors. Lead iodide (PbI_2) as precursor for perovskite needs 100 °C for 20 min for crystallization. Lead acetate ($PbAc_2$), however, requires only 2.5 min at 100 °C [134] for good uniformity (Fig. 27(c) as compared with PbI_2 (Fig. 27(a)) and $PbCl_2$ (in Fig. 27(b)). The activation energy of crystallization (E_a) for these three lead sources were obtained from in-situ X-ray data, i.e., $E_a(PbI_2)$ =97.3 kJ/mol, $E_a(PbCl_2)$= 86.6 kJ/mol, $E_a(PbAc_2)$=67.5 kJ/mol, in the order such that $E_a(PbI_2) > E_a(PbCl_2) > E_a(PbAc_2)$ [135]. However, it is not necessarily the lower the crystallization activation energy the better the surface morphology. Lead nitrate [136], for instance, has an activation energy of 56.6 kJ/mol [135], resulting in crystallization during the spin-coating process, but gives rise to a surface far from desire (c.f., dendrite grains in Fig. 27(d)).

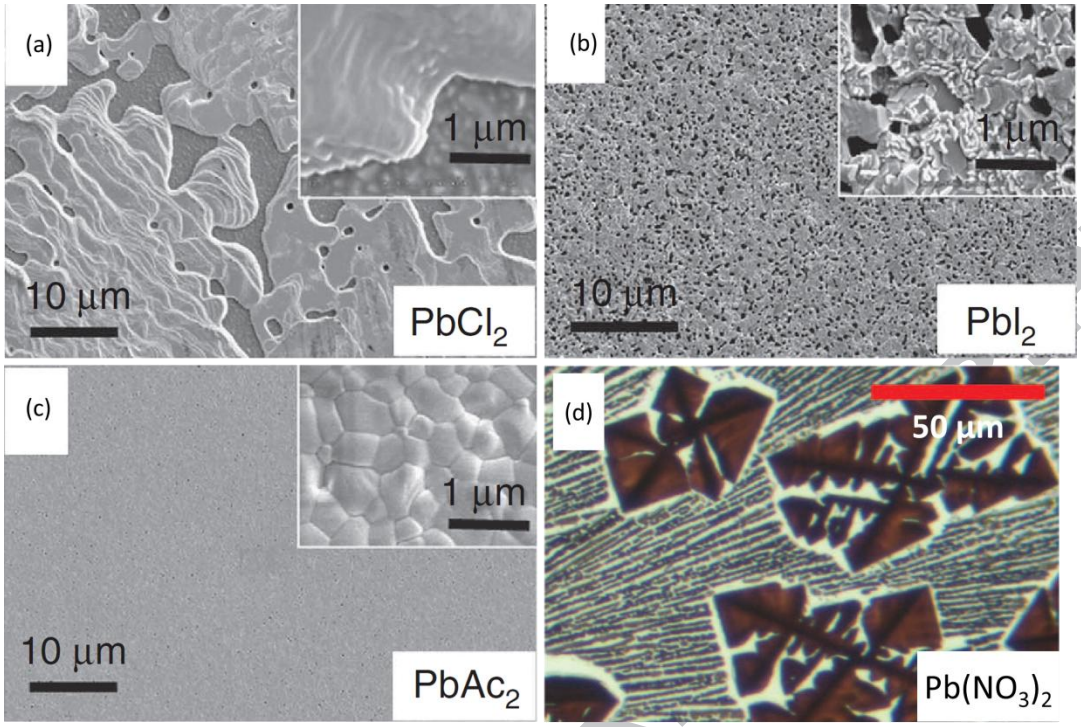

Fig. 27 Surface morphology of perovskite fabricated from different lead source of (a) PbI_2 processed at 150°C, (b) $PbCl_2$ processed at 100°C, (c) $PbAc_2$ processed at 100°C and (d) $Pb(NO_3)_2$ processed at 45°C. Reprinted with permission from ref. [134, 136]

Grain boundary (GB) plays an important role in the charge transport of solar cells. GB can be either beneficial or detrimental to device performance. Under normal circumstance, impurities tend to accumulate and more defects are found at the GBs compared to that inside the grains, thus larger grain means less GBs thus lower concentration of defects. On the other hand, GB could be electrically charged if the impurities or defects accumulated there are electrically charged. In this case, GB induces a built-in electric field that helps the charge separation [137-139] as discussed in section 3. Such a GB is said to be "benign" [140, 141]. Benign GBs in perovskite were confirmed both by calculation [140] and experiment [141]. GBs aligned perpendicular to the substrate separate grains into vertical alignment and at the same time behave "benign" thus are beneficial to device performance [142].

Bigger grains can be achieved through rising of the annealing temperature or increasing annealing time or both, but only to a certain extent, i.e., less than 300 nm [143]. As both PbI_2 and MAI are easily dissolved in DMF, annealing in the presence DMF vapor proves effective in increasing the grain size [144]. Fig. 28 shows the resulting microstructure of the grains with and without the presence of DMF vapor. The grain size of perovskite through traditional annealing (TA) was less than 300

nm while under solvent annealed (SA), the grain size reached over 1μm (Fig. 28(b) and (c)). The charge recombination lifetime was induced from transient photovoltage technique and gives in Fig. 28(d). With DMF vapor (i.e., the SA process), the charge recombination lifetime is 7.2 μs, more than three times longer than that without (the TA process, 1.7 μs). This gives rise to 2.3 times increase in Hall mobility and diffusion length increase from 282 to 886 nm. Similar results are obtained through moisture [145] and excess MAI [146]assisted annealing.

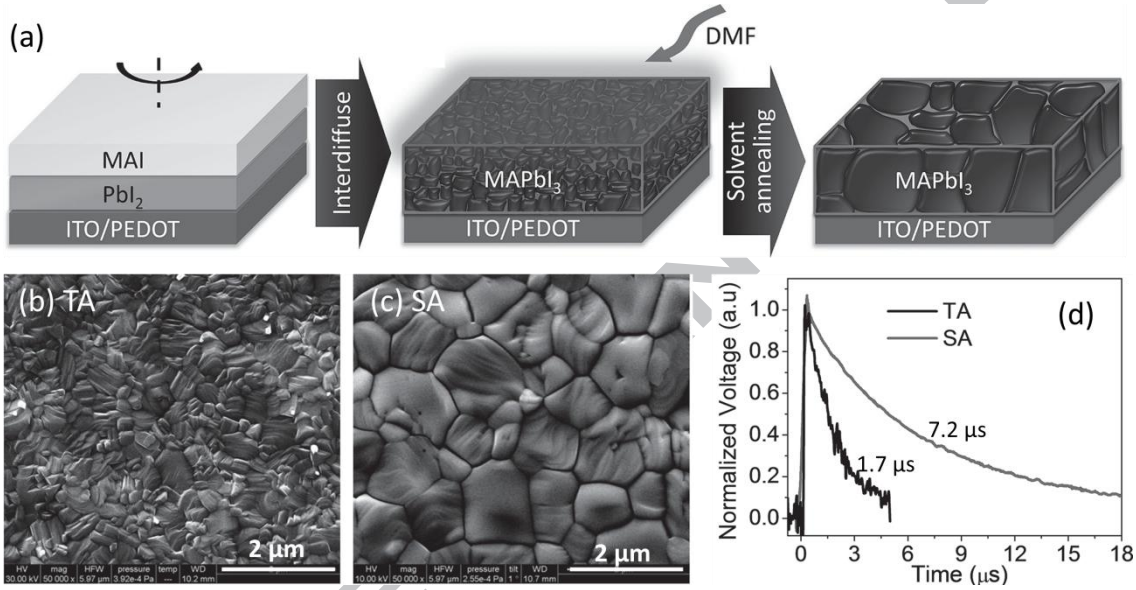

Fig. 28 (a) Schematics of the approach and solvent-annealing-induced grain size increase, surface morphology of (b) traditional annealing (TA) and (c) solvent annealing (SA) of 1015nm-thick perovskite, (d) Photovoltage decay under 0.3 Sun illumination measured by transient photovoltage technique. Reprinted with permission from ref. [144]

Combining nucleation and growth into one process, Nie et al [147] spin-coats preheated substrate with hot solution, as illustrated in Fig. 29. The maximum grain size achieved reaches millimeter scale (Fig. 29(c)). In essence, this process clearly makes use of the above "SA" effect, in addition to nucleation and growth at one-go, resulting in extremely large grains and dramatically improved efficiency and mobility (c.f., Fig. 29(d)).

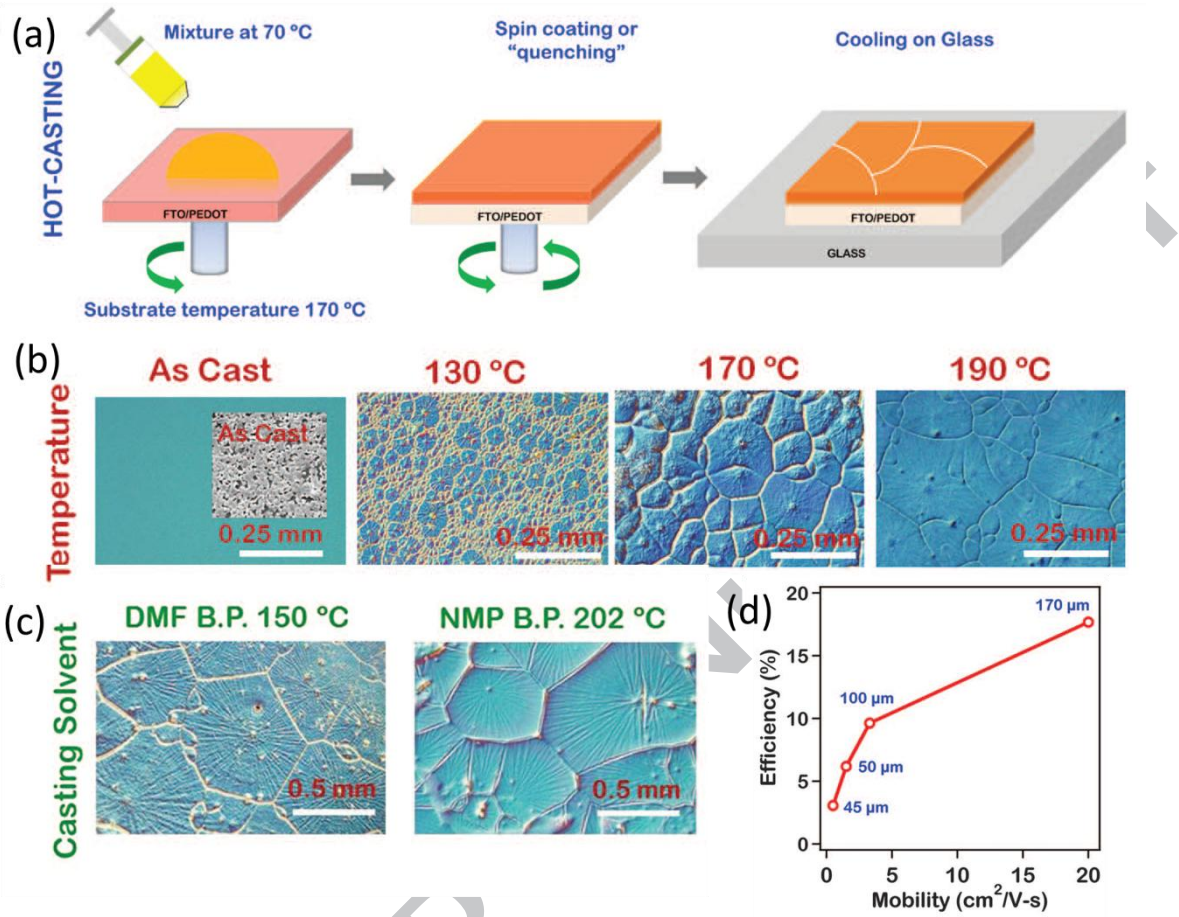

Fig. 29 (a) schematic of hot-casting process for perovskite films, (b) and (c) the large grain size observed for ($PbCH_3NH_3I_{3-x}Cl_x$)–based thin film, and (d) the effect of grain size on the efficiency of solar cell device [147]

Defects (such as vacancy, interstitial and antisite) and their concentration define not only the intrinsic type of semiconductor (*p* or *n*-type) but also the concentration of majority charge carriers' further influence the diffusion length. The non-radiative recombination centers with energy level deep in the band are mainly responsible for the short lifetime for minority carriers, resulting in low open circuit voltage.

In lead based perovskite, the calculated energy levels of point defects are given in Fig. 30 [140]. Intrinsic point defects, such as iodine interstitials (I_i), CH_3NH_3(MA) molecules on Pb sites (MA_{Pb}), CH_3NH_3 vacancies (V_{MA}), Pb vacancies (V_{Pb}), MA interstitials (MA_i), antisite defect (Pb_{MA}), and Iodine vacancy (V_I), have low formation energy, which showed very shallow transition energy levels (means near the band edge). While defects with deeper energy level, such as I_{MA}, I_{Pb}, Pb_I and Pb_i, have high formation energy and are not the dominant defects in perovskite

materials [140, 148]. Therefore, the defects in lead based perovskite materials are mainly shallow defects, which have less effect on the recombination and charge transport.

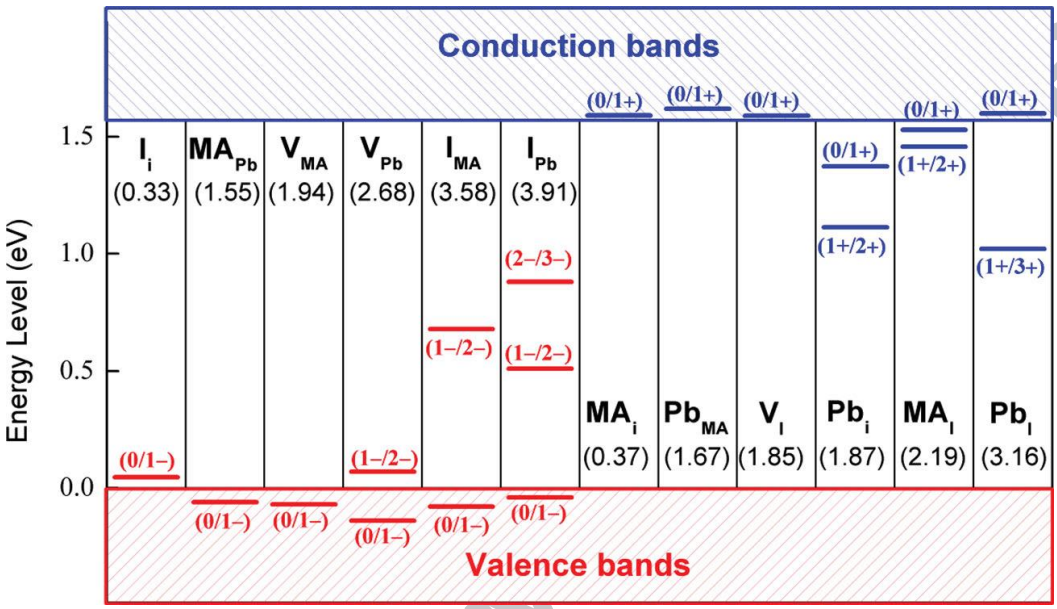

Fig. 30 Calculated transition energy levels of point defects in $CH_3NH_3PbI_3$. The formation energies of neutral defects are shown in parentheses. Reprinted with permission from ref. [140]

On the other hand, although iodine interstitials (I_i) is found in α-$CH_3NH_3PbI_3$, it could freeze in the lattice and remain to be the dominant defects in β-$CH_3NH_3PbI_3$ during the phase transition from α to β-phase at around 60 °C [148]. By alloying iodine with chloride, the formation of interstitial I_i is suppressed due to the shrinkage of lattice therefore reduces the density of trap states and increases the diffusion length [45]. Snaith's group [149] reported that the diffusion length of electron and hole for $CH_3NH_3PbI_3$ is 129±41 nm and 105±32 nm respectively, while that for $CH_3NH_3PbI_{3-x}Cl_x$ is 1069±204 nm and 1213±243 nm respectively, demonstrating an improvement of an order of magnitude.

During formation of an alloy, atoms of similar size may occupy "wrong site", such as Zn occupying some of Cu position in CZTSSe. This kind of defect is termed "antisite" defect. The way to reduce antisite defect is to partly use atoms of not-so-similar size. From the Period Table of Elements (see Table 1), as Zn, Cd, and Hg are in the same group with increasing atomic size, Cd or Hg can be used to replace Zn. Similarly Ag in the same group as Cu, it can be made use to replace Cu. Su and co-workers [150]

used Cd to replace part of Zn, improved their CZTS efficiency from 5.3% up to 9.24%. Similar improvements were reported using smaller atomic size Ge to substitute Sn [151, 152]. However there is no report on Ag and other transition metal replacement of Cu and/or Zn and should be conducted later.

As mentioned afore, transportation of minority charge carriers affects the efficiency of solar cell, therefore it is obvious that the majority charge carrier concentration should be controlled in a proper level (< 10^{15} cm^{-3} for lead based perovskite) [153], too high a majority carrier concentration increases the possibility of recombination between minority and majority carriers thus shorten the life time and diffusion length. This becomes more serious in Tin (Sn) based perovskite solar cell (such as $CsSnI_3$, $CH_3NH_3SnI_3$ etc), as the formation energy of Sn vacancy generating hole is very low leading to a hole concentration as high as 10^{17}~10^{18} cm^{-3}, much higher than that in lead based perovskite [154]. This high hole or majority charge carrier concentration results in a short diffusion length of 30 nm in $CH_3NH_3SnI_3$ as compared to around 1 μm in lead based $CH_3NH_3PbI_3$ perovskite. Calculation shows that with the decreasing of hole doping concentration from 10^{18} cm^{-3} to 10^{15} cm^{-3}, the diffusion length of $CH_3NH_3SnI_3$ dramatically increases from around 50 nm to >1 μm [155]. Based on this, Kumar et al introduced extra tin fluoride (SnF_2) to retard the formation of tin vacancy, achieving an efficiency improvement from 3×10^{-4}% to 2.02% with 20% addition of SnF_2 into $CsSnI_3$ [156].

Influence of device design on charge transportation

As charge transport involves “charge drift” and “charge diffusion”. Charge drift occurs as charge moves under the effect of an electrical field and charge diffusion is the movement of charge under charge concentration gradient. All that accelerate these aspects improves charge transportation.

In the context of solar cells, the electric field refers to the built-in field due to the difference in energy levels of the components in the material. The strength of the electric field is obviously affected by the composition.

Careful adjustment of composition gives rise to band grading therefore favorites the movement of charge carriers. Fig. 31 [157] shows this strategy in CIGS solar cell, in which the p-n junction is formed between the *p*-type CIGS absorber layer and the *n*-type CdS and ZnO layers. Molybdenum is the back contact electrode, molybdenum selenide ($MoSe_2$) formed during the growth of the CIGS absorber resulting in a favorite quasi-ohmic contact. In Fig. 31(a), secondary ion mass spectrometry (SIMS) results of the composition profile along CIGS thickness direction are plotted for

three samples, A, B and C, of which Sample C has a relatively wider and flatter of low gallium content range (green color line with wider and flatter valley) compared to Sample A and B. As discussed afore, addition of Ga into CIS primarily increases the conduction band minimum (E_C in Fig 31(b) and (c)), whereas the valence band maximum (E_V in Fig. 31) is only slightly affected, thus increases the bangap of CIGS. Too low and profound Ga ratios existing in Sample A and B result in lower E_c near the *p*-*n* junction and form a "notch" in the conduction band edge E_c, acting as a drain that traps electrons and lead to enhanced recombination with holes from the valance band E_v (c.f. Fig. 31(b)). On the contrary, higher concentration and more smooth distribution of Ga in Sample C results in an optimal bandgap grading profile favoring the electron drift without any barrier (c.f. Fig. 31(c)). With this design, the efficiency of CIGS solar cell improves to 18.7% for Sample C, from 16% for Sample A and 17.6% for Sample B.

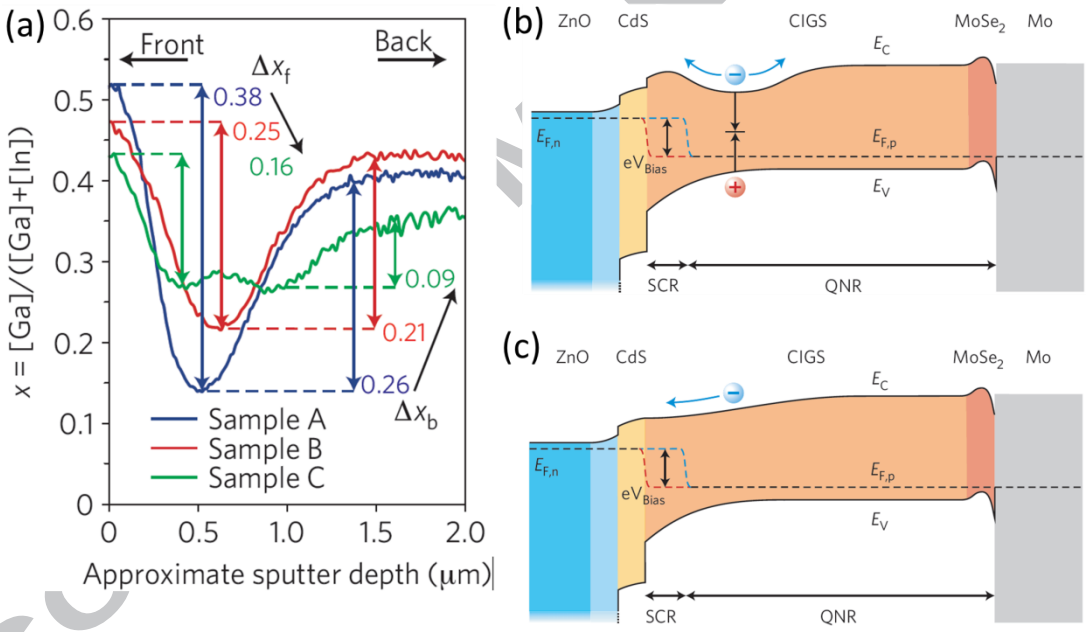

Fig. 31 Illustration of (a) Depth profiles of the three samples (A–C) showing the relative Ga content *x* along the CIGS film depth as assessed by SIMS measurements. Indicated are the front grading heights Δx_f and back grading heights Δx_b, the electronic barrier (b) without and (c) with optimized grading condition, indicated are conduction band energy E_C, valence band energy E_V, Fermi level E_F, space charge region (SCR), and quasi-neutral region (QNR). Reprinted with permission from ref. [157]

In organic solar cells, the diffusion length is usually short, around 10 nm, [158-163] which is too thin for effective absorption to take place (typically at least 100 nm

thick absorption layer is needed). The way to overcome the short diffusion length problem is to use bulk heterojunction, i.e., organic acceptor and donor molecules or polymers are mixed to form a blend of heterojunctions with fine grains [164-166]. Fig. 32 illustrates this concept where the different colors represent two types of organics having different energy levels. The "heterojunctions" formed at the interfaces between these two organic grains are 3D distributed within the films, thus termed as bulk heterojunction (BHJ). In this case, interpenetration is important in order to channel the charge out from the material. Without annealing, the BHJ has fine microstructure and lots of junctions but may not interpenetrated thus charges are isolated within and cannot be channeled out as shown in Fig. 32(a) [167]. Annealing is applied to increase the grain size and form interpenetrating network of donor/acceptor favoring the charge transport. The electrons and holes are transported separately in the network of acceptor and donor [168]. However too much annealing increases the grain size, coarse the morphology even finally results in phase separation. Fig. 32(c) shows the coarse morphology produced by too long time annealing; the average domain size (W_c) is much larger than the diffusion length of exciton (L_{ex}) inducing less efficient charge dissociation. An optimized condition (i.e. grain size equal to exciton diffusion length) of annealing exists for every pair of donor and acceptor, shown in Fig 32 (b) as t_a (opt) [167].

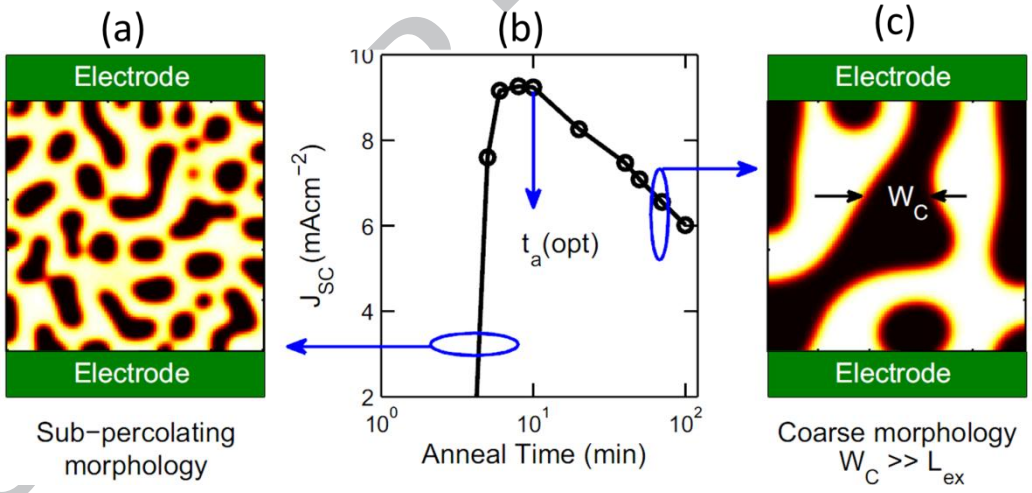

Fig. 32 Annealing effect on the short-current density of BHJ. Reprinted with permission from ref. [167]

3.3.2 Factors affecting charge collection

As the electrons and holes are transported into the interface of collection layer, they are collected to load the outer circuit. The collection should be fast enough to eliminate the charge accumulation and possibility of recombination at the interface.

The band edge matching (band alignment) between semiconductor and the collection layer, the properties especially conductivity, and the geometry of the collection layer will affect the collection efficiency.

In planar perovskite configuration, the TiO_2 (especially deposited by spray pyrolysis and spin coating process) is normally used as the electron extraction. However, the band edge of TiO_2 layer fabricated by atom layer deposition (ALD) is higher than perovskite [119]. Lots of electrons accumulate at the interface due to this energy barrier and get recombined, giving rise to low collection efficiency. Hagfeldt and coworkers [119] completely replaced TiO_2 with SnO_2 processed by ALD, to align the band with perovskite, especially that of the mixed perovskite, allowing electrons easily injection into the conduction band of SiO_2. This design results in an efficiency of over 18% for SnO_2-based devices.

To improve the stability of perovskite solar cell, inorganic TiO_2 and nickel oxide (NiO) were introduced as the electron and hole collection layer respectively, instead of organics. However, the poor conductivity of these inorganic oxides limits the charge collection and therefor the conversation efficiency. Niobium (Nb) was chosen as dopant for TiO_2, magnesium (Mg) and lithium (Li) were used to dope NiO to improve the conductivity to result in more than 15% efficiency [169].

The collection efficiency can be further improved by design 1D electrode, which performs as a charge collection highway. Examples in this category include TiO_2 nanotube arrays in DSSC [170], and interlacing of two types 1D polymers [171-173].

4. Reliability and stability in perovskite cells

Although perovskite solar cells can be produced with high performance via low cost solution process, the inherent poor stability and reliability may be fatal in its wide application. In this section we focus on issues pertaining to the reliability of perovskite solar cell performance, and environmental stability, such as thermal, moisture, light, oxygen and device configuration etc.

4.1 Hysteresis in I-V curve

One interesting phenomenon for perovskite solar cell is the hysteresis in current-voltage curve. Fig. 33 demonstrates that the device performance is strongly dependent of the measurement method, such as scan direction (forward or reverse), and scan rate. This hysteresis or performance difference is one of the data reliability

problems. Reverse or fast scan normally gives better performance than that from forward or slow scan. In cases, this difference could be notably big (c.f. Fig. 33). The cause of the hysteresis and how to get rid of it is still in hot debate. Currently three mechanisms dominate the discussions with regard to generation of the hysteresis: 1. ferroelectric, 2. ion motion, and 3. interface contact, as detailed below.

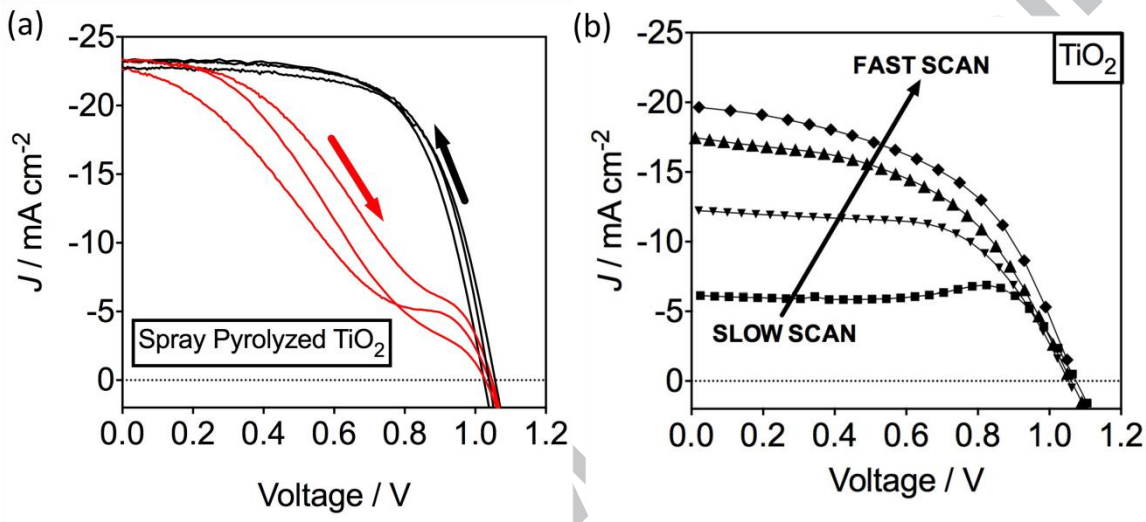

Fig. 33 (a) scan direction and (b) scan rate effect on the performance of planar perovskite solar cell on spray pyrolyzed TiO_2 and atomic layer deposited TiO_2 blocking layer [119]

Ferroelectric

Since the hysteresis I-V curve is similar in shape with ferroelectric behavior of a material (and indeed, many oxide perovskite do display ferroelectric properties), researchers naturally relate the hysteresis phenomenon to the ferroelectric properties of perovskite. The fact that dwelling of ~10 s in stepwise scan eliminates the hysteresis supports this theory: in ferroelectric model, dipoles need time to rotate and follow the external field (c.f. Fig. 34(a)) [174]. Researchers have even measured the polarization of perovskite by piezoelectric force microscopy. As shown in Fig. 34(b), domains are observed switchable similar as in a ferroelectric [175, 176]. Furthermore, when the perovskite is polarized with electric field, the current obtained follows the polarization direction and reverses the direction when the polarity is reversed, as shown in Fig. 34 (c)[177].

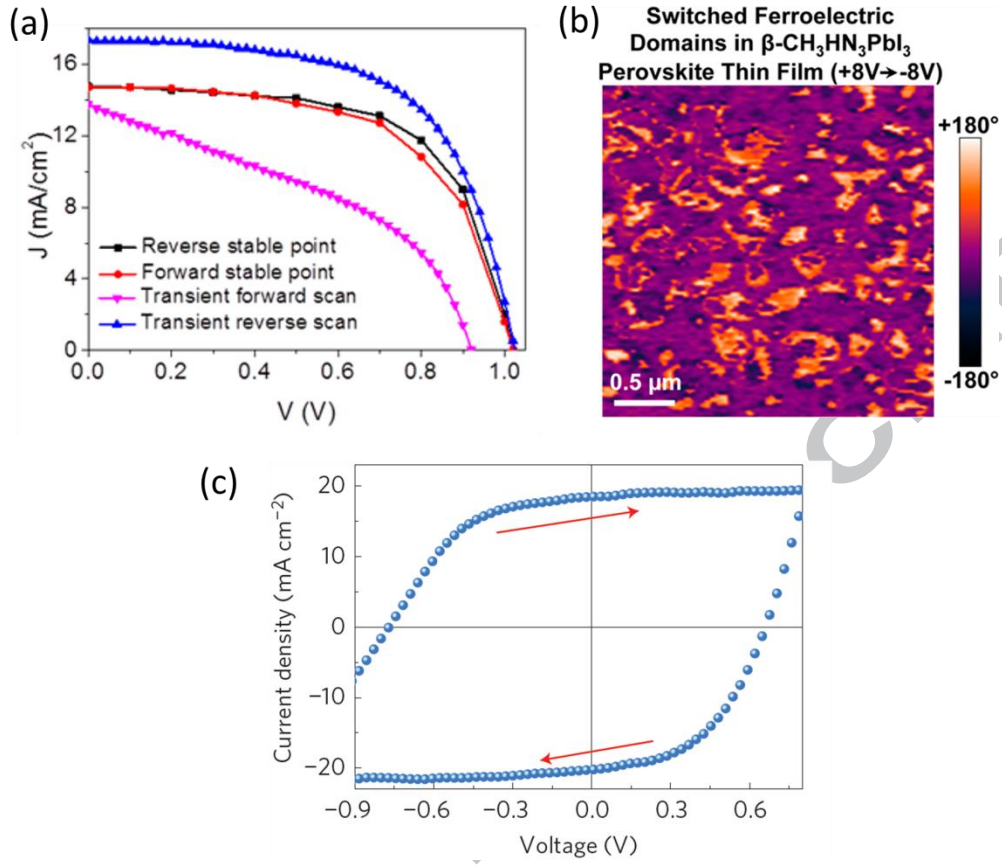

Fig. 34 (a) Current–voltage measurements of the stepwise scan measurements (with a dwell time of ~10 s per 100 mV step) and transient scan (scan velocity: 250 mV/s) in forward and reverse scans, reprinted with permission from ref. [174], (b) piezoelectric force microscopy image of switchable domain, reprinted with permission from ref. [176] and (c) switchable current-voltage curve of the perovskite devices under continuous current sweeping at a rate of 0.14Vs^{-1} between -2.5V and +2.5V after positive and negative poling. The arrows in the figures show the scanning direction, reprinted with permission from ref. [177]

Careful comparison, however, of the shapes of reported polarization-electric field loop of perovskite with true ferroelectric materials casts doubts in the ferroelectric theory. Fig. 35(a) is the expected polarization-electric field loops of a ferroelectric material. Fig. 35(b) is a typical polarization electric field loop of perovskite. Obviously they are vastly different. In one report, the hysteresis loop indeed shares similar shape with ferroelectric (Fig. 35(c)), but the polarization value has far exceeded the normal range: in excess of 1000 μC·cm^{-2} at frequencies below 0.4Hz (1/f=2.5s, c.f. Fig. 35(d)) [178], one order of magnitude higher than the best ferroelectric materials ($BiFeO_3$ thin film of 150 μC·cm^{-2}) [179].

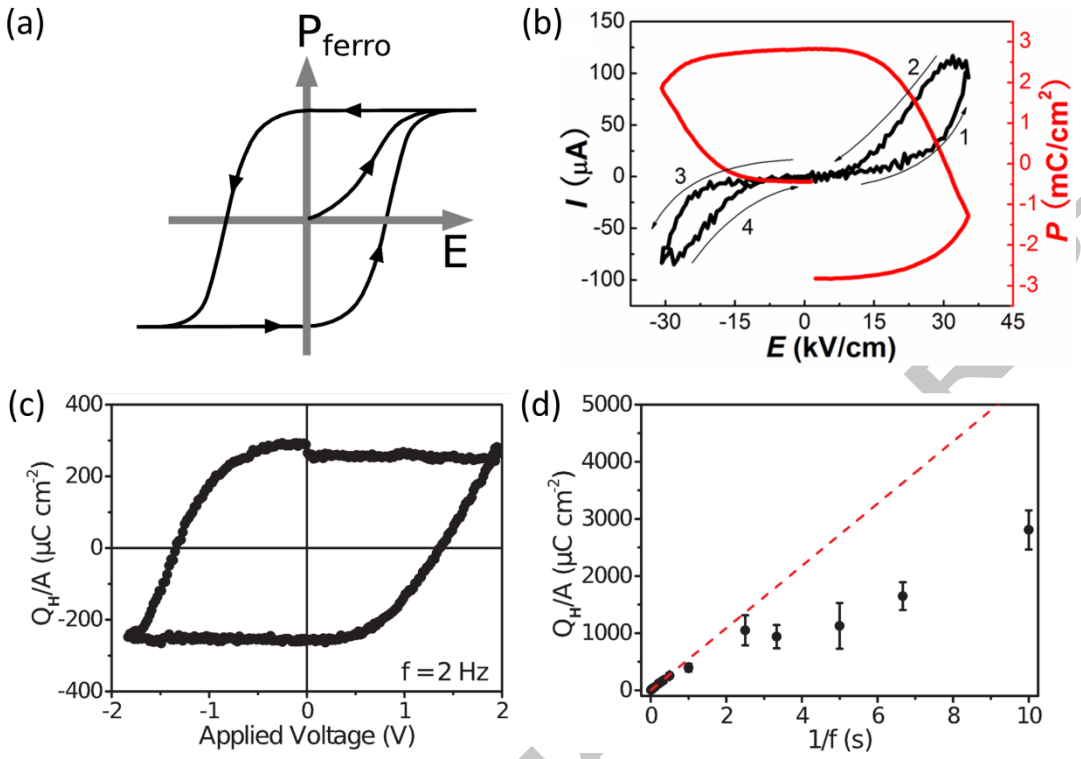

Fig. 35 (a) Expected electric (*E*)-field dependence of accumulated charges due to ferroelectric polarization; reprinted with permission from ref. [178] (b) typical experimental current-voltage (*I-E*) and polarization-voltage loop of Au/$CH_3NH_3PbI_3$/PEDOT:PSS/ITO measured with an applied voltage of 1 V and 10 Hz, reprinted with permission from ref. [180]; (c) Hysteretic charge density (QH/A) as measured by the DWM on a $CH_3NH_3PbI_3$ thin film at 2 Hz and (d) Frequency dependence of the QV hysteresis at low frequencies, where some saturation from the low frequency linear behaviour (dotted line) is observed. For f below 1 Hz, error bars indicate the range of measured values of hysteresis at each frequency, reprinted with permission from ref. [178]

Ion Motion

A typical ion conduction behavior under scanning voltage is represented by the so-called banana loop (Fig. 36(a)) [181]. The dielectric of banana skin is shown in Fig. 36(b) [182]. At the highest frequency (higher values at X-axis), the dielectric constant of banana skin is way below 100 (vertical axis). With decreasing frequency, the dielectric constant dramatically increased, reaching a colossal value of more than 10^8. This is well known banana ionic conductivity. Fig. 36(c) and (d) [183, 184] illustrate the experimental set-up and the giant dielectric constant of perovskite materials as a function of frequency. At high frequency, the dielectric constant of perovskite is less than 10, and reaches ~1000 at low frequency in dark condition. Under illumination, the dielectric constant at low frequency further increases to 10^5-10^6, which is claimed due to increased population of electronic carriers. The

striking resemblance of Fig. 36(b) and Fig. 36(d) naturally points to the ion conduction possibility.

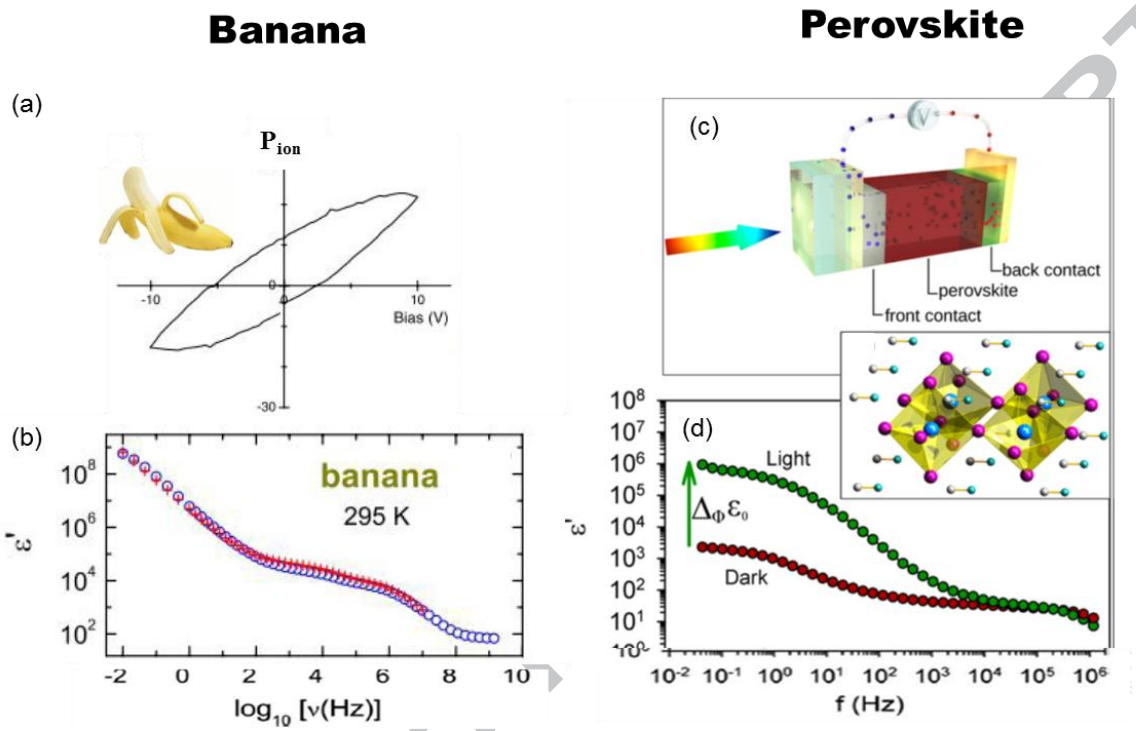

Fig. 36 Comparison of the frequency-dependent dielectric response of a banana and $CH_3NH_3PbI_3$. (a) polarization-electric field loop, reprinted with permission from ref. [181] and (b) broadband spectra of real dielectric permittivity of a banana skin at room temperature, reprinted with permission from ref. [182]; (c) illustration of dielectric property measurement and (d) real dielectric permittivity of a $CH_3NH_3PbI_3$ thin film under dark and 1 sun illumination conditions, reprinted with permission from ref. [183, 184]

In fact, fast oxygen ion motion property in oxide perovskite (ABO_3) has been applied as electrode materials for fuel cell application [185, 186]. In halide perovskite (ABX_3), ionic conductivity and motion of F^- vacancies in $KCaF_3$ was also reported [187]. Motion of Br and Cl ions was also confirmed in all inorganic ($CsPbX_3$, $KMnCl_3$) halide perovskites [188]. Ion diffusion in organic-inorganic halide ($CH_3NH_3PbX_3$) perovskite was calculated through First-Principles method. The results indicated that I^- anions in perovskites can easily diffuse with a low energy barrier of around 0.3 eV, comparable with ion conducting materials. The bond between Pb-I showed weak enough for I^- migration. Interesting enough, the A-site large organic cation, $CH_3NH_3^+$, also has a rather low barrier of <0.60 eV [189]. The calculated activation barrier of migration of Pb vacancy is around 0.8 eV [190]. As such, migration of

organic cations in perovskite is possible under an electric field. Diffusion of iodine vacancies and interstitials across the perovskite crystal is even easier as the activation energy is only ~0.1 eV [190]. The diffusion is also fast: at a short time scale of < 1 μs it could migrate to the electrodes. Comparatively, the larger organic ion $CH_3NH_3^+$ and Pb vacancies with relatively higher activation energies of ~0.5 and 0.8 eV, respectively, move at a much slower paste: in the order of tens of milli-seconds to minutes. This could be the cause of the hysteresis. In Fig. 37(a), an experiment was set up to monitor, with an optical microscope, the transmission of light through the perovskite film under applied voltage. The area closer to the anode became increasingly transparent with time (c.f., Fig. 37(b)), indicating loss of mass, an indirect proof of ion motion. Morphologically, large amount of pinholes were observed in this area (a direct proof of moving away of mass) [177]. Very recently, photo-induced halide redistribution in organic–inorganic perovskite film was observed through a unique combination of confocal photoluminescence (PL) microscopy and chemical imaging to correlate the local changes in perovskite thin film, a strong evidence of ion motion [191]. The property changes of perovskite under high pressure suggest that the relatively not compact perovskite cage may provide space for fast ion motion [192].

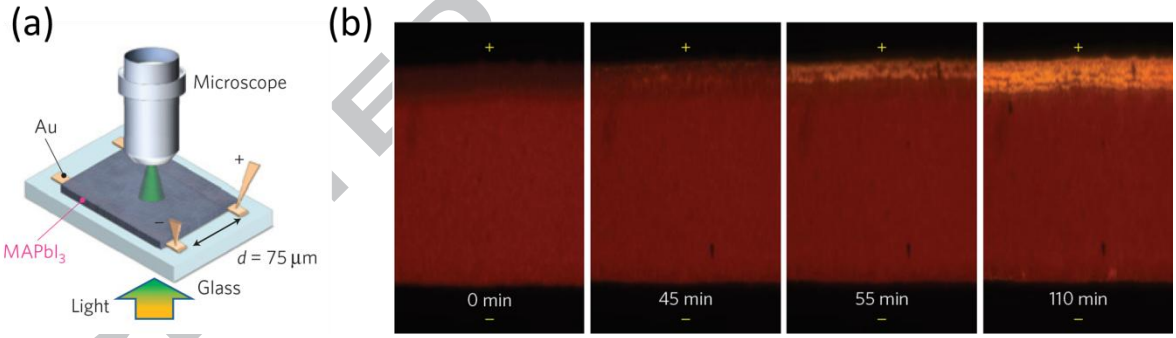

Fig. 37 In situ monitoring of the material change during the poling process. (a), Illustration of the set-up used for in situ monitoring of the poling process using a lateral structure device. (b), Snapshots of the in situ recorded video, showing changed perovskite material close to the anode side during the poling process. The electrical field applied on the perovskite film was ~1.2V·μm^{-1}. Reprinted with permission from ref. [177]

Interface contact

As not all perovskite devices have the hysteresis problem, ion motion may still not be the only mechanism. Ion motion causes migration of mass and also charge

accumulation that in turn may change the defect physics and electrical conductivity thus eventually degrades the long term stability.

Figure 38 shows no hysteresis inverted planar perovskite solar cell with PCBM(C60) as electron and PEDOT:PSS as hole transport layer [193]. The device has no hysteresis under different scan direction and scan rate from 0.1 to 0.5 V/s. In contrast, hysteresis almost always appears in perovskite solar cell with TiO_2 as contact layer. To compare, planar perovskite solar cells with different contact layers, including TiO_2, spiro, PEDOT:PSS, PCBM, NiO etc, have been fabricated and their hysteresis behavior showed that, with TiO_2 and spiro as contact layers, the hysteresis is serious while it is less with PEDOT:PSS and PCBM contact (c.f. Fig. 39) [194]. The conductivity of PEDOT:PSS and PCBM are comparable (0.014 and 0.016 $mS \cdot cm^{-1}$ respectively). The electron and hole extraction from perovskite might be similar and thus no charge accumulates at the interface. However the conductivity of TiO_2 is 0.00006 $mS \cdot cm^{-1}$, resulting slow electron extraction from perovskite compared to hole extraction [111]. The TiO_2 layer is then considered the main reason for its hysteresis behavior.

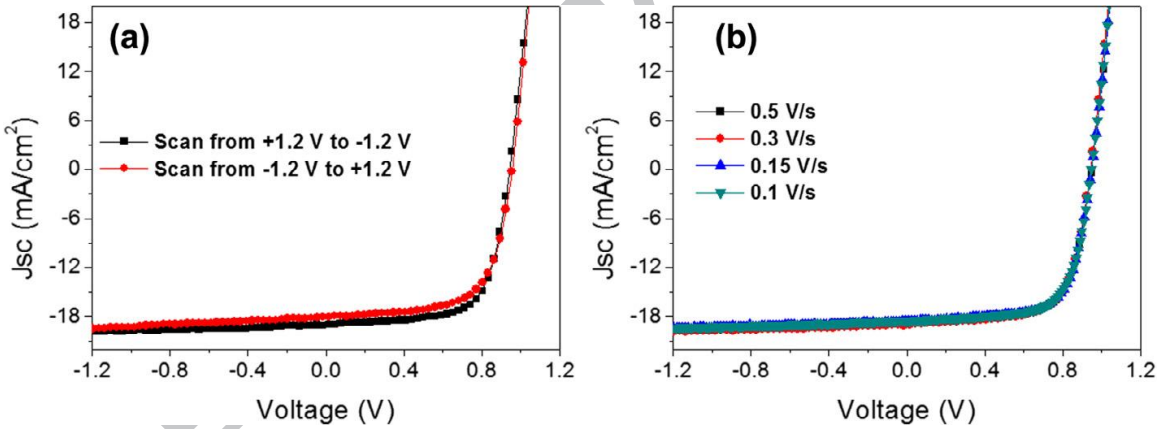

Fig. 38 J–V curves of perovskite solar cells with a structure of ITO/PEDOT:PSS/290 nm $CH_3NH_3PbI_3$/30 nm PCBM/Al measured with (a) forward and reverse scanning directions and (b) different scanning speed under AM 1.5 G illumination. Reprinted with permission from ref. [193]

To confirm this effect, hysteresis is measured in a special setup where a perovskite layer is sandwiched between two layers of FTO/TiO_2 (Fig. 40). The curves showed apparently enlarged hysteresis, confirming the problematic TiO_2 contact layer [195].

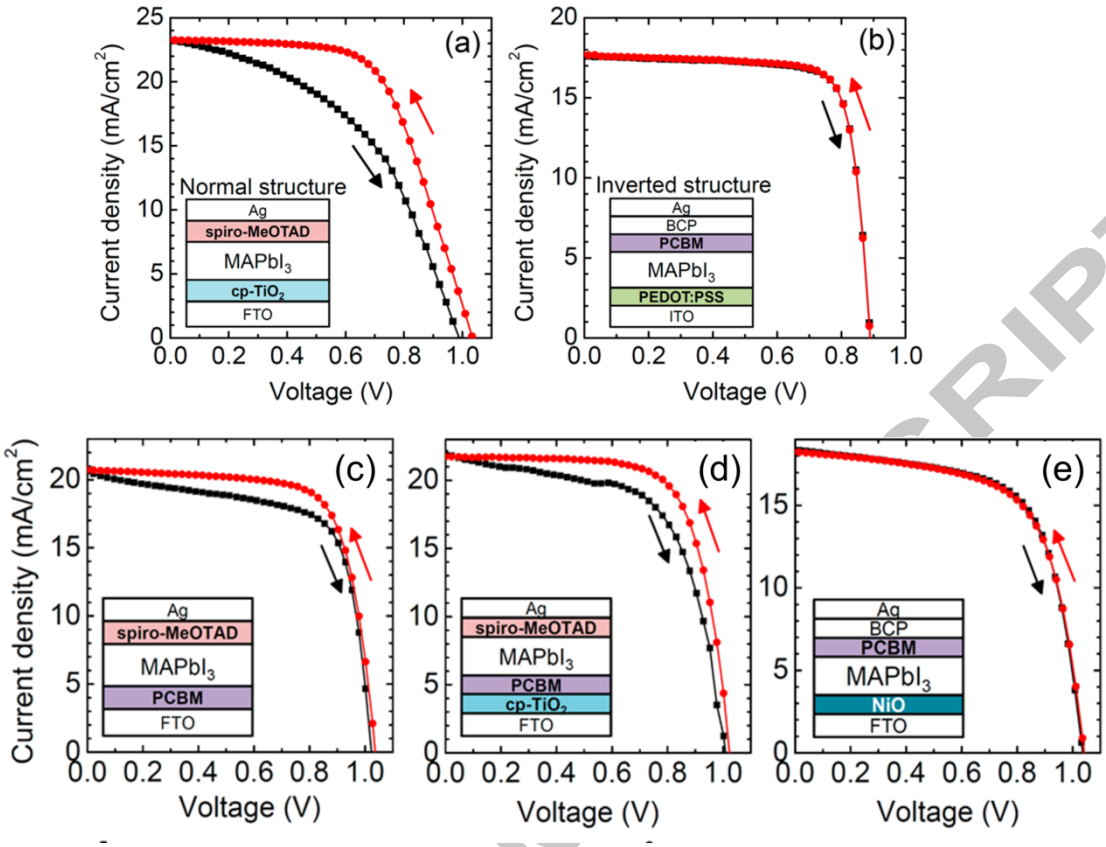

Fig. 39 I-V hysteresis of perovskite solar cells with different contact layers. Reprinted with permission from ref. [194]

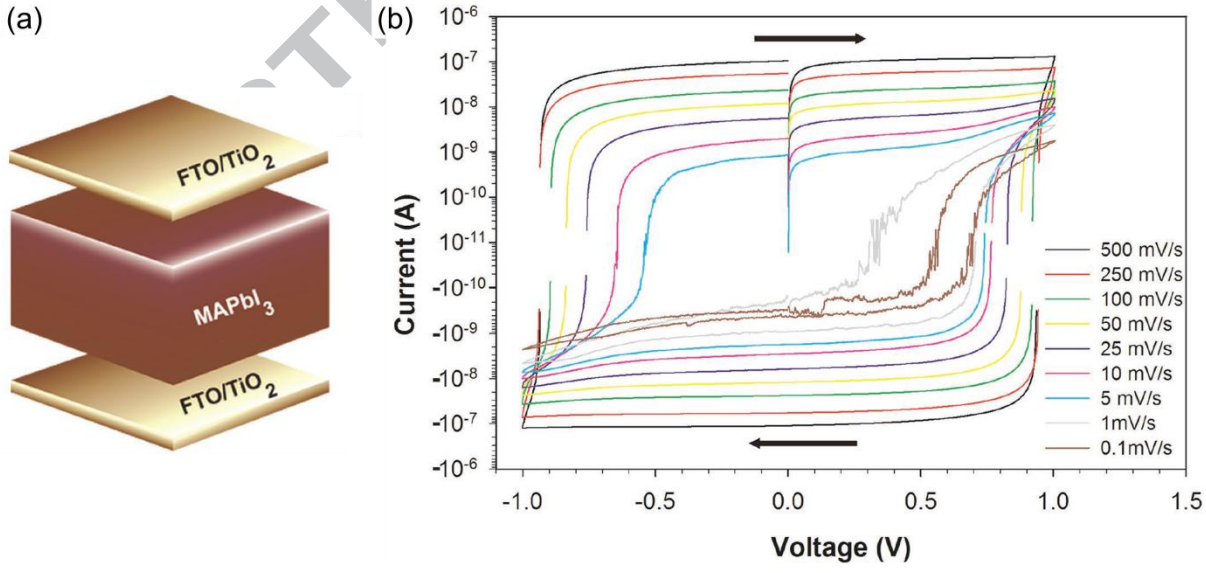

Fig. 40 (a) Structure of $MAPbI_3$ (500 µm) symmetric devices with TiO_2 contact layers, (b) Capacitive currents exhibited by $TiO_2/MAPbI_3/TiO_2$ samples. Perfect square-like, scan rate-dependent responses are obtained indicating electrode capacitance behavior. Reprinted with permission from ref. [195]

However, high efficiency (20.8%) perovskite based on TiO_2 and spiro contact layers are reported without any hysteresis in forward and reverse scan, and also with different scan rate (c.f. Fig. 41) [199]. The microstructure shown in Fig. 41 indicated the large grain size and thicker perovskite capping layer above TiO_2 layer. This points out the importance of microstructure and the crystallinity. More study on this aspect is needed.

To avoid the influence of the hysteresis and ensure comparability of research data, proposal is made for steady-state efficiency: measurement should be conducted at a fixed voltage near the maximum power point and at fixed applied bias until it stabilizes, as shown in Fig. 42 [196].

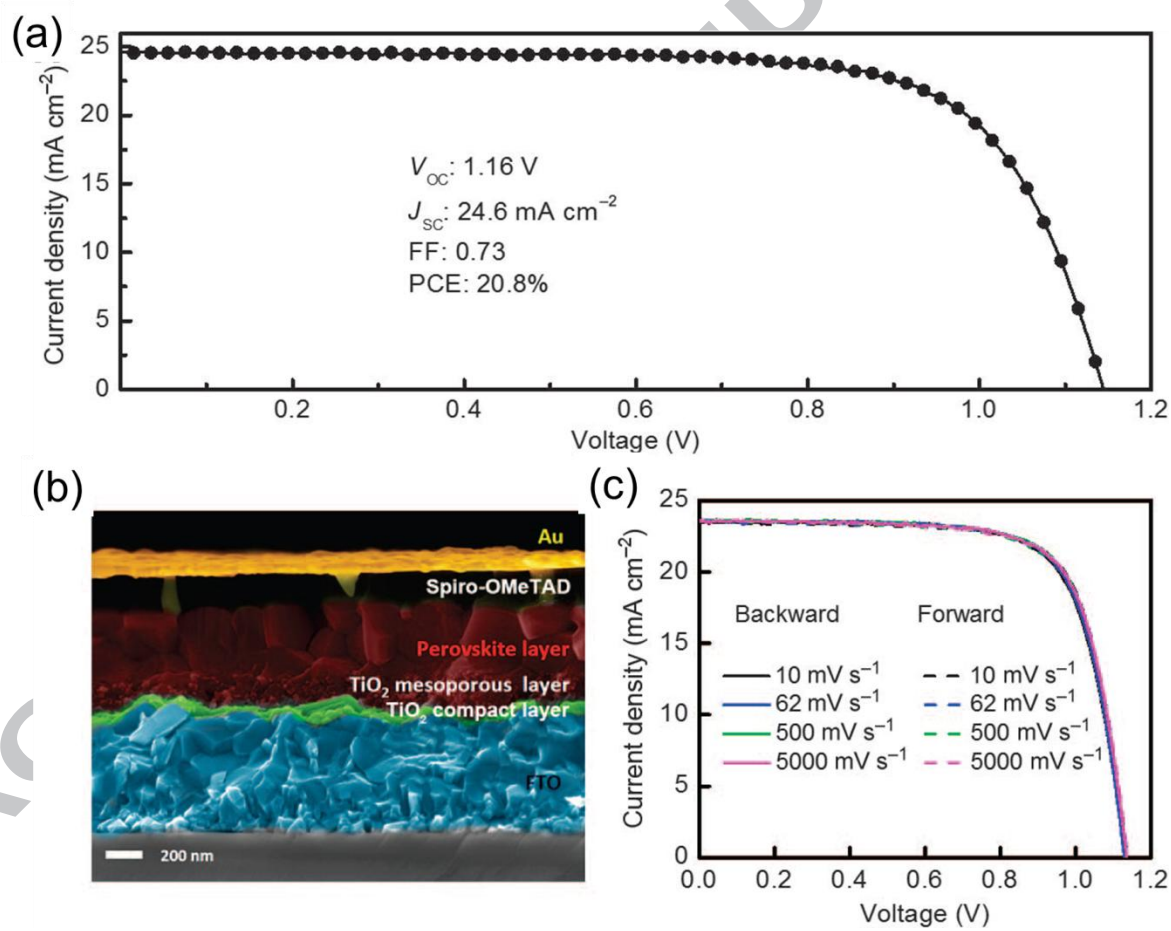

Fig. 41 (a) J-V curves for the champion solar cell under AM 1.5 G illumination, measured from Voc to Jsc,(b) Cross-sectional SEM image of the champion cell. (c) Hysteresis measurements of one PSC at different scanning speeds under AM 1.5 G illumination [197]

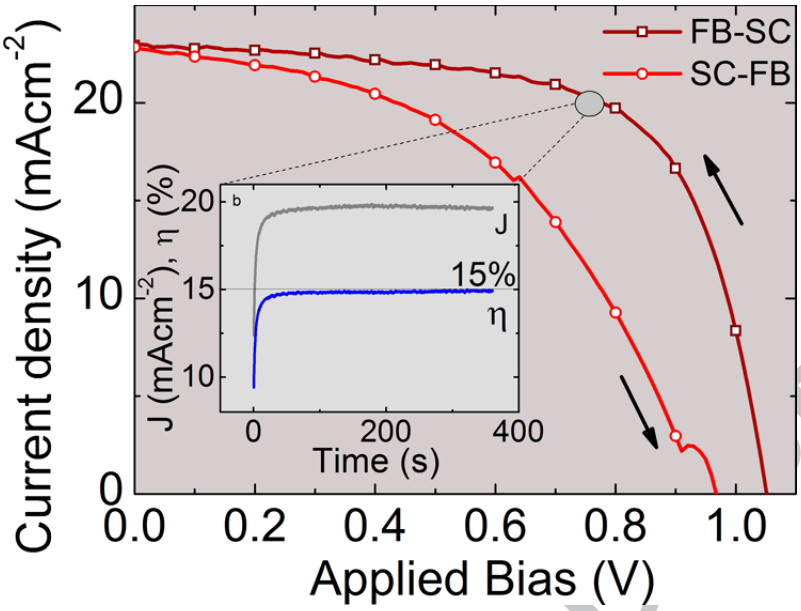

Fig. 42 Stabilized power output from a perovskite solar cell. Reprinted with permission from ref. [196]

4.2 Environmental stability of perovskite cells

It is commonly accepted that the environmental stability of solar cells includes stability against the combination of heat, moisture, oxygen and light. High temperature induces decomposition or phase change of perovskite materials. Device configuration, such as the electron and hole transporting materials will also affect the stability of perovskite solar cell. $MAPbI_3$ perovskite is considered highly sensitive to moisture thus degrades in the presence of water under light as follows [198, 199]:

$$\text{In presence of moisture: } CH_3NH_3PbI_3\ (s) + H_2O \longleftrightarrow [(CH_3NH_2)PbI_3][H_3O] \quad (9)$$

$$[(CH_3NH_2)PbI_3][H_3O] \longleftrightarrow CH_3NH_2\ (aq) + HI\ (aq) + PbI_2\ (s) \quad (10)$$

$$\text{In presence of oxygen: } 4HI\ (aq) + O_2 \longleftrightarrow 2I_2\ (s) + 2\,H_2O \quad (11)$$

$$\text{Under light: } 2HI\ (aq) + hv \longleftrightarrow H_2\ (g) + I_2\ (s) \quad (12)$$

In other words, moisture initiates the degradation of perovskite, while oxygen and light help to move the reaction forward. The processes are discussed in detail below.

4.2.1 Effect of heat

Table 3 lists the decomposition temperature and the stable temperature of several currently used perovskite materials. Bulk single crystal $CH_3NH_3PbI_3$ ($MAPbI_3$) starts to decompose when the temperature is above 240°C. But this temperature drops to around only 85°C when it is in the form of film [200]. The most important issue that limited the practical application of $MAPbI_3$ is that it undergoes phase change from tetragonal to cubic at 55°C – a very temperature right in the range of solar cell operation [201]. Substituting iodine with bromine can improve the temperature stability. It is believed that the organic cation $CH_3NH_3^+$ has strong dipole and different orientation which increase the disorder inside the crystal structure of $CH_3NH_3PbI_3$. Changing the $CH_3NH_3^+$ with $HC(NH_2)_2^+$, the stability dramatically improved. There is no phase change of $HC(NH_2)_2PbI_3$ at temperature lower than 150°C. However it is difficult to obtain pure and stable α phase (black) of $HC(NH_2)_2PbI_3$ as non-perovskite δ phase (yellow) forms easily or transforms from α phase through hydrolysis [201], thus detrimental to solar cell application. Further substituting organic cation with inorganic Cs to form $CsPbI_3$ or $CsPbBr_3$ completely eradicates decomposition up to their melting point. However, the $CsPbI_3$ and $CsPbBr_3$ compounds are non-perovskite orthorhombic at room temperature. $CsPbBr_3$ transfers to tetragonal (orange in color) at 130°C, $CsPbI_3$ transforms to tetragonal (black in color) ~300°C [202].

Table 3 Stable temperature of several perovskite compounds

Compound	$CH_3NH_3PbI_3$	$CH_3NH_3PbBr_3$	$HC(NH_2)_2]PbI_3$	$CsPbI_3$	$CsPbBr_3$
Decomposition temperature (°C)	240 (single crystal), [200] 85 (thin film)	257(single crystal),[200]	320-360(single crystal)[203]	>460[204]	>460[204]
Perovskite phase stable/forming temperature (°C)	55 [201]	~70	185(single crystal),[203] <150 (thin film)[205]	>300[204]	>130 [206, 207]

One of the strategies to solve the thermal stability problem is to add a small amount of MA into $FAPbI_3$, and thus forming $(MAFA)PbI_3$ to make use of the stronger dipoles in MA to strengthen the interactions between the MA cation and the inorganic PbI_6 octahedral cage. This hence improves the stability. Bein et al [208] added 17% of MA into FA to form $MA_{0.17}FA_{0.83}PbI_3$, and found no phase change from 25 to 250°C as

scanned in differential scanning calorimetry (DSC). As Br is one atomic period ahead of I, thus Br has stronger bond with Pb, addition of Br to replace some I is expected to further enhance stability. Seok et al further incorporated bromide into this system to form a stable black phase $MA_{0.15}FA_{0.85}Pb(Br_{0.15}I_{0.85})_3$ (measured up to 150°C) [209]. However, the addition of MA in $FAPbI_3$ does not necessarily solve the long term stability problem as $MAPbI_3$ itself has an inherent decomposition problem at only 85 °C. Park [210] mixed FA with Cs forming $FA_{0.9}Cs_{0.1}PbI_3$ with improved stability. Snaith [211] added Cs into $FAPb(IBr)_3$ to form $FA_{0.83}Cs_{0.17}Pb(I_{0.6}Br_{0.4})_3$. At 130°C for up to 6h, no change is observed in optical band gap and the crystal lattice. Extending this idea to its extreme, effectively replacing all FA with Cs in the compound to form $CsPb(I_2Br)$ [202], this produced a stable absorbance for 270 min at 85 °C in a relative humidity of 20~25%. Prolonged exposure to ambient, hours or days depending on humidity, this compound still instigated degradation into non-perovskite (yellow) phase.

In fact, non-stability of $MAPbI_3$ lies in its own thermodynamics as revealed by Wei et al. [212] through calculation of its decomposition energy (c.f., Table 4): at room-temperature, decomposition of $CH_3NH_3PbI_3$ into $CH_3NH_3I + PbI_2$ is exothermic. In other words, the commonly used perovskite, $CH_3NH_3PbI_3$, is inherently thermodynamically unstable, regardless of the humidity or oxygen in the atmosphere. Substituting iodine with bromine or chlorine turns tide (negative to positive, i.e., exothermic changes to endothermic). However, the quantum of the endothermic value is still too small even completely replacing I with Br. Accordingly, it is unpromising to stabilize $CH_3NH_3PbI_3$ with partial or even complete replacement of I with Br. If this is true, i.e., the instability is the intrinsic thermodynamic problem of $MAPbI_3$ perovskite itself, the encapsulation is of no use at all to avoid the effect of moisture or oxygen. As such, the direction of research should turn to MA-free or inorganic inclusion at "A" site in ABX_3, as shown in the calculation that addition of Cs does help to increase the level of endothermic energy (thus the stability of the perovskite).

Table 4 The calculated energy cost (in eV/f.u.) of the phase-separation reactions of the hybrid halide perovskites in three crystal polymorphs and with two exchange-correlation functionals (PBE and vdW-TS) [212]

Phase-Separation	cubic		tetragonal		orthorhombic	
	PBE	vdW	PBE	vdW	PBE	vdW
$CH_3NH_3PbI_3 \rightarrow CH_3NH_3I + PbI_2$	-0.111	-0.119	-0.060	-0.063	-0.031	0.037
$CH_3NH_3PbBr_3 \rightarrow CH_3NH_3Br + PbBr_2$	0.043	0.014	0.077	0.065	0.068	0.106
$CH_3NH_3PbCl_3 \rightarrow CH_3NH_3Cl + PbCl_2$	0.040	0.004	0.058	0.033	0.097	0.071
$CsPbI_3 \rightarrow CsI + PbI_2$	-0.069				0.098	
$CsPbBr_3 \rightarrow CsBr + PbBr_2$	0.127				0.209	
$CsPbCl_3 \rightarrow CsCl + PbCl_2$	0.224				0.292	

In summary, the thermal stability problem is a big or even fatal issue concerning development of perovskite solar cell into commercializing. Through composition design and modification to improve the stability is urgent for commercial applications.

4.2.2 Effect of moisture

Three models are established on possible decomposition of perovskite under moisture:

Walsh et al [115] proposed a simple acid-base reaction, seen in Fig. 41(a), with methylammonium lead iodide as an example, where a single water molecule is sufficient to decompose a perovskite molecule into $[(CH_3NH_2)PbI_3][H_3O]$ (c.f., Eq. (9), or process "a" in Fig. 41(a)). Kamat et al. [213], however, viewed it slightly different: before decomposition takes place, H_2O and perovskite molecules first form a hydrate product similar to $(CH_3NH_3)_4PbI_6{\cdot}2H_2O$. This was later confirmed by Kelly [214] through experiment. Excess moisture is needed to further drive this reaction to dissolve by-products HI and CH_3NH_2 ("b" and "c" in Fig. 43(a)). With sufficient moisture, the perovskite molecule finally degrades into CH_3NH_2 (aq) +HI (aq) +PbI_2 (s) (c.f., Eq. 10) and the color changes to yellow (solid PbI_2). Jena et al [199] further illustrated this process through molecular dynamics simulations (Fig. 43(b)). They believed that the water molecule first attacks the bond between $[CH_3NH_3]^+$ and $[PbI_3]^-$. Due to the huge negative charge on both the oxygen and the iodine atoms, the water molecule pushes the iodine away. The iodine atom then grasps one proton from the NH_3 group in $[CH_3NH_3]^+$ to form HI, CH_3NH_2 and water, leaving PbI_2 behind. Therefore the NH_3 group in organic cation is the culprit and the weak bond between Pb and I made it easily attacked.

As such, the way towards stability is to rid of these two causes. Park et al. [210] improved the photo- and moisture stability of perovskite film by replacing 10% of $HC(NH_2)_2^+$ with Cs^+, as shown in Fig. 44. EPFL researchers targeted both aspects by using Cs, MA and FA at "A" site and replacing some I with Br to strengthen the Pb-X bonding to achieve a consistent efficiency of 21.1% for continuous aging of 250h at operation condition [215].

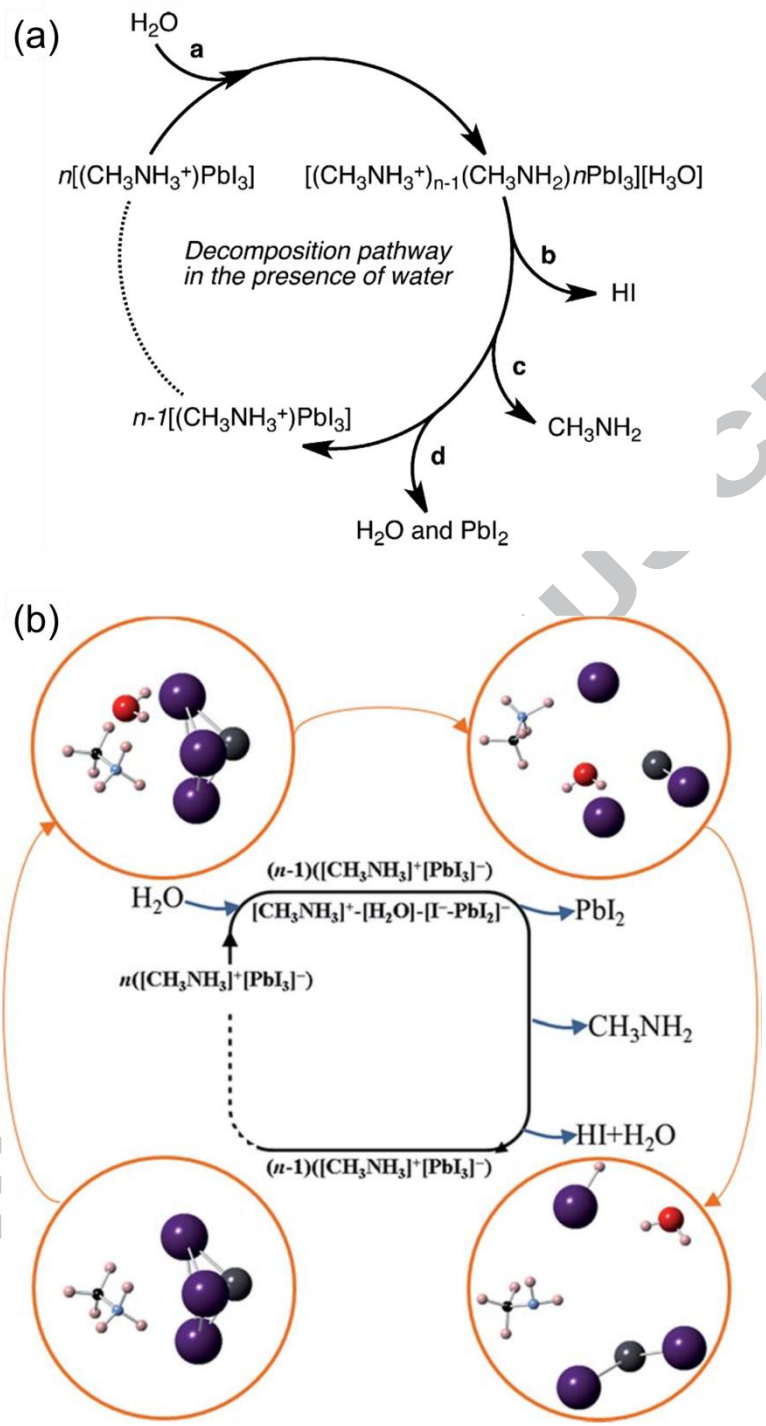

Fig. 43 (a) A. Walsh's model of possible decomposition mechanism of methylammonium lead iodide perovskite in the presence of water. A water molecule, a, is required to initiate the process of decomposition, being driven by dissolving of b/c in water or volatile of c, finally resulted in yellow color solid phase PbI_2, reprinted with permission from ref. [115] (b) Degradation mechanism of $CH_3NH_3PbI_3$ exposed to moisture proposed by P. Jena. The ball-and-stick plots (Pb: lead black; I: purple; N: cyan; C: black; O: red; H: pink) in the circles demonstrate the process in sequence as indicated by the arrows. It starts with the reactant as one water molecule is trapped between the super alkali $[CH_3NH_3]^+$ and super

halogen $[PbI_3]^-$ and ends up with products of PbI_2, CH_3NH_2, HI and H_2O, reprinted with permission from ref. [199]

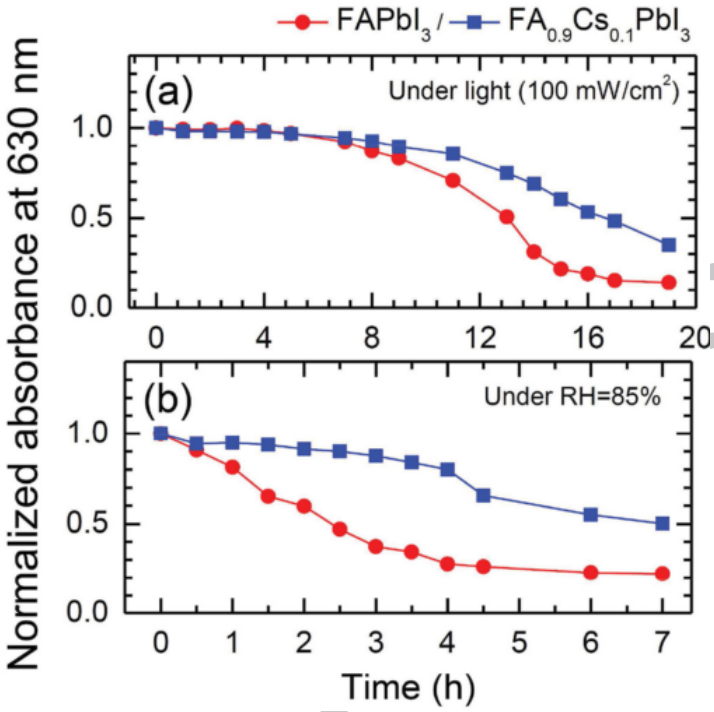

Fig. 44 Normalized absorbance of $FAPbI_3$ and $FA_{0.9}Cs_{0.1}PbI_3$ films measured a) under sulfur lamp (relative humidity (RH) < 50%, temperature (T) < 65 °C) and b) under constant humidity of RH 85% in dark (T =25 °C) as a function of time. The absorption spectra were measured every hour for photo-stability test and every half an hour for moisture-stability test. Reprinted with permission from ref. [210]

Even the lead source might also affect the stability of perovskite synthesized, as reported by Mora-Sero et al [216]: perovskite produced from $PbCl_2$ gives better stability than that from $Pb(OAc)_2$, (OAc = $CH_3CH_2COO^-$). As the morphology especially the crystal size varied significantly as the lead source changed, it is inconclusive whether the stability improvement is due to larger crystal size obtained from $PbCl_2$.

As illustrated in Fig. 43, moisture decomposition of the perovskite structure is realized through first breaking of the bonds between "A" site group and the PbI_3 group. If this bond can be strengthened or bonded to other groups of stronger affiliation than with H_2O, the stability should increase. Graetzel and coworkers [217] introduced butylphosphonic acid 4-ammonium chloride (4-ABPACl) into their perovskite solution and strong hydrogen bonding of the $-PO(OH)_2$ and $-NH_3^+$ forms to crosslink neighboring perovskite grains as shown in Fig. 45. This eliminates the chances of H_2O "invasion" into the boding of "A" site group and the PbI_3 group. The

device thus made remained its initial efficiency close to 14% for one week in ambient conditions at 55% relative humidity without encapsulation. In comparison, the efficiency of the cell without 4-ABPA "crosslinking treatment" degraded from ~7% to 1% under the same condition. This crosslinking can also be realized with other organics such as aliphatic fluorinated amphiphilic additive [218].

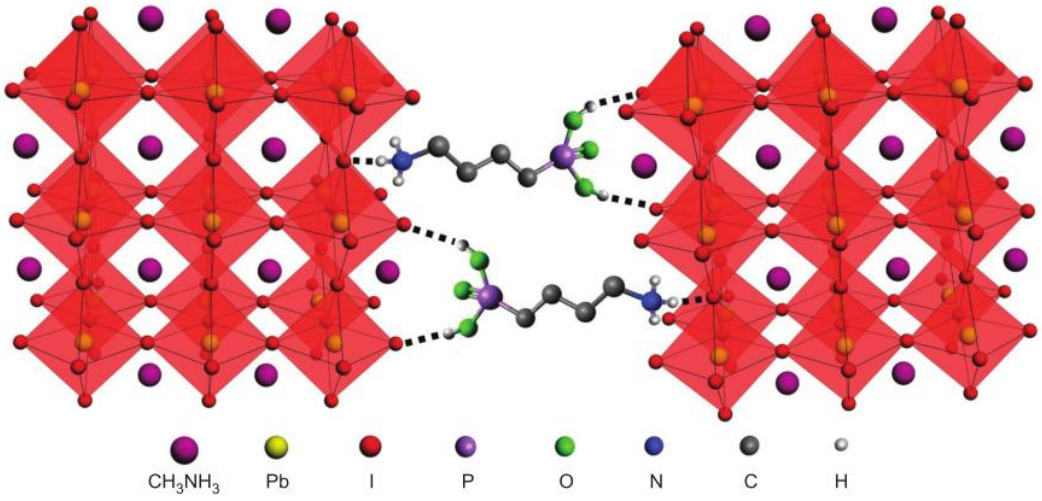

Fig. 45 Schematic illustration of two neighbouring grain structures in which the methyl ammonium groups are shown as one sphere for clarity, and the PbI_6^{4-} octahedral are shown in red, crosslinked by butylphosphonic acid 4-ammonium chloride (4-ABPACl) hydrogen-bonding interactions (O-H…I and N-H…I) of the iodide from the iodoplumbate complex with the phosphonic acid ($-PO(OH)_2$) and the ammonium ($-NH3^+$) end groups of the 4-ABPACl species. Reprinted with permission from ref. [217]

Replacing some of the "A"-site group with gigantic molecule effectively breaks up 3D into 2D lattice structure. The gigantic organic group slices 3D crystal structure and acts as a protection layer to avoid moisture attack. Fig. 46(a) showed the crystal structure of 2D hybrid perovskite $(PEA)_2(MA)_2[Pb_3I_{10}]$(PEA=$C_6H_5(CH_2)_2NH_3^+$, MA= $CH_3NH_3^+$), where the $(MA)[PbI_3]$ is sliced along specific crystallographic planes by PEA group [219]. The long chain of $C_6H_5(CH_2)_2$ in PEA group forming a protection layer to avoid the attack of moisture with NH_3^+ group and the Pb-I bond. This compound shows extremely moisture resistance. After exposure to a relative humidity of 52% for 46 days, the crystal structure did not change, being a new kind of moisture stable low dimensional perovskite (c.f. Fig. 46(b)) [219]. However the larger bandgap and lower solar cell efficiency of this kind of 2D materials should be balanced.

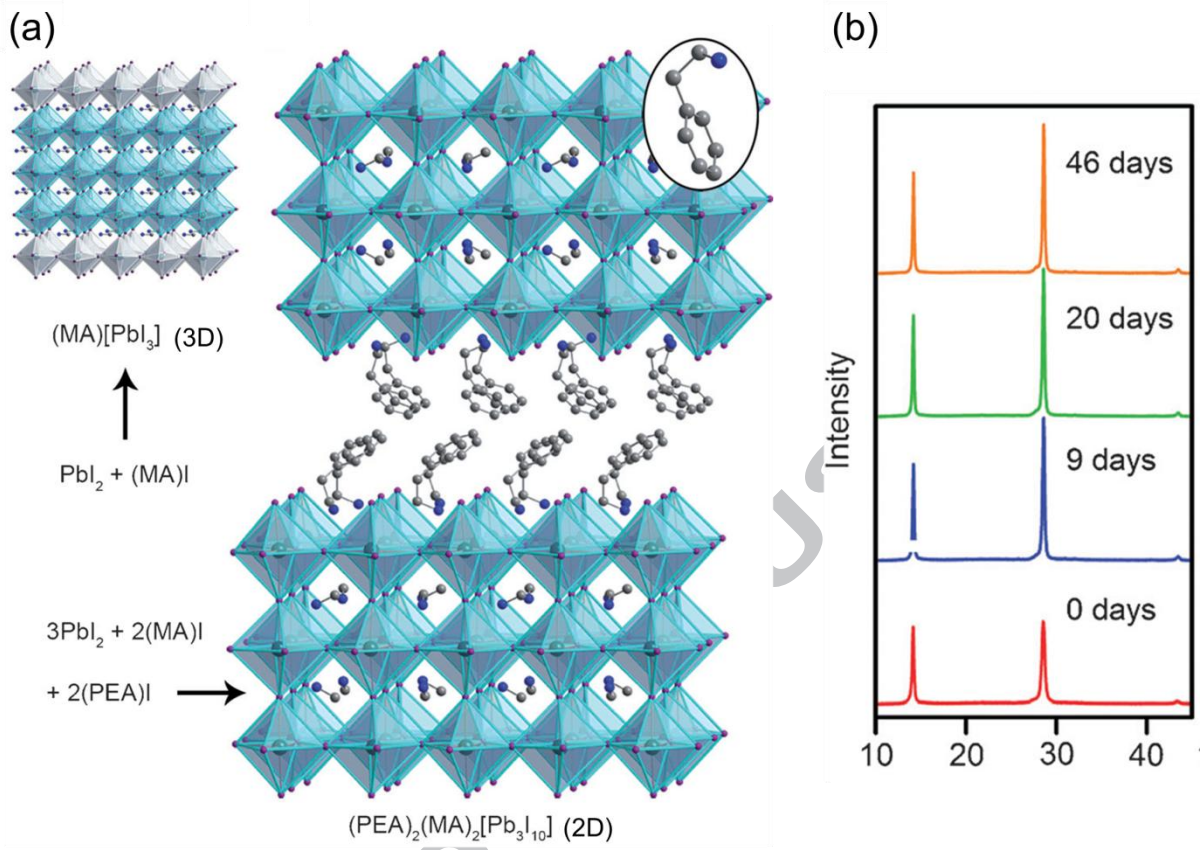

Fig. 46 (a) Crystal structure of 3D and 2D perovskite, (b) XRD pattern of $(PEA)_2(MA)_2[Pb_3I_{10}]$ after exposure to 52% relative humidity condition. Reprinted with permission from ref. [219]

2D or multidimensional perovskite has abundant chemistry to play with: breaking up of the 3D structure along different crystalline orientation coupled with inserting organic layer of different nature gives rise to vast possibilities of 2D structures. And in the same orientation of "cut", one can generate perovskites with a general formula $(RNH_3)_2A_{n-1}MnX_{3n+1}$ by tuning the number of inorganic layers *n* in the structure where n = 1 gives rise to a pure 2D layered; n = ∞, 3D structure; and n = other integer, quasi-2D layered structure as illustrated in Fig. 47 [220], where the center image is a 3D perovskite, the left is inserting an organic layer along the <110> orientation with n=2, and the right illustrate inserting the organic layer along <001> with different values of n. The stability of perovskite improves with the increasing of amount and size of organics. The drawback, however, is the detrimental increase of the barrier for the interlayer charge transportation and the binding energy of the exciton. Chemical strengthening of the bond between the organic and inorganic sheets and/or use of conductive organic cations should favor interlayer charge transportation.

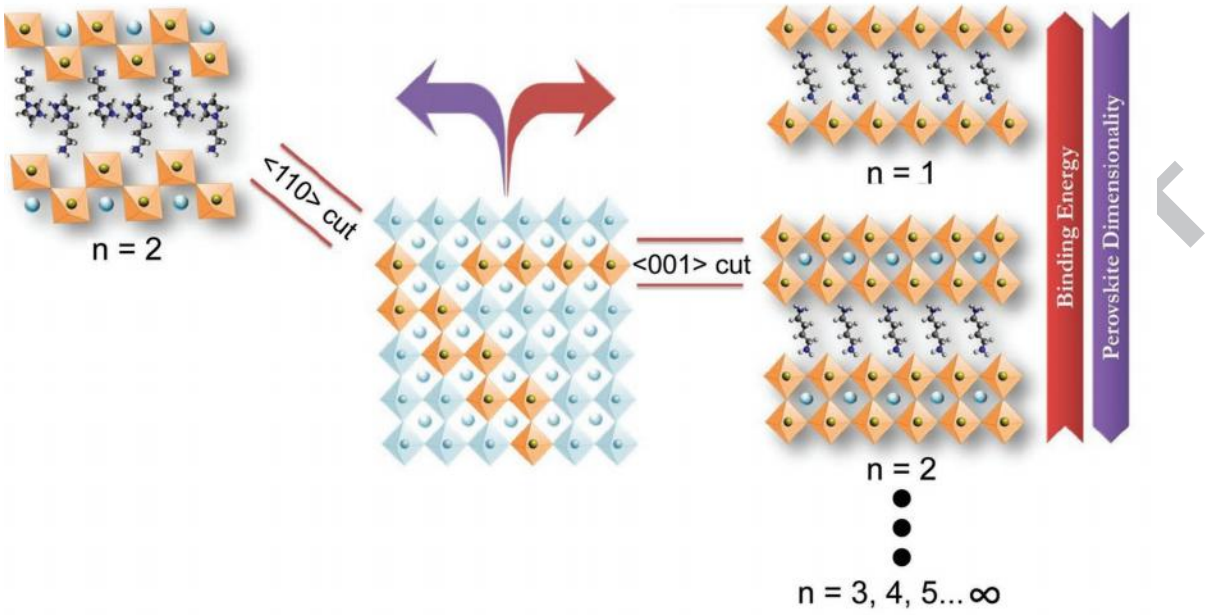

Fig. 47 Concept of multidimensionality in perovskite materials; introduction of large organic cations in the inorganic layers break the AMX_3 symmetry to form perovskites in <110> and <001> oriented A_2MX_4 layered structures. Reprinted with permission from ref. [220]

One significant phenomenon reported by Yang's group showed that, the efficiency of planar perovskite solar cell boosted to 19.3% produced in controlled humidity. The moisture seems like favorite the formation of perovskite. However the fabricated perovskite still suffer from moisture instability [221].

As can be seen, huge amount of interests have been attracted in the stability of perovskite materials in air atmosphere and many promising results came out. However, it is still far from practical application requirements and need further improvement.

4.2.3 Effect of oxygen and light

As indicated in Eq. 11 and 12, the product of the moisture decomposition of perovskite, HI, further decomposes to gaseous H_2 and I_2, with presence of oxygen and/or light, accelerating the degradation reaction. Should I be replaced by Br, HBr would be formed, but the stability of HBr against oxygen and light is much better than HI. The key of this chain reaction lies in the existence of moisture (H_2O) and I. If there is no presence of water or iodine is changed to bromine, oxygen or light induced degradation will be weakened. Katz et al [222] investigated the stability of replacing I with Br (c.f., Fig. 48): for encapsulated $MAPbI_3$ and $MAPbBr_3$, at room temperature there is no degradation in both cases as there is no moisture. However,

at elevated temperature, the trapped-in moisture acted thus in the case of $MAPbI_3$, HI formed thus degradation took place. But in the case of $MAPbBr_3$ even though there might be HBr formed there was no further reaction thus perovskite degradation disappeared.

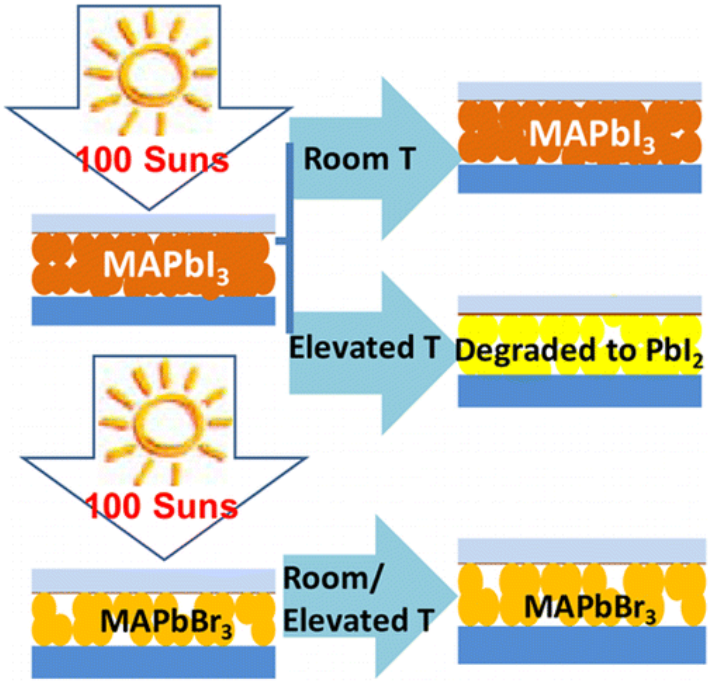

Fig. 48 Schematic illustration of the degradation of $MAPbI_3$ and $MAPbBr_3$ films under 100 suns and different temperature. The absorption of $MAPbI_3$ films degraded about 7% after exposure to 100 suns for 60 min at 45~55 °C. Reprinted with permission from ref. [222]

The UV light also acts to oxidize I^- into I_2 with presence of TiO_2 (as TiO_2 absorbs UV), thus degradation of perovskite ($MAPbI_3$ or $FAPbI_3$) into PbI_2 takes place. This is called photocatalytic degradation. Fig. 49 illustrates this process. TiO_2 has strong electron extraction ability from organic materials as photo-catalysts and from iodide (I^-) as electrodes in DSSCs. Extraction of electron by TiO_2 from an iodide anion (I^-) to form I_2 and from $CH_3NH_3^+$ to release CH_3NH_2 gas and H^+ (Fig. 49(a)). The byproducts, I_2 and H^+, react with I^- and HI is formed leaving PbI_2 behind. As such, breaking of the contact between TiO_2 with perovskite should stop this degradation. Coating the TiO_2 surface with Sb_2S_3 thus passivated the surface of TiO_2 and resulted better stability, as shown in Fig. 49(b)[223]. Similarly, a very thin Al_2O_3 layer on top of TiO_2 was also effective in improving UV stability [224]. CsBr was also used to passivate the surface of TiO_2 with improved stability [225]. Some even totally replaced TiO_2 with Al_2O_3 mesoporous scaffold [226] with stable performance over 1000h continuous exposure under full spectrum simulated sunlight.

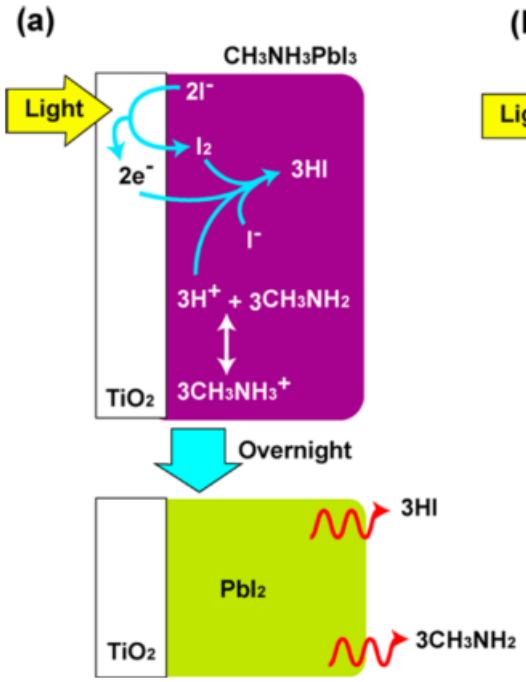

Fig. 49 Degradation scheme of $CH_3NH_3PbI_3$ perovskite solar cells during light exposure test: (a) $TiO_2/CH_3NH_3PbI_3$ and (b) $TiO_2/Sb_2S_3/CH_3NH_3PbI_3$. Reprinted with permission from ref. [223]

As TiO_2 absorbs only UV light, down-conversion of UV light into visible light avoids this photocatalytic degradation [227]. Coating a $YVO_4:Eu^{3+}$ nano-phosphor layer on the back side of FTO glass to face the incoming light effectively absorbs UV light and convert into visible light that, in turn, is absorbed by perovskite behind. This not only solves the UV stability problem, but also improves the photocurrent density by ~8.5%.

4.2.4 Effect of device structure

Aside from the environmental influences (heat, moisture, oxygen and light) discussed above, device structures also affect stability of the cells. As discussed in section 3.2, perovskite is ambipolar semiconductor, both electron and hole conducting layers are placed on both sides of perovskite layer to efficiently collect charges. Based on good band alignment with perovskite, nitrogen-containing donors, such as 2,20,7,70-tetrakis-(N,N-di-pmethoxyphenylamine)-9,90-spiro-bifluorene (spiro-OMeTAD, hereafter as spiro), is commonly used as hole transporting materials (HTM) for perovskite. However, besides the high price, spiro suffers from

low hole mobility and conductivity because the sp3 hybridization of the nitrogen atom, the inherent triangular pyramid configuration lead to large intermolecular distances (c.f. Fig. 50) , therefore p-type dopants (or additives), such as Li-TFSI (Li-bis(trifluoromethanesulfonyl) imide)), are used to improve the conductivity. 4-*tert*-butylpyridine (TBP) is also commonly added into HTM to suppress the photogenerated electron recombination from TiO_2 to electrolyte and reduces energy loss in DSSC [228]. It also helps to increase the polarity of HTM, as thus improving the contact between perovskite and HTM. The devices with TBP normally get higher open circuit voltage. These additives, as well as acetonitrile (a solvent used for Li-TFSI), will degrade the perovskite layer. For example, TBP tends to react with PbI_2, forming [PbI_2·TBP] complexes, leads to decomposition of perovskite [229]. To solve this problem, montmorillonite (MMT) was used forming a buffer layer to protect perovskite from contact with HTM to improve the stability of cell [229]. As a replacement of Li-TFSI, a dual functional ionic liquid N-butyl-N0-(4-pyridylheptyl) imidazolium bis(trifluoromethane) sulfonamide (BuPyIm-TFSI) is introduced to improve the conductivity of HTM and also suppress the recombination [230].

To get rid of the additives all together, researches into totally replacing spiro as hole transporting materials are reported. Ionic liquid N-butyl-N0-(4-pyridylheptyl) imidazolium bis(triuoromethane) sulfonamide (TTF-1, Fig. 50) [231]has been used as a replacement for spiro because this small molecule with planar configurations exhibits strong intermolecular π– π stacking. The device made from TTF-1 gave an efficiency of 11%, less than the 11.4% from spiro, but two times more stable in air. Due to the relatively higher HOMO level of TTF-1 (-5.0 eV) compared to spiro (-5.4 eV), the open circuit voltage of device from TTF-1 dropped. Other materials to replace spiro, such as Polythiophene [232], silolothiophene-linked triphenylamines [233], are also reported.

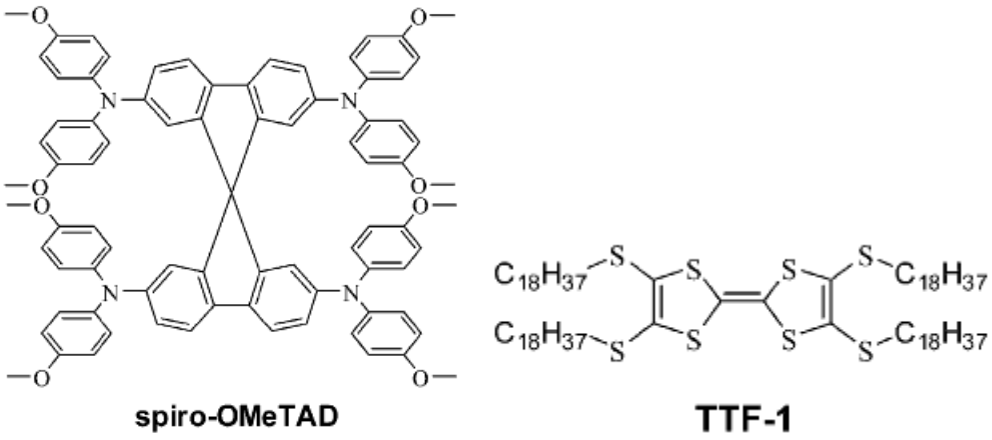

Fig. 50 Molecular structures of spiro-OMeTAD and TTF-1. Reprinted with permission from ref. [231]

As inorganic materials are much more stable against moisture, oxygen and light (because of strong covalent or ionic bond), searches are started for brand new inorganic hole transporting materials such as WO_3 [234], NiO_x, [235] or carbon nanotube/polymer composites [236] etc. The stability of device dramatically improved, however, the band position of inorganic is difficult to adjust compared to organic molecule. Since inorganic layers normally need high temperature sintering, researchers are trying to find low temperature solution process to fabricate these layers.

As use of hole transporting materials causes so much problem, what happens if not using it at all? Fig. 51 illustrates a HTM-free structure where perovskite was drop-casted from a solution of PbI_2, MAI and 5-ammoniumvaleric acid (5-AVA) iodide through the top porous carbon film. The device achieved a certified power conversion efficiency of 12.8% and was stable for >1000h in ambient air under full sunlight [113].

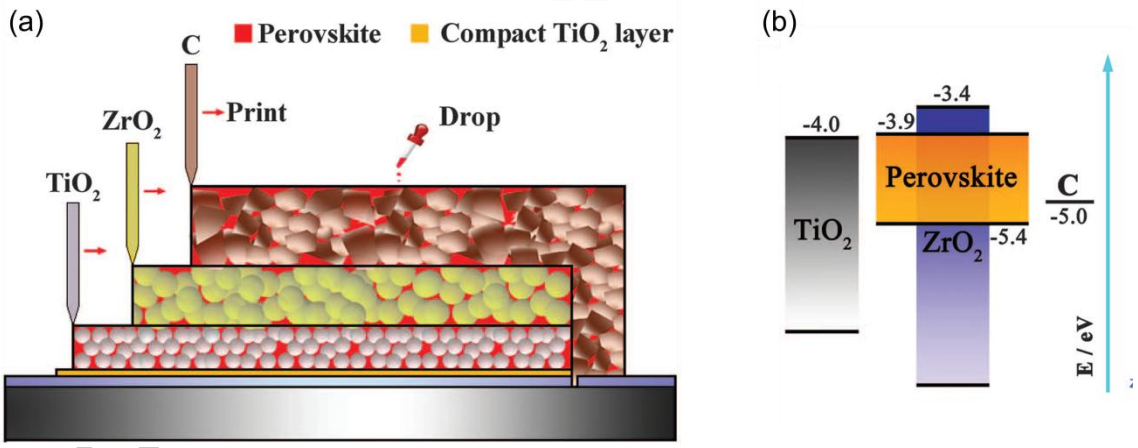

Fig. 51 (a) Schematic drawing showing the cross section of the triple-layer perovskite–based fully printable mesoscopic solar cell, (b) Energy band diagram of the triple-layer device [113]

4.3 Device Encapsulation

Encapsulation of the whole device with hydrophobic coating has been widely used in commercial solar cells, such as silicon, CIGS, OPV, DSSC, and so on, to improve the stability.

Adopted from the advanced encapsulation technique for the organic light emitting diode technology, in which one desiccant from Dynic is placed between cells and the cover glass to absorb moisture leaking into the device during sealing and measurement [237]. The cover glass was then sealed through a UV-curable epoxy resin. All sealed cell showed degradation after exposure to 55°C, 80% relative humidity and one sun illumination, although the advanced sealing method improved the stability (Fig. 52). Therefore effective encapsulation methods are urgent.

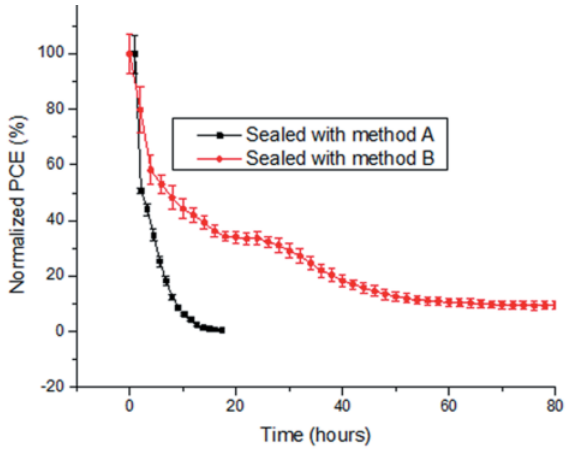

Fig. 52 Comparison of the stability of devices sealed without (method A) or with (method B) additional desiccant tested under environmental temperature of 55°C (cell real temperature of 85°C), 80% relative humidity and one sun illumination. Reprinted with permission from ref. [237]

5. Summary

To summarize, current key obstacles in the four major cell categories are as follows:

1. The most outstanding problem hindering polycrystalline inorganic $Cu(In,Ga)(S,Se)_2$ solar cells' large scale application is the high cost vacuum process and the expensive materials. Low cost solution processes are being studied to rid the need of vacuum, with limited success. Use of cheap Zn and Sn in place of expensive Ga and In to form $Cu_2ZnSn(S,Se)_4$ is promising if the composition sensitivity can be pacified for better manufacturing controllability, and the occurrence of deep defects be suppressed.

2. The existence of large amount of dangling bonds in hydrogenated amorphous silicon limits the diffusion length of the charge carriers thus the charge collection efficiency. One way out may be the formation of a structure in which nanosized crystalline silicon domains are imbedded in amorphous silicon matrix.

3. The key problems in organic photovoltaics are the low charge carrier mobility and high exciton binding energy. Single crystalline organic domain can expect to enhance the charge carrier mobility. Organic absorbers that delocalize the distribution of electron and holes could also help. The high exciton binding energy problem is associated with dielectric constant thus can be reduced through introduction of inorganic element(s) into the organics.

4. The most notorious problem hindering application of organic-inorganic halide perovskite solar cells is the environmental stability especially with respect to moisture, heat and light. Composition design to introduce inorganic element at A-site of perovskite is expected to improve stability at high temperature. Multi/mixed dimensional (2D or 3D or the mix) structure may be able to appease sensitivity against moisture. For perovskite solar cells to be commercially viable, intrinsic reliability (solving of the hysteresis problem) and environmental stability (heat, moisture, light, etc.) are of top importance and priority in further research.

In terms of strategies in achieving high efficiency the following aspects worth mentioning:

In light harvesting, energy bandgap can be adjusted through composition modification with elements of different electronegativity and crystal structure alternation with different size unit cell. A higher structural dimension (1D, 2D or 3D) narrows the bandgap thus favors light harvesting process. Better light harvesting can also be achieved through tandem structure, multiple-exciton generation using quantum dot effect and up or down conversion to combine low energy photons to excite higher energy photoelectron or split high energy photon into multiple lower energy photons.

Charge dissociation or separation is easily achieved through a p-n junction in inorganic solar cells. In organics, however, heterojunctions have to be used to separate the electron and hole pairs in the exciton. In amorphous silicon the bipolar conductivity enables separation of holes and electrons with a p-i-n junction. Ferroelectric domain and built-in electric field were proposed as charge dissociation mechanisms for organic-inorganic perovskite. However, these hypotheses are still challenged. The reported open-circuit voltages with different contact materials suggested that the charge selection materials as well as the perovskite itself contribute to the charge dissociation.

The most important parameters determining the charge carrier transport are mobility and diffusion length, which in turn, are affected by effective mass, mean scattering time and life time of the charge carriers. Composition and band structure design enable reduction of effective mass thus increasing mobility. Bigger grain size or less grain boundary area reduces scattering thus lengthens the charge carrier life time.

Processing parametric study is another important aspect in achieving high efficiency as surface non-continuity, pin-hole and various defects all serve as channels for current leakage or charge scattering centers that adversely affect charge carrier life and diffusion length.

Acknowledgements

This work is supported by Singapore Ministry of Education Tier 1 project RG187/14 and Ministry of Science and Technology of the Republic of China under contract No. of 104-2221-E-212-002-MY3.

Reference

[1] Würfel P. Limitations on Energy Conversion in Solar Cells. Physics of Solar Cells: Wiley-VCH Verlag GmbH; 2007. p. 137-53.
[2] Reinhard P, Chirila A, Blosch P, Pianezzi F, Nishiwaki S, Buechelers S, et al. Review of Progress Toward 20% Efficiency Flexible CIGS Solar Cells and Manufacturing Issues of Solar Modules. Photovoltaics, IEEE Journal of. 2013;3:572-80.
[3] Wagner S, Shay JL, Migliorato P, Kasper HM. CuInSe2/CdS heterojunction photovoltaic detectors. Applied Physics Letters. 1974;25:434-5.
[4] Best Research-Cell Efficiencies. Released by National Renewable Energy Laboratory. 2016.
[5] Wang W, Winkler MT, Gunawan O, Gokmen T, Todorov TK, Zhu Y, et al. Device Characteristics of CZTSSe Thin-Film Solar Cells with 12.6% Efficiency. Advanced Energy Materials. 2014;4:1301465.
[6] Suryawanshi MP, Agawane GL, Bhosale SM, Shin SW, Patil PS, Kim JH, et al. CZTS based thin film solar cells: a status review. Materials Technology. 2013;28:98-109.
[7] Kentaro I, Tatsuo N. Electrical and Optical Properties of Stannite-Type Quaternary Semiconductor Thin Films. Japanese Journal of Applied Physics. 1988;27:2094.
[8] Sterling HF, Swann RCG. Chemical vapour deposition promoted by r.f. discharge. Solid-State Electronics. 1965;8:653-4.
[9] Zeman M. Advanced Amorphous Silicon Solar Cell Technologies. Thin Film Solar Cells: John Wiley & Sons, Ltd; 2006. p. 173-236.
[10] Spear WE, Le Comber PG. Substitutional doping of amorphous silicon. Solid State Communications. 1975;17:1193-6.

[11] Nelson J. Organic photovoltaic films. Current Opinion in Solid State and Materials Science. 2002;6:87-95.
[12] Jef Poortmans VA. Thin Film Solar Cells: Fabrication, Characterization and Applications. In: Jef Poortmans VA, editor. Thin Film Solar Cells: John Wiley & Sons, Ltd; 2006. p. i-xxix.
[13] der Wiel Bv, Egelhaaf H-J, Issa H, Roos M, Henze N. Market Readiness of Organic Photovoltaics for Building Integration. MRS Online Proceedings Library. 2014;1639:null-null.
[14] Green MA, Emery K, Hishikawa Y, Warta W, Dunlop ED. Solar cell efficiency tables (version 46). Progress in Photovoltaics: Research and Applications. 2015;23:805-12.
[15] Grätzel M. Nanocrystalline Injection Solar Cells. In: Arkhipov JPa, editor. Thin Film Solar Cells: John Wiley & Sons, Ltd; 2006. p. 363-85.
[16] Kojima A, Teshima K, Shirai Y, Miyasaka T. Organometal halide perovskites as visible-light sensitizers for photovoltaic cells. J Am Chem Soc. 2009;131:6050-1.
[17] Kim HS, Lee CR, Im JH, Lee KB, Moehl T, Marchioro A, et al. Lead iodide perovskite sensitized all-solid-state submicron thin film mesoscopic solar cell with efficiency exceeding 9%. Scientific reports. 2012;2:591.
[18] Sum TC, Mathews N. Advancements in perovskite solar cells: photophysics behind the photovoltaics. Energy Environ Sci. 2014;7:2518-34.
[19] Yang WS, Noh JH, Jeon NJ, Kim YC, Ryu S, Seo J, et al. High-performance photovoltaic perovskite layers fabricated through intramolecular exchange. Science. 2015;348:1234-7.
[20] Shockley W, Queisser HJ. Detailed Balance Limit of Efficiency of p‐n Junction Solar Cells. Journal of Applied Physics. 1961;32:510-9.
[21] Shah A. Thin-Film Silicon Solar Cells: EPFL Press; 2010.
[22] Green MA. Solar cells: operating principles, technology, and system applications1982.
[23] Jaffe JE, Zunger A. Anion displacements and the band-gap anomaly in ternary ABC2 chalcopyrite semiconductors. Physical Review B. 1983;27:5176-9.
[24] Chen S, Walsh A, Yang J-H, Gong XG, Sun L, Yang P-X, et al. Compositional dependence of structural and electronic properties of Cu2ZnSn(S,Se)4 alloys for thin film solar cells. Physical Review B. 2011;83:125201.
[25] Contreras MA, Mansfield LM, Egaas B, Li J, Romero M, Noufi R, et al. Wide bandgap Cu(In,Ga)Se2 solar cells with improved energy conversion efficiency. Progress in Photovoltaics: Research and Applications. 2012;20:843-50.
[26] Wei S-H, Zhang SB, Zunger A. Effects of Ga addition to CuInSe2 on its electronic, structural, and defect properties. Applied Physics Letters. 1998;72:3199-201.
[27] Persson C. Anisotropic hole-mass tensor of CuIn1−xGax(S,Se)2: Presence of free carriers narrows the energy gap. Applied Physics Letters. 2008;93:072106.
[28] Sun LY, Kazmerski LL, Clark AH, Ireland PJ, Morton DW. Absorption coefficient measurements for vacuum‐deposited Cu‐ternary thin films. Journal of Vacuum Science & Technology. 1978;15:265-8.
[29] Chichibu S, Mizutani T, Murakami K, Shioda T, Kurafuji T, Nakanishi H, et al. Band gap energies of bulk, thin-film, and epitaxial layers of CuInSe2 and CuGaSe2. Journal of Applied Physics. 1998;83:3678-89.
[30] Metzger WK. The potential and device physics of interdigitated thin-film solar cells. Journal of Applied Physics. 2008;103:094515.
[31] Metzger WK, Repins IL, Romero M, Dippo P, Contreras M, Noufi R, et al. Recombination kinetics and stability in polycrystalline Cu(In,Ga)Se2 solar cells. Thin Solid Films. 2009;517:2360-4.
[32] Gloeckler M, Fahrenbruch AL, Sites JR. Numerical modeling of CIGS and CdTe solar cells: setting the baseline. Photovoltaic Energy Conversion, 2003 Proceedings of 3rd World Conference on2003. p. 491-4 Vol.1.

[33] Chandramohan M, S.Velumani, Venkatachalam T. Band structure calculations of Cu(In1−xGax)Se2. Materials Science and Engineering: B. 2010;174:200-4.
[34] Minemoto T, Matsui T, Takakura H, Hamakawa Y, Negami T, Hashimoto Y, et al. Theoretical analysis of the effect of conduction band offset of window/CIS layers on performance of CIS solar cells using device simulation. Solar Energy Materials and Solar Cells. 2001;67:83-8.
[35] Lee J, Cohen JD, Shafarman WN. The determination of carrier mobilities in CIGS photovoltaic devices using high-frequency admittance measurements. Thin Solid Films. 2005;480–481:336-40.
[36] Liu H-R, Chen S, Zhai Y-T, Xiang HJ, Gong XG, Wei S-H. First-principles study on the effective masses of zinc-blend-derived Cu2Zn−IV−VI4 (IV = Sn, Ge, Si and VI = S, Se). Journal of Applied Physics. 2012;112:093717.
[37] Zhao H, Persson C. Optical properties of Cu(In,Ga)Se2 and Cu2ZnSn(S,Se)4. Thin Solid Films. 2011;519:7508-12.
[38] Singh J. Effective mass of charge carriers in amorphous semiconductors and its applications. Journal of Non-Crystalline Solids. 2002;299–302, Part 1:444-8.
[39] Kalema VN, Aljishi S, Dawson RMA, Slobodin D, Wagner S. The dielectric constants of a-Si,Ge:H,F alloys. Materials Letters. 1986;4:320-2.
[40] Stoumpos CC, Frazer L, Clark DJ, Kim YS, Rhim SH, Freeman AJ, et al. Hybrid Germanium Iodide Perovskite Semiconductors: Active Lone Pairs, Structural Distortions, Direct and Indirect Energy Gaps, and Strong Nonlinear Optical Properties. Journal of the American Chemical Society. 2015;137:6804-19.
[41] Hao F, Stoumpos CC, Cao DH, Chang RPH, Kanatzidis MG. Lead-free solid-state organic-inorganic halide perovskite solar cells. Nat Photon. 2014;8:489-94.
[42] Bernal C, Yang K. First-Principles Hybrid Functional Study of the Organic–Inorganic Perovskites CH3NH3SnBr3 and CH3NH3SnI3. The Journal of Physical Chemistry C. 2014;118:24383-8.
[43] Umari P, Mosconi E, De Angelis F. Relativistic GW calculations on CH3NH3PbI3 and CH3NH3SnI3 perovskites for solar cell applications. Scientific reports. 2014;4:4467.
[44] Boix PP, Agarwala S, Koh TM, Mathews N, Mhaisalkar SG. Perovskite Solar Cells: Beyond Methylammonium Lead Iodide. The Journal of Physical Chemistry Letters. 2015;6:898-907.
[45] Du MH. Efficient carrier transport in halide perovskites: theoretical perspectives. Journal of Materials Chemistry A. 2014;2:9091-8.
[46] Yin W-J, Yang J-H, Kang J, Yan Y, Wei S-H. Halide perovskite materials for solar cells: a theoretical review. J Mater Chem A. 2015;3:8926-42.
[47] Giorgi G, Fujisawa J-I, Segawa H, Yamashita K. Small Photocarrier Effective Masses Featuring Ambipolar Transport in Methylammonium Lead Iodide Perovskite: A Density Functional Analysis. The Journal of Physical Chemistry Letters. 2013;4:4213-6.
[48] Federico Brivio KTB, Aron Walsh, and Mark van Schilfgaarde. Relativistic quasiparticle self-consistent electronic structure of hybrid halide perovskite photovoltaic absorbers. Phys Rev B. 2014;89:6.
[49] Noh JH, Im SH, Heo JH, Mandal TN, Seok SI. Chemical Management for Colorful, Efficient, and Stable Inorganic–Organic Hybrid Nanostructured Solar Cells. Nano Letters. 2013;13:1764-9.
[50] Kitazawa N, Watanabe Y, Nakamura Y. Optical properties of CH3NH3PbX3 (X = halogen) and their mixed-halide crystals. Journal of Materials Science. 2002;37:3585-7.
[51] Li G, Zhu R, Yang Y. Polymer solar cells. Nat Photon. 2012;6:153-61.
[52] Northrup JE. Atomic and electronic structure of polymer organic semiconductors: P3HT, PQT, and PBTTT. Phys Rev B. 2007;76:6.

[53] Johns JE, Muller EA, Frechet JMJ, Harris CB. The Origin of Charge Localization Observed in Organic Photovoltaic Materials. Journal of the American Chemical Society. 2010;132:15720-5.
[54] Amat A, Mosconi E, Ronca E, Quarti C, Umari P, Nazeeruddin MK, et al. Cation-Induced Band-Gap Tuning in Organohalide Perovskites: Interplay of Spin–Orbit Coupling and Octahedra Tilting. Nano Letters. 2014;14:3608-16.
[55] Kieslich G, Sun S, Cheetham AK. Solid-state principles applied to organic-inorganic perovskites: new tricks for an old dog. Chemical Science. 2014;5:4712-5.
[56] Yuan D-X, Gorka A, Xu M-F, Wang Z-K, Liao L-S. Inverted planar NH2CH=NH2PbI3 perovskite solar cells with 13.56% efficiency via low temperature processing. Physical Chemistry Chemical Physics. 2015;17:19745-50.
[57] Li C, Lu X, Ding W, Feng L, Gao Y, Guo Z. Formability of ABX3 (X = F, Cl, Br, I) halide perovskites. Acta Crystallographica Section B. 2008;64:702-7.
[58] Goldschmidt VM. Crystal structure and chemical combination. Berichte der deutschen chemischen Gesellschaft (A and B Series). 1927;60:1263-96.
[59] Mitzi DB. Templating and structural engineering in organic-inorganic perovskites. Journal of the Chemical Society, Dalton Transactions. 2001:1-12.
[60] Keldysh L. Coulomb interaction in thin semiconductor and semimetal films. ZhETF Pisma Redaktsiiu. 1979;29:716.
[61] Mitzi DB. Synthesis, Structure, and Properties of Organic-Inorganic Perovskites and Related Materials. Progress in Inorganic Chemistry: John Wiley & Sons, Inc.; 2007. p. 1-121.
[62] Papavassiliou GC. Synthetic Three-and Lower-Dimensional Semiconductors Based on Inorganic Units. Molecular Crystals and Liquid Crystals Science and Technology Section A Molecular Crystals and Liquid Crystals. 1996;286:231-8.
[63] Chen C-C, Dou L, Gao J, Chang W-H, Li G, Yang Y. High-performance semi-transparent polymer solar cells possessing tandem structures. Energy & Environmental Science. 2013;6:2714-20.
[64] Kinoshita T, Nonomura K, Joong Jeon N, Giordano F, Abate A, Uchida S, et al. Spectral splitting photovoltaics using perovskite and wideband dye-sensitized solar cells. Nat Commun. 2015;6.
[65] Fu F, Feurer T, Jager T, Avancini E, Bissig B, Yoon S, et al. Low-temperature-processed efficient semi-transparent planar perovskite solar cells for bifacial and tandem applications. Nat Commun. 2015;6.
[66] Lunt RR, Bulovic V. Transparent, near-infrared organic photovoltaic solar cells for window and energy-scavenging applications. Applied Physics Letters. 2011;98:113305.
[67] Betancur R, Romero-Gomez P, Martinez-Otero A, Elias X, Maymo M, Martorell J. Transparent polymer solar cells employing a layered light-trapping architecture. Nat Photon. 2013;7:995-1000.
[68] Yu W, Shen L, Shen P, Long Y, Sun H, Chen W, et al. Semitransparent Polymer Solar Cells with 5% Power Conversion Efficiency Using Photonic Crystal Reflector. ACS Applied Materials & Interfaces. 2014;6:599-605.
[69] Dissanayake DMNM, Roberts B, Ku P-C. Angular selective backreflector for semitransparent photovoltaics. Applied Physics Letters. 2012;101:063302.
[70] Galagan Y, Debije MG, Blom PWM. Semitransparent organic solar cells with organic wavelength dependent reflectors. Applied Physics Letters. 2011;98:043302.
[71] Kong E-H, Chang Y-J, Jang H. Hierarchically Nanostructured Photoelectrodes for Quantum-Dot-Sensitized Solar Cells. In: Wu J, Wang ZM, editors. Quantum Dot Solar Cells: Springer New York; 2014. p. 39-66.

[72] Semonin OE, Luther JM, Choi S, Chen H-Y, Gao J, Nozik AJ, et al. Peak External Photocurrent Quantum Efficiency Exceeding 100% via MEG in a Quantum Dot Solar Cell. Science. 2011;334:1530-3.
[73] Böhm ML, Jellicoe TC, Tabachnyk M, Davis NJLK, Wisnivesky-Rocca-Rivarola F, Ducati C, et al. Lead Telluride Quantum Dot Solar Cells Displaying External Quantum Efficiencies Exceeding 120%. Nano Letters. 2015.
[74] Wegh RT, Donker H, Oskam KD, Meijerink A. Visible Quantum Cutting in LiGdF4:Eu3+ Through Downconversion. Science. 1999;283:663-6.
[75] Zhang QY, Huang XY. Recent progress in quantum cutting phosphors. Progress in Materials Science. 2010;55:353-427.
[76] Richards BS. Enhancing the performance of silicon solar cells via the application of passive luminescence conversion layers. Solar Energy Materials and Solar Cells. 2006;90:2329-37.
[77] Trupke T, Green MA, Würfel P. Improving solar cell efficiencies by down-conversion of high-energy photons. Journal of Applied Physics. 2002;92:1668-74.
[78] Saxena VN. Phosphors for Solar Cells: Tb-Doped Lanthanum Fluoride & Th-Doped Calcium Tungstate. Indian J Pure Appl Phys. 1983;21:306-7.
[79] Huang Z, Li X, Mahboub M, Hanson KM, Nichols VM, Le H, et al. Hybrid Molecule–Nanocrystal Photon Upconversion Across the Visible and Near-Infrared. Nano Letters. 2015;15:5552-7.
[80] Güdel HU, Pollnau M. Near-infrared to visible photon upconversion processes in lanthanide doped chloride, bromide and iodide lattices. Journal of Alloys and Compounds. 2000;303–304:307-15.
[81] Imanieh MH, Martin IR, Gonzalez-Platas J, Eftekhari Yekta B, Marghussian VK, Shakhesi S. Behavior of Yb3+ and Er3+ during Heat Treatment in Oxyfluoride Glass Ceramics. Journal of Nanomaterials. 2014;2014:10.
[82] Wang H-Q, Batentschuk M, Osvet A, Pinna L, Brabec CJ. Rare-Earth Ion Doped Up-Conversion Materials for Photovoltaic Applications. Advanced Materials. 2011;23:2675-80.
[83] Shan G-B, Demopoulos GP. Near-Infrared Sunlight Harvesting in Dye-Sensitized Solar Cells Via the Insertion of an Upconverter-TiO2 Nanocomposite Layer. Advanced Materials. 2010;22:4373-7.
[84] Roldán-Carmona C, Malinkiewicz O, Betancur R, Longo G, Momblona C, Jaramillo F, et al. High efficiency single-junction semitransparent perovskite solar cells. Energy & Environmental Science. 2014;7:2968.
[85] Amin N, Chelvanathan P, Hossain MI, Sopian K. Numerical Modelling of Ultra Thin Cu(In,Ga)Se2 Solar Cells. Energy Procedia. 2012;15:291-8.
[86] Li-Kao ZJ, Naghavi N, Erfurth F, Guillemoles JF, Gérard I, Etcheberry A, et al. Towards ultrathin copper indium gallium diselenide solar cells: proof of concept study by chemical etching and gold back contact engineering. Progress in Photovoltaics: Research and Applications. 2012;20:582-7.
[87] Shiu K-T, Zimmerman J, Wang H, Forrest SR. Ultrathin film, high specific power InP solar cells on flexible plastic substrates. Applied Physics Letters. 2009;95:223503.
[88] Yoon J, Baca AJ, Park S-I, Elvikis P, Geddes JB, Li L, et al. Ultrathin silicon solar microcells for semitransparent, mechanically flexible and microconcentrator module designs. Nat Mater. 2008;7:907-15.
[89] Wang KX, Yu Z, Liu V, Cui Y, Fan S. Absorption Enhancement in Ultrathin Crystalline Silicon Solar Cells with Antireflection and Light-Trapping Nanocone Gratings. Nano Letters. 2012;12:1616-9.

[90] Eperon GE, Bryant D, Troughton J, Stranks SD, Johnston MB, Watson T, et al. Efficient, Semitransparent Neutral-Colored Solar Cells Based on Microstructured Formamidinium Lead Trihalide Perovskite. The Journal of Physical Chemistry Letters. 2015;6:129-38.
[91] Bailie CD, Christoforo MG, Mailoa JP, Bowring AR, Unger EL, Nguyen WH, et al. Semi-transparent perovskite solar cells for tandems with silicon and CIGS. Energy & Environmental Science. 2015;8:956-63.
[92] Chen C-C, Dou L, Zhu R, Chung C-H, Song T-B, Zheng YB, et al. Visibly Transparent Polymer Solar Cells Produced by Solution Processing. ACS Nano. 2012;6:7185-90.
[93] Meiss J, Holzmueller F, Gresser R, Leo K, Riede M. Near-infrared absorbing semitransparent organic solar cells. Applied Physics Letters. 2011;99:193307.
[94] Lin H-W, Chen Y-H, Huang Z-Y, Chen C-W, Lin L-Y, Lin F, et al. Highly efficient bifacial transparent organic solar cells with power conversion efficiency greater than 3% and transparency of 50%. Organic Electronics. 2012;13:1722-8.
[95] Guo F, Kubis P, Stubhan T, Li N, Baran D, Przybilla T, et al. Fully Solution-Processing Route toward Highly Transparent Polymer Solar Cells. ACS Applied Materials & Interfaces. 2014;6:18251-7.
[96] Zhang K, Qin C, Yang X, Islam A, Zhang S, Chen H, et al. High-Performance, Transparent, Dye-Sensitized Solar Cells for See-Through Photovoltaic Windows. Advanced Energy Materials. 2014;4:1301966.
[97] Zhao Y, Meek GA, Levine BG, Lunt RR. Near-Infrared Harvesting Transparent Luminescent Solar Concentrators. Advanced Optical Materials. 2014;2:606-11.
[98] Dvorak M, Wei S-H, Wu Z. Origin of the Variation of Exciton Binding Energy in Semiconductors. Physical Review Letters. 2013;110:016402.
[99] Valenta IPaJ. Luminescence Spectroscopy of Semiconductors: Oxford University Press; 2012.
[100] Shockley W. The theory of p-n junctions in semiconductors and p-n junction transistors. Bell System Technical Journal, The. 1949;28:435-89.
[101] Edri E, Kirmayer S, Mukhopadhyay S, Gartsman K, Hodes G, Cahen D. Elucidating the charge carrier separation and working mechanism of CH3NH3PbI(3-x)Cl(x) perovskite solar cells. Nat Commun. 2014;5:3461.
[102] Kurtz HA. LUMO energies and negative electron affinities. Journal of Chemical Education. 1984;61:580.
[103] Zhan C-G, Nichols JA, Dixon DA. Ionization Potential, Electron Affinity, Electronegativity, Hardness, and Electron Excitation Energy: Molecular Properties from Density Functional Theory Orbital Energies. The Journal of Physical Chemistry A. 2003;107:4184-95.
[104] Alam M, Ray B, Khan M, Dongaonkar S. The Essence and Efficiency Limits of Bulk-Heterostructure Organic Solar Cells. MRS Online Proceedings Library. 2012;1390:null-null.
[105] Alam MA, Ray B, Khan MR, Dongaonkar S. The essence and efficiency limits of bulk-heterostructure organic solar cells: A polymer-to-panel perspective. Journal of Materials Research. 2013;28:541-57.
[106] Hu H, Jiang K, Yang G, Liu J, Li Z, Lin H, et al. Terthiophene-Based D–A Polymer with an Asymmetric Arrangement of Alkyl Chains That Enables Efficient Polymer Solar Cells. Journal of the American Chemical Society. 2015;137:14149-57.
[107] Jung HS, Park NG. Perovskite solar cells: from materials to devices. Small. 2015;11:10-25.
[108] Song Y, Lv S, Liu X, Li X, Wang S, Wei H, et al. Energy level tuning of TPB-based hole-transporting materials for highly efficient perovskite solar cells. Chemical Communications. 2014;50:15239-42.
[109] Lee MM, Teuscher J, Miyasaka T, Murakami TN, Snaith HJ. Efficient hybrid solar cells based on meso-superstructured organometal halide perovskites. Science. 2012;338:643-7.

[110] Correa-Baena J-P, Anaya M, Lozano G, Tress W, Domanski K, Saliba M, et al. Unbroken Perovskite: Interplay of Morphology, Electro-optical Properties, and Ionic Movement. Advanced Materials. 2016:n/a-n/a.
[111] Heo JH, Han HJ, Kim D, Ahn TK, Im SH. Hysteresis-less inverted CH3NH3PbI3 planar perovskite hybrid solar cells with 18.1% power conversion efficiency. Energy & Environmental Science. 2015;8:1602-8.
[112] Cohen B-E, Aharon S, Dymshits A, Etgar L. Impact of Antisolvent Treatment on Carrier Density in Efficient Hole-Conductor-Free Perovskite-Based Solar Cells. The Journal of Physical Chemistry C. 2016;120:142-7.
[113] Mei A, Li X, Liu L, Ku Z, Liu T, Rong Y, et al. A hole-conductor-free, fully printable mesoscopic perovskite solar cell with high stability. Science. 2014;345:295-8.
[114] Rong Y, Liu L, Mei A, Li X, Han H. Beyond Efficiency: the Challenge of Stability in Mesoscopic Perovskite Solar Cells. Advanced Energy Materials. 2015:n/a-n/a.
[115] Frost JM, Butler KT, Brivio F, Hendon CH, van Schilfgaarde M, Walsh A. Atomistic Origins of High-Performance in Hybrid Halide Perovskite Solar Cells. Nano Letters. 2014;14:2584-90.
[116] Deng Y, Xiao Z, Huang J. Light-Induced Self-Poling Effect on Organometal Trihalide Perovskite Solar Cells for Increased Device Efficiency and Stability. Advanced Energy Materials. 2015:1500721.
[117] Eames C, Frost JM, Barnes PRF, O/'Regan BC, Walsh A, Islam MS. Ionic transport in hybrid lead iodide perovskite solar cells. Nat Commun. 2015;6.
[118] Guerrero A, Juarez-Perez EJ, Bisquert J, Mora-Sero I, Garcia-Belmonte G. Electrical field profile and doping in planar lead halide perovskite solar cells. Applied Physics Letters. 2014;105:133902.
[119] Correa Baena JP, Steier L, Tress W, Saliba M, Neutzner S, Matsui T, et al. Highly Efficient Planar Perovskite Solar Cells through Band Alignment Engineering. Energy & Environmental Science. 2015.
[120] Park M, Kim J-Y, Son HJ, Lee C-H, Jang SS, Ko MJ. Low-temperature solution-processed Li-doped SnO2 as an effective electron transporting layer for high-performance flexible and wearable perovskite solar cells. Nano Energy. 2016;26:208-15.
[121] Gouda L, Gottesman R, Ginsburg A, Keller DA, Haltzi E, Hu J, et al. Open Circuit Potential Build-Up in Perovskite Solar Cells from Dark Conditions to 1 Sun. The Journal of Physical Chemistry Letters. 2015:4640-5.
[122] Jiang C-S, Noufi R, AbuShama JA, Ramanathan K, Moutinho HR, Pankow J, et al. Local built-in potential on grain boundary of Cu(In,Ga)Se2 thin films. Applied Physics Letters. 2004;84:3477-9.
[123] Kim GY, Oh SH, Nguyen BP, Jo W, Kim BJ, Lee DG, et al. Efficient Carrier Separation and Intriguing Switching of Bound Charges in Inorganic–Organic Lead Halide Solar Cells. The Journal of Physical Chemistry Letters. 2015;6:2355-62.
[124] Zeghbroeck V. Principles of Semiconductor Devices2011.
[125] Gfroerer TH, Zhang Y, Wanlass MW. An extended defect as a sensor for free carrier diffusion in a semiconductor. Applied Physics Letters. 2013;102:012114.
[126] P. OJWaB. The Electrical Characterization of Semiconductors: Measurement of Minority Carrier Properties: Academic Press, San Diego; 1990.
[127] Finger AN. Using a Semiconductor Defect to Connect Diffusion Lengths and Lifetimes: Davidson College; 2014.
[128] Koutselas IB, Ducasse L, Papavassiliou GC. Electronic properties of three- and low-dimensional semiconducting materials with Pb halide and Sn halide units. Journal of Physics: Condensed Matter. 1996;8:1217.

[129] Wang Y, Gould T, Dobson JF, Zhang H, Yang H, Yao X, et al. Density functional theory analysis of structural and electronic properties of orthorhombic perovskite CH3NH3PbI3. Physical Chemistry Chemical Physics. 2014;16:1424-9.
[130] Umebayashi T, Asai K, Kondo T, Nakao A. Electronic structures of lead iodide based low-dimensional crystals. Physical Review B. 2003;67:155405.
[131] Im J-H, Kim H-S, Park N-G. Morphology-photovoltaic property correlation in perovskite solar cells: One-step versus two-step deposition of CH3NH3PbI3. APL Mater. 2014;2:081510.
[132] Huang F, Dkhissi Y, Huang W, Xiao M, Benesperi I, Rubanov S, et al. Gas-assisted preparation of lead iodide perovskite films consisting of a monolayer of single crystalline grains for high efficiency planar solar cells. Nano Energy. 2014;10:10-8.
[133] Ahn N, Son D-Y, Jang I-H, Kang SM, Choi M, Park N-G. Highly Reproducible Perovskite Solar Cells with Average Efficiency of 18.3% and Best Efficiency of 19.7% Fabricated via Lewis Base Adduct of Lead(II) Iodide. Journal of the American Chemical Society. 2015;137:8696-9.
[134] Zhang W, Saliba M, Moore DT, Pathak SK, Hörantner MT, Stergiopoulos T, et al. Ultrasmooth organic–inorganic perovskite thin-film formation and crystallization for efficient planar heterojunction solar cells. Nat Commun. 2015;6.
[135] Moore DT, Sai H, Tan KW, Smilgies D-M, Zhang W, Snaith HJ, et al. Crystallization Kinetics of Organic–Inorganic Trihalide Perovskites and the Role of the Lead Anion in Crystal Growth. Journal of the American Chemical Society. 2015;137:2350-8.
[136] Moore DT, Sai H, Wee Tan K, Estroff LA, Wiesner U. Impact of the organic halide salt on final perovskite composition for photovoltaic applications. APL Mater. 2014;2:081802.
[137] Jiang C-S, Noufi R, Ramanathan K, AbuShama JA, Moutinho HR, Al-Jassim MM. Does the local built-in potential on grain boundaries of Cu(In,Ga)Se2 thin films benefit photovoltaic performance of the device? Applied Physics Letters. 2004;85:2625-7.
[138] Visoly-Fisher I, Cohen SR, Gartsman K, Ruzin A, Cahen D. Understanding the Beneficial Role of Grain Boundaries in Polycrystalline Solar Cells from Single-Grain-Boundary Scanning Probe Microscopy. Advanced Functional Materials. 2006;16:649-60.
[139] Kim GY, Jeong AR, Kim JR, Jo W, Son D-H, Kim D-H, et al. Surface potential on grain boundaries and intragrains of highly efficient Cu2ZnSn(S,Se)4 thin-films grown by two-step sputtering process. Solar Energy Materials and Solar Cells. 2014;127:129-35.
[140] Yin WJ, Shi T, Yan Y. Unique properties of halide perovskites as possible origins of the superior solar cell performance. Adv Mater. 2014;26:4653-8.
[141] Yun JS, Ho-Baillie A, Huang S, Woo SH, Heo Y, Seidel J, et al. Benefit of Grain Boundaries in Organic–Inorganic Halide Planar Perovskite Solar Cells. The Journal of Physical Chemistry Letters. 2015;6:875-80.
[142] Edri E, Kirmayer S, Henning A, Mukhopadhyay S, Gartsman K, Rosenwaks Y, et al. Why lead methylammonium tri-iodide perovskite-based solar cells require a mesoporous electron transporting scaffold (but not necessarily a hole conductor). Nano Lett. 2014;14:1000-4.
[143] Cui P, Fu P, Wei D, Li M, Song D, Yue X, et al. Reduced surface defects of organometallic perovskite by thermal annealing for highly efficient perovskite solar cells. RSC Advances. 2015;5:75622-9.
[144] Xiao Z, Dong Q, Bi C, Shao Y, Yuan Y, Huang J. Solvent annealing of perovskite-induced crystal growth for photovoltaic-device efficiency enhancement. Adv Mater. 2014;26:6503-9.
[145] You J, Yang Y, Hong Z, Song T-B, Meng L, Liu Y, et al. Moisture assisted perovskite film growth for high performance solar cells. Applied Physics Letters. 2014;105:183902.
[146] Yang M, Zhou Y, Zeng Y, Jiang C-S, Padture NP, Zhu K. Square-Centimeter Solution-Processed Planar CH3NH3PbI3 Perovskite Solar Cells with Efficiency Exceeding 15%. Advanced Materials. 2015:6363-70.

[147] Nie W, Tsai H, Asadpour R, Blancon J-C, Neukirch AJ, Gupta G, et al. High-efficiency solution-processed perovskite solar cells with millimeter-scale grains. Science. 2015;347:522-5.
[148] Yin W-J, Shi T, Yan Y. Unusual defect physics in CH3NH3PbI3 perovskite solar cell absorber. Applied Physics Letters. 2014;104:063903.
[149] Stranks SD, Eperon GE, Grancini G, Menelaou C, Alcocer MJP, Leijtens T, et al. Electron-Hole Diffusion Lengths Exceeding 1 Micrometer in an Organometal Trihalide Perovskite Absorber. Science. 2013;342:341-4.
[150] Su Z, Tan JMR, Li X, Zeng X, Batabyal SK, Wong LH. Cation Substitution of Solution-Processed Cu2ZnSnS4 Thin Film Solar Cell with over 9% Efficiency. Advanced Energy Materials. 2015:1500682.
[151] Guo Q, Ford GM, Yang W-C, Hages CJ, Hillhouse HW, Agrawal R. Enhancing the performance of CZTSSe solar cells with Ge alloying. Solar Energy Materials and Solar Cells. 2012;105:132-6.
[152] Ford GM, Guo Q, Agrawal R, Hillhouse HW. Earth Abundant Element Cu2Zn(Sn1−xGex)S4 Nanocrystals for Tunable Band Gap Solar Cells: 6.8% Efficient Device Fabrication. Chemistry of Materials. 2011;23:2626-9.
[153] D'Innocenzo V, Grancini G, Alcocer MJ, Kandada AR, Stranks SD, Lee MM, et al. Excitons versus free charges in organo-lead tri-halide perovskites. Nat Commun. 2014;5:3586.
[154] Chung I, Song J-H, Im J, Androulakis J, Malliakas CD, Li H, et al. CsSnI3: Semiconductor or Metal? High Electrical Conductivity and Strong Near-Infrared Photoluminescence from a Single Material. High Hole Mobility and Phase-Transitions. Journal of the American Chemical Society. 2012;134:8579-87.
[155] Noel NK, Stranks SD, Abate A, Wehrenfennig C, Guarnera S, Haghighirad A-A, et al. Lead-free organic?inorganic tin halide perovskites for photovoltaic applications. Energy & Environmental Science. 2014;7:3061-8.
[156] Kumar MH, Dharani S, Leong WL, Boix PP, Prabhakar RR, Baikie T, et al. Lead-free halide perovskite solar cells with high photocurrents realized through vacancy modulation. Adv Mater. 2014;26:7122-7.
[157] Chirilă A, Buecheler S, Pianezzi F, Bloesch P, Gretener C, Uhl AR, et al. Highly efficient Cu(In,Ga)Se2 solar cells grown on flexible polymer films. Nat Mater. 2011;10:857-61.
[158] Vijila C, Singh SP, Williams E, Sonar P, Pivrikas A, Philippa B, et al. Relation between charge carrier mobility and lifetime in organic photovoltaics. Journal of Applied Physics. 2013;114:184503.
[159] Nguyen L-N, Kumar Pradhan S, Yen C-N, Lin M-C, Chen C-H, Wu C-S, et al. High performance phototransistors based on single crystalline perylene-tetracarboxylic-dianhydride nanoparticle. Applied Physics Letters. 2013;103:183301.
[160] Zhang W, Smith J, Watkins SE, Gysel R, McGehee M, Salleo A, et al. Indacenodithiophene Semiconducting Polymers for High-Performance, Air-Stable Transistors. Journal of the American Chemical Society. 2010;132:11437-9.
[161] de Haas MP, Warman JM, Anthopoulos TD, de Leeuw DM. The Mobility and Decay Kinetics of Charge Carriers in Pulse-Ionized Microcrystalline PCBM Powder. Advanced Functional Materials. 2006;16:2274-80.
[162] Zhan X, Tan Za, Domercq B, An Z, Zhang X, Barlow S, et al. A High-Mobility Electron-Transport Polymer with Broad Absorption and Its Use in Field-Effect Transistors and All-Polymer Solar Cells. Journal of the American Chemical Society. 2007;129:7246-7.
[163] Parkinson P, Lloyd-Hughes J, Johnston MB, Herz LM. Efficient generation of charges via below-gap photoexcitation of polymer-fullerene blend films investigated by terahertz spectroscopy. Physical Review B. 2008;78:115321.

[164] Wei HX, Li J, Xu ZQ, Cai Y, Tang JX, Li YQ. Thermal annealing-induced vertical phase separation of copper phthalocyanine: Fullerene bulk heterojunction in organic photovoltaic cells. Applied Physics Letters. 2010;97:083302.
[165] Ebadian S, Gholamkhass B, Shambayati S, Holdcroft S, Servati P. Effects of annealing and degradation on regioregular polythiophene-based bulk heterojunction organic photovoltaic devices. Solar Energy Materials and Solar Cells. 2010;94:2258-64.
[166] Ray B, Alam MA. A compact physical model for morphology induced intrinsic degradation of organic bulk heterojunction solar cell. Applied Physics Letters. 2011;99:033303.
[167] Ray B, Nair PR, Alam MA. Annealing dependent performance of organic bulk-heterojunction solar cells: A theoretical perspective. Solar Energy Materials and Solar Cells. 2011;95:3287-94.
[168] Lyons BP, Clarke N, Groves C. The relative importance of domain size, domain purity and domain interfaces to the performance of bulk-heterojunction organic photovoltaics. Energy & Environmental Science. 2012;5:7657-63.
[169] Chen W, Wu Y, Yue Y, Liu J, Zhang W, Yang X, et al. Efficient and stable large-area perovskite solar cells with inorganic charge extraction layers. Science. 2015.
[170] Sun L, Zhang S, Wang X, Sun XW, Ong DY, Ko Kyaw AK. A novel parallel configuration of dye-sensitized solar cells with double-sided anodic nanotube arrays. Energy & Environmental Science. 2011;4:2240-8.
[171] Niesen B, Rand BP, Van Dorpe P, Cheyns D, Tong L, Dmitriev A, et al. Plasmonic Efficiency Enhancement of High Performance Organic Solar Cells with a Nanostructured Rear Electrode. Advanced Energy Materials. 2013;3:145-50.
[172] Hu Z, Zhang J, Zhao Y. Effect of textured electrodes with light-trapping on performance of polymer solar cells. Journal of Applied Physics. 2012;111:104516.
[173] Wang X, Sun L, Zhang S, Wang X. Ultralong, Small-Diameter TiO2 Nanotubes Achieved by an Optimized Two-Step Anodization for Efficient Dye-Sensitized Solar Cells. ACS Applied Materials & Interfaces. 2014;6:1361-5.
[174] Wei J, Zhao Y, Li H, Li G, Pan J, Xu D, et al. Hysteresis Analysis Based on the Ferroelectric Effect in Hybrid Perovskite Solar Cells. The Journal of Physical Chemistry Letters. 2014;5:3937-45.
[175] Kim H-S, Kim SK, Kim BJ, Shin K-S, Gupta MK, Jung HS, et al. Ferroelectric Polarization in CH3NH3PbI3 Perovskite. The Journal of Physical Chemistry Letters. 2015;6:1729-35.
[176] Kutes Y, Ye L, Zhou Y, Pang S, Huey BD, Padture NP. Direct Observation of Ferroelectric Domains in Solution-Processed CH3NH3PbI3 Perovskite Thin Films. The Journal of Physical Chemistry Letters. 2014;5:3335-9.
[177] Xiao Z, Yuan Y, Shao Y, Wang Q, Dong Q, Bi C, et al. Giant switchable photovoltaic effect in organometal trihalide perovskite devices. Nat Mater. 2015;14:193-8.
[178] Beilsten-Edmands J, Eperon GE, Johnson RD, Snaith HJ, Radaelli PG. Non-ferroelectric nature of the conductance hysteresis in CH3NH3PbI3 perovskite-based photovoltaic devices. Applied Physics Letters. 2015;106:173502.
[179] Kwi Young Y, Dan R, Takeshi K, Minoru N, Masanori O. Giant Ferroelectric Polarization Beyond 150 μC/cm 2 in BiFeO 3 Thin Film. Japanese Journal of Applied Physics. 2004;43:L647.
[180] Fan Z, Xiao J, Sun K, Chen L, Hu Y, Ouyang J, et al. Ferroelectricity of CH3NH3PbI3 Perovskite. The Journal of Physical Chemistry Letters. 2015;6:1155-61.
[181] Scott JF. Ferroelectrics go bananas. Journal of Physics: Condensed Matter. 2008;20:021001.
[182] Loidl A, Krohns S, Hemberger J, Lunkenheimer P. Bananas go paraelectric. Journal of Physics: Condensed Matter. 2008;20:191001.

[183] Juarez-Perez EJ, Sanchez RS, Badia L, Garcia-Belmonte G, Kang YS, Mora-Sero I, et al. Photoinduced Giant Dielectric Constant in Lead Halide Perovskite Solar Cells. J Phys Chem Lett. 2014;5:2390-4.
[184] Frost JM, Walsh A. What Is Moving in Hybrid Halide Perovskite Solar Cells? Accounts of Chemical Research. 2016;49:528-35.
[185] Taskin AA, Lavrov AN, Ando Y. Fast oxygen diffusion in A-site ordered perovskites. Progress in Solid State Chemistry. 2007;35:481-90.
[186] Adler S, Russek S, Reimer J, Fendorf M, Stacy A, Huang Q, et al. Local structure and oxide-ion motion in defective perovskites. Solid State Ionics. 1994;68:193-211.
[187] Chadwick AV, Strange JH, Ranieri GA, Terenzi M. Studies of ionic motion in perovskite fluorides. Solid State Ionics. 1983;9–10, Part 1:555-8.
[188] Mizusaki J, Arai K, Fueki K. Ionic conduction of the perovskite-type halides. Solid State Ionics. 1983;11:203-11.
[189] Haruyama J, Sodeyama K, Han L, Tateyama Y. First-Principles Study of Ion Diffusion in Perovskite Solar Cell Sensitizers. Journal of the American Chemical Society. 2015;137:10048-51.
[190] Azpiroz JM, Mosconi E, Bisquert J, De Angelis F. Defect migration in methylammonium lead iodide and its role in perovskite solar cell operation. Energy & Environmental Science. 2015;8:2118-27.
[191] deQuilettes DW, Zhang W, Burlakov VM, Graham DJ, Leijtens T, Osherov A, et al. Photo-induced halide redistribution in organic-inorganic perovskite films. Nat Commun. 2016;7.
[192] Jaffe A, Lin Y, Beavers CM, Voss J, Mao WL, Karunadasa HI. High-Pressure Single-Crystal Structures of 3D Lead-Halide Hybrid Perovskites and Pressure Effects on their Electronic and Optical Properties. ACS Central Science. 2016;2:201-9.
[193] Xiong J, Yang B, Wu R, Cao C, Huang Y, Liu C, et al. Efficient and non-hysteresis CH3NH3PbI3/PCBM planar heterojunction solar cells. Organic Electronics. 2015;24:106-12.
[194] Kim H-S, Jang I-H, Ahn N, Choi M, Guerrero A, Bisquert J, et al. Control of I–V Hysteresis in CH3NH3PbI3 Perovskite Solar Cell. The Journal of Physical Chemistry Letters. 2015:4633-9.
[195] Carrillo J, Guerrero A, Rahimnejad S, Almora O, Zarazua I, Mas-Marza E, et al. Ionic Reactivity at Contacts and Aging of Methylammonium Lead Triiodide Perovskite Solar Cells. Advanced Energy Materials. 2016;6:n/a-n/a.
[196] Snaith HJ, Abate A, Ball JM, Eperon GE, Leijtens T, Noel NK, et al. Anomalous Hysteresis in Perovskite Solar Cells. J Phys Chem Lett. 2014;5:1511-5.
[197] Bi D, Tress W, Dar MI, Gao P, Luo J, Renevier C, et al. Efficient luminescent solar cells based on tailored mixed-cation perovskites. Science Advances. 2016;2.
[198] Niu G, Guo X, Wang L. Review of recent progress in chemical stability of perovskite solar cells. Journal of Materials Chemistry A. 2015;3:8970-80.
[199] Fang H, Jena P. Super-ion inspired colorful hybrid perovskite solar cells. Journal of Materials Chemistry A. 2016;4:4728-37.
[200] Liu Y, Yang Z, Cui D, Ren X, Sun J, Liu X, et al. Two-Inch-Sized Perovskite CH3NH3PbX3 (X = Cl, Br, I) Crystals: Growth and Characterization. Advanced Materials. 2015;27:5176-83.
[201] Stoumpos CC, Malliakas CD, Kanatzidis MG. Semiconducting tin and lead iodide perovskites with organic cations: phase transitions, high mobilities, and near-infrared photoluminescent properties. Inorganic chemistry. 2013;52:9019-38.
[202] Sutton RJ, Eperon GE, Miranda L, Parrott ES, Kamino BA, Patel JB, et al. Bandgap-Tunable Cesium Lead Halide Perovskites with High Thermal Stability for Efficient Solar Cells. Advanced Energy Materials. 2016;6:1502458.

[203] Han Q, Bae S-H, Sun P, Hsieh Y-T, Yang Y, Rim YS, et al. Single Crystal Formamidinium Lead Iodide (FAPbI3): Insight into the Structural, Optical, and Electrical Properties. Advanced Materials. 2016;28:2253-8.
[204] S. Sharma NW, A. Weiss , . Phase Diagrams of Quasibinary Systems of the Type: ABX3 — A′ BX3; ABX3 — AB′ X3, and ABX3 — ABX′ 3; X = Halogen. Z Phys Chem 1992;175.
[205] Lee J-W, Seol D-J, Cho A-N, Park N-G. High-Efficiency Perovskite Solar Cells Based on the Black Polymorph of HC(NH2)2PbI3. Advanced Materials. 2014;26:4991-8.
[206] Stoumpos CC, Malliakas CD, Peters JA, Liu Z, Sebastian M, Im J, et al. Crystal Growth of the Perovskite Semiconductor CsPbBr3: A New Material for High-Energy Radiation Detection. Crystal Growth & Design. 2013;13:2722-7.
[207] Moller CK. Crystal Structure and Photoconductivity of Caesium Plumbohalides. Nature. 1958;182.
[208] Binek A, Hanusch FC, Docampo P, Bein T. Stabilization of the Trigonal High-Temperature Phase of Formamidinium Lead Iodide. The Journal of Physical Chemistry Letters. 2015;6:1249-53.
[209] Jeon NJ, Noh JH, Yang WS, Kim YC, Ryu S, Seo J, et al. Compositional engineering of perovskite materials for high-performance solar cells. Nature. 2015;517:476-80.
[210] Lee J-W, Kim D-H, Kim H-S, Seo S-W, Cho SM, Park N-G. Formamidinium and Cesium Hybridization for Photo- and Moisture-Stable Perovskite Solar Cell. Advanced Energy Materials. 2015:1501310.
[211] McMeekin DP, Sadoughi G, Rehman W, Eperon GE, Saliba M, Hörantner MT, et al. A mixed-cation lead mixed-halide perovskite absorber for tandem solar cells. Science. 2016;351:151-5.
[212] Yue-Yu Zhang SC, Peng Xu, Hongjun Xiang, Xin-Gao Gong, Aron Walsh, Su-Huai Wei. Intrinsic Instability of the Hybrid Halide Perovskite Semiconductor CH3NH3PbI3. cond-matmtrl-sci. 2015:11.
[213] Christians JA, Miranda Herrera PA, Kamat PV. Transformation of the Excited State and Photovoltaic Efficiency of CH3NH3PbI3 Perovskite upon Controlled Exposure to Humidified Air. Journal of the American Chemical Society. 2015;137:1530-8.
[214] Yang J, Siempelkamp BD, Liu D, Kelly TL. Investigation of CH3NH3PbI3 Degradation Rates and Mechanisms in Controlled Humidity Environments Using in Situ Techniques. ACS Nano. 2015;9:1955-63.
[215] Saliba M, Matsui T, Seo J-Y, Domanski K, Correa-Baena J-P, Mohammad K N, et al. Cesium-containing Triple Cation Perovskite Solar Cells: Improved Stability, Reproducibility and High Efficiency. Energy & Environmental Science. 2016;9.
[216] Aldibaja FK, Badia L, Mas-Marza E, Sanchez RS, Barea EM, Mora-Sero I. Effect of different lead precursors on perovskite solar cell performance and stability. Journal of Materials Chemistry A. 2015;3:9194-200.
[217] Li X, Ibrahim Dar M, Yi C, Luo J, Tschumi M, Zakeeruddin SM, et al. Improved performance and stability of perovskite solar cells by crystal crosslinking with alkylphosphonic acid ω-ammonium chlorides. Nature chemistry. 2015;7:703-11.
[218] Bi D, Gao P, Scopelliti R, Oveisi E, Luo J, Grätzel M, et al. High-Performance Perovskite Solar Cells with Enhanced Environmental Stability Based on Amphiphile-Modified CH3NH3PbI3. Advanced Materials. 2016;28:2910-5.
[219] Smith IC, Hoke ET, Solis-Ibarra D, McGehee MD, Karunadasa HI. A Layered Hybrid Perovskite Solar-Cell Absorber with Enhanced Moisture Stability. Angewandte Chemie International Edition. 2014;53:11232-5.
[220] Veldhuis SA, Boix PP, Yantara N, Li M, Sum TC, Mathews N, et al. Perovskite Materials for Light-Emitting Diodes and Lasers. Advanced Materials. 2016:n/a-n/a.

[221] Zhou H, Chen Q, Li G, Luo S, Song T-b, Duan H-S, et al. Interface engineering of highly efficient perovskite solar cells. Science. 2014;345:542-6.
[222] Misra RK, Aharon S, Li B, Mogilyansky D, Visoly-Fisher I, Etgar L, et al. Temperature- and Component-Dependent Degradation of Perovskite Photovoltaic Materials under Concentrated Sunlight. The Journal of Physical Chemistry Letters. 2015;6:326-30.
[223] Ito S, Tanaka S, Manabe K, Nishino H. Effects of Surface Blocking Layer of Sb2S3on Nanocrystalline TiO2for CH3NH3PbI3Perovskite Solar Cells. The Journal of Physical Chemistry C. 2014;118:16995-7000.
[224] Guarnera S, Abate A, Zhang W, Foster JM, Richardson G, Petrozza A, et al. Improving the Long-Term Stability of Perovskite Solar Cells with a Porous Al2O3 Buffer Layer. The Journal of Physical Chemistry Letters. 2015;6:432-7.
[225] Li W, Zhang W, Van Reenen S, Sutton RJ, Fan J, Haghighirad AA, et al. Enhanced UV-light stability of planar heterojunction perovskite solar cells with caesium bromide interface modification. Energy & Environmental Science. 2016;9:490-8.
[226] Leijtens T, Eperon GE, Pathak S, Abate A, Lee MM, Snaith HJ. Overcoming ultraviolet light instability of sensitized TiO(2) with meso-superstructured organometal tri-halide perovskite solar cells. Nat Commun. 2013;4:2885.
[227] Chander N, Khan AF, Chandrasekhar PS, Thouti E, Swami SK, Dutta V, et al. Reduced ultraviolet light induced degradation and enhanced light harvesting using YVO4:Eu3+ down-shifting nano-phosphor layer in organometal halide perovskite solar cells. Applied Physics Letters. 2014;105:033904.
[228] Wang L, Wu M, Gao Y, Ma T. Highly catalytic counter electrodes for organic redox couple of thiolate/disulfide in dye-sensitized solar cells. Applied Physics Letters. 2011;98:221102.
[229] Li W, Dong H, Wang L, Li N, Guo X, Li J, et al. Montmorillonite as bifunctional buffer layer material for hybrid perovskite solar cells with protection from corrosion and retarding recombination. Journal of Materials Chemistry A. 2014;2:13587-92.
[230] Zhang H, Shi Y, Yan F, Wang L, Wang K, Xing Y, et al. A dual functional additive for the HTM layer in perovskite solar cells. Chemical Communications. 2014;50:5020-2.
[231] Liu J, Wu Y, Qin C, Yang X, Yasuda T, Islam A, et al. A dopant-free hole-transporting material for efficient and stable perovskite solar cells. Energy & Environmental Science. 2014;7:2963-7.
[232] Yan W, Li Y, Li Y, Ye S, Liu Z, Wang S, et al. Stable high-performance hybrid perovskite solar cells with ultrathin polythiophene as hole-transporting layer. Nano Research. 2015;8:2474-80.
[233] Abate A, Paek S, Giordano F, Correa-Baena J-P, Saliba M, Gao P, et al. Silolothiophene-linked triphenylamines as stable hole transporting materials for high efficiency perovskite solar cells. Energy Environ Sci. 2015.
[234] Li Z. Stable Perovskite Solar Cells Based on WO₃ Nanocrystals as Hole Transport Layer. Chemistry Letters. 2015;44:1140-1.
[235] Zhang H, Cheng J, Lin F, He H, Mao J, Wong KS, et al. Pinhole-Free and Surface-Nanostructured NiOx Film by Room-Temperature Solution Process for High-Performance Flexible Perovskite Solar Cells with Good Stability and Reproducibility. ACS Nano. 2016;10:1503-11.
[236] Habisreutinger SN, Leijtens T, Eperon GE, Stranks SD, Nicholas RJ, Snaith HJ. Carbon Nanotube/Polymer Composites as a Highly Stable Hole Collection Layer in Perovskite Solar Cells. Nano Letters. 2014;14:5561-8.
[237] Han Y, Meyer S, Dkhissi Y, Weber K, Pringle JM, Bach U, et al. Degradation observations of encapsulated planar CH3NH3PbI3 perovskite solar cells at high temperatures and humidity. Journal of Materials Chemistry A. 2015;3:8139-47.